CALT 68-xxxx
CNS Thesis

Neuromorphic Models of Visual and Motion Processing in the Fly Visual System

Thesis by

Shih-Chii Liu

In Partial Fulfillment of the Requirements
for the Degree of
Doctor of Philosophy

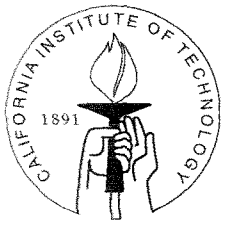

California Institute of Technology
Pasadena, California

1997
(Submitted May 20, 1997)

Acknowledgements

I am indebted to my advisor, Carver Mead, for his inspiration, support, and encouragement during my graduate tenure. I am grateful to my committee members, Christof Koch, Pietro Perona, John Allman, and Rob de Ruyter van Steveninck.

Special thanks to Tobias Delbrück, for his love, support, encouragement, and technical assistance in my research. I am grateful to Kwabena Boahen for his tremendous assistance in my initial years in the lab, and for his inspirational work. I also thank Bradley A. Minch and Rahul Sarpeshkar for their many helpful and interesting discussions. I am also thankful to other members of the lab, Lena Petersen, Chris Diorio, Paul Hasler, Dick Lyon, and Sanjoy Mahajan for their assistance and helpful discussions. I thank Rob de Ruyter van Steveninck and Simon Laughlin for their help in understanding the biological aspects of fly vision. To Misha Mahowald, I thank her for her inspirational ideas in retinal modeling. To John Harris, I thank him for introducing me to research in vision. I also thank many other colleagues; especially Bhusan Gupta, Tim Horiuchi, Jeff Dickson, Andreas Andreou, Rodney Douglas, Jörg Kramer, Giacomo Indiveri, Ron Benson, and Öjvind Bernander for stimulating discussions. I thank Bimal Mathur for his support during my dissertation work.

To Lyn Dupre, I thank you for editing this manuscript; To Candace Schmidt and Donna Fox, I thank you for your help in taking care of the lab.

To my parents, and my sisters, Shih Sing and Shih Ling, I thank you for the constant support and encouragement throughout my life. To Manny Delbrück, I thank you for the wonderful camping trips.

Abstract

Since the first neuromorphic retina was introduced 10 years ago, we have seen neuromorphic modeling extended to motion processing, saccadic systems, and auditory processing, to name a few. This dissertation extends neuromorphic modeling to the fly visual system. The retinotopic and regular arrangement of the layers in this system makes viable the mapping of the structure of the layers to silicon. The ability of the fly to compute motion reliably with only 24,000 receptors, while consuming only microwatts of power, also makes this system attractive for neuromorphic modeling. I start this dissertation by comparing the filter bandwidth properties and offsets of the fly receptors with those of silicon receptors. The filtering properties and the offsets of the receptors are critical because they determine the limits of subsequent processing circuitry. This work is the first characterization of biological and artificial offsets. Next, I describe an analog circuit that captures some of the adaptation and temporal filtering properties of the cells in the initial layers of the visual system. The adaptation time constant of the circuit is controllable via an external bias. The temporal filtering of the circuit changes with the S/N ratio of the signals. This prefiltering preceding the motion areas is important to ensure that the motion computation is robust under different S/N ratios. The filtering should be adaptive to match the S/N ratio so as to maximise the information transfer to subsequent processing. Adaptation is also a big component of the motion computation since the visual system has to extract information from a 2 to 3 decade range of speeds of objects under a six decade range of illumination. In this dissertation, I show the first adaptive motion model that matches its time scale to that of the moving image. The model explains experimental data showing motion adaptation in the direction-selective cells of the fly. Finally, I describe a novel analog silicon implementation of the Reichardt model that is used to describe the responses of the direction-selective cells to motion. This silicon model is critical in showing that local direction selectivity can be computed from the

correlation of continuous-time, graded inputs. The computation integrates the visual information over time in the decision making process and binarized features are not needed for the correlation. This model differs from previous silicon implementations of the Reichardt model that used token-based information for correlation. This model is a closer analogue of the motion computation in flies than previous silicon models.

Contents

List of Figures

List of Tables

Chapter 1 Introduction

This dissertation describes the neuromorphic modeling of the initial layers of the fly's visual system and the motion-adaptation process in the direction-selective cells. It also describes a silicon model of the direction-selective computation in the fly. The retinotopically ordered subunits of the fly's visual system makes the latter a good candidate for neuromorphic modeling. Extensive studies of insects's optics [1], visual behavior [2][3][4], physiology [5], neuroanatomy [6], and oculomotor control [7] have been undertaken over the past 40 years. A review of the work in insects can be found in different sources [8][9][6][10][11].

The ability of the fly to navigate with 24,000 receptors (in the *Musca*) using only milliwatts of powers is amazing. The small number of receptors (as compared to 10^6 cones and about 100×10^6 rods in our retina), the low power consumption, and the retinotopic arrangement of the subunits of the visual layers, make it feasible to model the visual system on silicon. The number of receptors is at least eight times smaller than the number of pixels (300,000) on a standard VGA imager. The pixel size of both CCD imagers (20 to 30μm) and CMOS imagers (10 to 50μm) is comparable to the facet size of the subunits of the fly's eye (20 to 50μm). The optics for silicon imagers is not diffraction limited, since most imagers use single lenses. However, with the decreasing pixel size of silicon imagers, individual lenses on each pixel are needed, as in the fly's eye, to increase the collecting power of light. Sharp, for example, has a microlens over each photosensitive element in their high density imagers. Sony has a similar implemention with its Hyper HAD technology. There is a growing interest in low-power systems in the silicon industry as the density of transistors grows with the decreasing line widths. The decreased power consumption is accomplished partially by a reduced power supply and partially through processing techniques. This trend leads to complex chips that consume microwatts of power, and thus fits in with the low power consumption observed in flies.

The physics of the phototransduction process is similar in biological receptors and silicon receptors, because this process involves the conversion of photons to the flow of charged particles. This similarity means that the noise sources in both kinds of receptors are the same, and the signal is subjected to both photon noise and transducer noise. Both biological and silicon systems are similar in the sense that they have to deal with mismatches. By modeling in silicon, we can understand how neural computation deals with the system offsets. The similarities in the physics of computation in both systems make neuromorphic modeling helpful in our quest to understand the neural computation in the visual system.

An important benefit from neuromorphic modeling is the bidirectional flow of biological-based algorithms to more efficient artificial systems. This need is dire in artificial motion systems, which are cumbersome and power hungry. Motion algorithms that run on digital systems are also constrained by the serial-processing nature of these systems. Artificial motion systems that use front-end CCD sensors with 640×480 pixels are found wanting; partially because the information flow is limited by the frame rate of the sensors; and partially because the data are computed serially on the digital system. Some motion algorithms cannot deal with the frame rate of CCD sensors, so motion is computed on fewer than 60 frames/second. It is true that the advent of faster processors can solve part of this problem, but faster processors also mean higher power consumption. If flies can extract motion with 24,000 receptors using milliwatts of power, it is obvious that there are lessons that we can learn from the underlying motion computation in the biological system. There are already two ways that researchers have tried to improve motion systems: by using continuous-time sensors, and by processing the information in parallel in real time.

With silicon microchips, we can use small robot systems with specialized vision chips to understand autonomous navigation. A robotic platform with a front-end sensor, an analogue of the fly's eye that was built by Franceschini and colleagues [12], weighs about 10kg. Its compound eye consists of 100 electro-optical sensors arranged in a circle; it weighs 1kg. We can scale the weight and size of the robot platform by 2 or 3 orders of magnitude by using silicon microchips.

1.1 Background of Silicon Retinae

Neuromorphic modeling of retinal processing has evolved in the past 10 years, since the first silicon retina by Mahowald and Mead in 1988 [13][14][15][16]. That silicon retina is a model of the cones, horizontal cells, and bipolar cells of the outer plexiform layer (OPL) of the vertebrate retina. It performs automatic local gain control through network adaptation, and models the spatiotemporal responses of the cones and the horizontal cells. A later receptor design by Delbrück [17] implements automatic gain control through local adaptation in the pixel. The silicon retina by Boahen and Andreou [18] is a close correlate to the neurocircuitry of the OPL. By using current-mode CMOS transistors, the researchers were able to model the shunting inhibition of the horizontal cells onto the cones, and to model the gap junctions in the cones and horizontal cells with a single transistor. The shunting inhibition was not implemented in the previous retinae. Boahen and Andreou's retina also includes inter-receptor coupling that changes with the signal-to-noise (S/N) ratio of the input. The adaptive spatiotemporal filtering of this retina corresponds to the physiology of the cells in the OPL [19][20]. The advantages of using a biologically inspired, continuous-time sensor over a CCD sensor have been explicated by Delbrück [17] and by Boahen [21]. The noise properties of the silicon sensor have also been measured in detail by Delbrück [17].

1.2 Overview

This dissertation extends neuromorphic modeling to the domain of the invertebrate eye. The fly's eye is a compound eye, which consists of thousands of little eyes, or ommatidia. Each ommatidium has its own lens, whereas the simple eye of vertebrates has only a single lens. The same photopigment, rhodopsin, is present on the micro-tubular membranes of the receptors in the ommatidia, and on the disc-membrane system of rods and cones in vertebrates. The compound eye of the *Musca* has a total of about 24,000 receptors; the human eye has over 1 million cones and 100×10^6 rods.

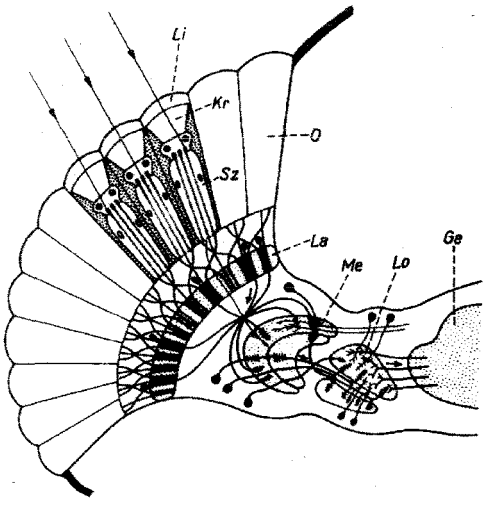

Figure 1.1: Cross-section of compound eye showing the four distinct layers in the visual system. The layers consist of the photoreceptors, the lamina, the medulla, and the lobula complex. The lobula complex is made up of the lobula and the lobula plate. The wide-field direction-selective cells are found in the lobula plate. Source: Adapted from Kirschfeld [17], Figure 1, pg. 63.

Even the total number of 0.5 million neurons in the visual system of the fly is only one-half of the number of cones. Despite these differences between invertebrates and vertebrates, the optical processing and the projection of the image onto the retina of invertebrates is no different from that of vertebrates. The physiology of the cells in the initial visual layers is similar in invertebrate and vertebrate eyes. One difference between both visual systems is that the fly responds faster than most vertebrates.

1.2.1 Speed Issues and Offsets in Silicon

The fly visual system is divided into four distinct layers: the retina, the lamina, the medulla, and the lobula complex as shown in Figure 1.1. The subunits of the retina, lamina, and medulla are retinotopically arranged. The lobula complex is divided into two sections; the lobula and the lobula plate. The lobula plate contains wide-field, direction-selective cells. Most of the cells in these layers respond with

graded potentials, rather than with spikes. The output cells in the lobula plate provide input to the optomotor control system. The range of speeds to which the direction-selective cells respond is determined by the **speed sensitivity** limits of the photoreceptor. In this chapter, I compare the speed limits of biological and silicon receptors under different lighting conditions. The speed sensitivity is determined by the spatial and temporal bandwidths of the receptors. The **spatial bandwidth** in the fly is determined by the acceptance angle of the receptors and the optics. The spatial bandwidth of the silicon receptors is set by the optics, the sensor width, and the spatial period between the receptors. The **temporal bandwidth** in both receptors is determined by the time constant of the receptors.

The neural system and the silicon system have to deal with **offsets** or **mismatches** between the neurons or transistors, respectively. In Chapter 2, I describe how the DC offsets and AC gain mismatches measured in two silicon retinae compare with that of the photoreceptors in the fly retina. The offsets in silicon can be reduced through well-controlled processing, careful design and layout of the circuits, and adaptation mechanisms. The offsets in the neural system can be reduced through adaptation and self-calibration.

1.2.2 Circuit Model of Retina and Lamina

The photoreceptor cells from the retina are presynaptic (with sign-inverting synapses) to the laminar monopolar cells (LMCs) in the lamina. The LMCs play a role similar to that of the bipolar cells in the OPL of the vertebrate retina. The LMCs code only the signal contrast and adapt their spatiotemporal filtering to the S/N ratio. These cells also exhibit a center-surround organization, but the spatial center-surround property is weak compared to that of the bipolar cells in the OPL. The temporal analogue of the spatial center-surround property is expressed strongly in these cells. This response corresponds to self-inhibition in the cells. In Chapter 3, I describe a small, compact **retino-laminar** circuit that captures the automatic local-gain-control behavior of the receptors, and the adaptive temporal filtering of the LMCs. This circuit is used

as a front end to a direction-selective circuit described in Chapter 5.

1.2.3 Motion Adaptation

The adaptive properties in the photoreceptor cells are also present in the direction-selective cells in the lobula plate. Recordings show that these cells adapt to motion stimuli. The dynamic range of input frequencies to which the cell responds is increased through adaptation. The Hassenstein–Reichardt detector, which models the responses of these direction-selective cells, can be modified to account for this adaptation behavior. The time constants of the filters in this model are assumed to be fixed. In Chapter 4, I present an **adaptive correlation model**, where the time constants of the filters adapt to the stimuli motion. We obtain the stimulus's frequency by comparing the outputs of a lowpass and highpass filter. We then use the difference in the outputs of the filters to adapt the time constant. The results from this model explain the physiological results from the direction-selective cells. The correlates of the subunits of this model cannot be attributed to the neuroanatomical units in the visual layer, because of incomplete physiological information from the cells in the medulla and lobula areas.

1.2.4 Direction Selective Circuit

Different motion algorithms and circuits have been developed in the past 20 years. The initial implementations came from the computer-vision community, where motion algorithms that used CCD sensors as a front end, were implemented on a sequential machine. More recent implementations use continuous-time sensors as a front end, and are based on models that describe direction selectivity in biological systems (except for the gradient model). The most common model used in the neuromorphic community is the correlation model. The models usually follow token-based schemes, in which robust features, such as spatial edges, pulses, or discretized temporal edges, are used for correlation. In Chapter 5, I describe a novel implementation of the correlation model, where **temporal averaging** and **mutual inhibition** are part of the

direction selectivity process. The circuit uses the graded output signals of the retino-laminar circuit described in Chapter 3, and does not use any pulses or edges in the direction selective computation. Previous implementations have ignored the temporal averaging computation in the correlation model, and only one other implementation incorporated mutual inhibition [22].

Bibliography

[1] K. Kirschfeld, "The visual system of Musca: Studies on optics, structure and function," *Information Processing in the Visual Systems of Arthropods*, R. Wehner, Editor, pp. 61–74, Springer–Verlag, Berlin, Heidelberg, New York, 1972.

[2] B. Pick, "Visual pattern discrimination as an element of the fly's orientation behavior," *Biol. Cybernetics*, **23**, pp. 171–180, 1976.

[3] T. Poggio and W. Reichardt, "Visual control of orientation behaviour in the fly: Part II: Towards the underlying neural interactions," *Q. Rev. Biophys.*, **9**, pp. 377–438, 1976.

[4] W. Reichardt and T. Poggio, "A theory of the pattern induced flight orientation of the fly *Musca domestica* II," *Biol. Cybernetics*, **18**, pp. 69–80, 1975.

[5] S. B. Laughlin, "Matching coding, circuits, cells, and molecules to signals - General principles of retinal design in the fly's eye," *Progress in Retinal and Eye Research*, **13:1**, pp. 165–196, 1994.

[6] I. A. Meinertzhagen and A. Frölich, "The regulation of synapse formation in the fly's visual system," *Trends in Neuroscience*, **6**, pp. 223–228, 1983.

[7] N. J. Strausfeld and C. Gilbert, "Small-field neurons associated with oculomotor control in muscoid flies: cellular organization in the lobula plate," *Journal of Comparative Neurology*, **316**, pp. 56–71, 1992.

[8] M. Land, "Optics and vision in invertebrates," in *Handbook of Sensory Physiology, Vol VII/6B*, H. Autrum, ed. Springer-Verlag, Berlin, Heidelberg, New York, pp. 472–592, 1981.

[9] S. Shaw, "Anatomy and physiology of identified non-spiking cells in the photoreceptor-lamina complex of the compound eye of insects, especially *Diptera*," in *Neurones without Impulses*, A. Roberts and B. Bush, Editors, pp. 61–116, Cambridge Univ. Press, Cambridge, 1981.

[10] S. Laughlin, "Neural principles in the visual system," in *Handbook of Sensory Physiology, Vol VII/6B*, H. Autrum, ed. Springer-Verlag, Berlin, Heidelberg, New York, pp. 133–280, 1981.

[11] N. Franceschini, "Early processing of colour and motion in a mosaic visual system," *Neuroscience Research, Suppl. 2*, pp. S17-S49, 1985.

[12] N. Franceschini, J. M. Pichon, and C. Blanes, "From insect vision to robot vision," *Phil. Trans. Roy. Soc. London B*, **337:1281**, pp. 283–294, 1992.

[13] C. A. Mead and M. A. Mahowald, "A silicon model of early visual processing," *Neural Networks*, **1**, pp. 91–97, 1988.

[14] M. A. Mahowald and C. A. Mead, "Silicon retina," in *Analog VLSI and Neural Systems*, C. A. Mead, ed. Addison Wesley, Reading, MA, pp. 257–278, 1989.

[15] M. A. Mahowald, " A silicon retina with adaptive photoreceptors," in *SPIE/SPSE Symposium on Electronic Science and Technology: From Neurons to Chips.* Orlando, FL, April 1991.

[16] M. Mahowald, "VLSI analogs of neuronal visual processing: a synthesis of form and function," *Ph.D. Thesis*, California Institute of Technology, Pasadena, CA, 1994.

[17] T. Delbrück, "Analog VLSI phototransduction by continous-time, adaptive, logarithmic photoreceptor circuits," CNS Memo No.30, California Institute of Technology, Pasadena, CA, 1994.

[18] K. A. Boahen, and A. G. Andreou, "A contrast sensitive silicon retina with reciprocal synapses," in *Advances in Neural Information Processing Systems 4*, D. S. Touretzky, ed. Morgan Kaufmann, San Mateo, CA, pp. 764–772, 1992.

[19] K. A. Boahen, "Spatiotemporal sensitivity of the retina: A physical model," *CNS Memo CNS-TR-91-06*, California Institute of Technology, Pasadena, CA 91125, June 1991.

[20] K. Boahen, "Retinomorphic vision systems: reverse engineering the vertebrate retina," *Ph.D. Thesis*, California Institute of Technology, Pasadena, CA, 1997.

[21] K. A. Boahen, "A retinomorphic vision system," *IEEE Micro*, **16:5**, pp. 30–39, 1996.

[22] R. Benson and T. Delbrück, "Direction selective silicon retina that uses null inhibition," in *Advances in Neural Information Processing Systems 4*, J. Moody, S. Hanson, and R. Lippmann, eds, Morgan Kaufmann, San Mateo, CA, pp. 756–763, 1992.

Chapter 2 Photoreceptor Modeling

The receptors in the invertebrate retina and the rods and cones in the vertebrate retina have the same task of transducing light into an electrical signal. Both types of retinae have to contend with coding the information over a large range of intensities. The dynamic range of the fly's receptors is about 7 decades, whereas that of the vertebrate retina is about 10 decades. The wider dynamic range of the vertebrate retina is made possible through two groups of receptors: the rods and the cones. The cones code the higher range of intensities, and the rods take over when the background drops to the level of moonlight.

The sampling arrangement of fly receptors is regular. Thus, we can make comparisons between the fly receptors and a sampling grid of silicon receptors. Since the receptors are the front end to any subsequent visual processing, they constrain the information flow to later layers. In insects, one important piece of the visual information extracted is motion so the limit of speed sensitivities in the receptors is critical. The **speed sensitivity** is determined by the spatial and temporal bandwidths of the receptors. These bandwidths vary with background intensities. A similar argument can be proposed for analog silicon systems. In this chapter, I compute the speed sensitivities of silicon receptors, and compare them with that of the fly receptors. I also review the geometrical optics of insect eyes and lenses, since the optical cutoff frequency determines the spatial bandwidths of the receptors.

Both neural and silicon systems have mismatches among their neurons or transistors, respectively. Here, measurements of the **DC offsets** and **AC gain mismatches** are characterized on two silicon retinae; one with 59×66 pixels, and the other with 32×32 pixels. The pixels consist of the photoreceptor circuit model by Delbrück [20]. I compare these offsets with the offsets measured from fly receptors. Silicon offsets can be reduced through a well-controlled process, and through careful design and layout. We can also use long-term adaptation to remove offsets.

2.1 Fly Photoreceptors

The anatomy and optics of insect receptors have been extensively studied by many researchers [1][2][3]. A short description of the optics and the anatomy of the receptors is given here.

2.1.1 Ommatidium

The compound eye in the *Musca* consists of about 3000 ommatidia, or "little eyes." The corneal lens and the crystalline cone make up the dioptric apparatus of each ommatidium. The ommatidia are arranged hexagonally over the whole eye, but the interommatidial angle increases away from the equatorial region of the eye. The dioptric apparatus and the cells constituting each ommatidium are shown in Figure 2.1. An ommatidium consists of the lens, a crystalline cone, a cluster of retinula cells, glial cells, pigment cells, and optical support cells. Each retinula cell has a rhabdomere, which in *Calliphora*, consists of about 60,000 aligned tubular microvilli, each about 70nm across and about 300μm long [4][5]. The microvilli are equivalent to the disks in the rod outer segments in the vertebrate retina. They increase the surface area of the cell on which a high concentration of the photosensitive pigment, rhodopsin, ($\geq$ 100 million molecules of rhodopsin per cell), is situated. Light is absorbed by the rhodopsin on the microvilli. The rhabdomere has a diameter of about 1μm and a high refractive index, so it behaves like a wave guide from the focal plane of the lens. In most insects, the rhabdomeres are fused to form a rhabdom. In the higher *Diptera*, the rhabdomeres are separate and they point in a different visual axis. In the *Drosophila*, there are eight rhabdomeres (R1 to R8) in each ommatidium as shown in Figure 2.2a. R1 to R6 have a rhodopsin peak in the blue part of the spectrum at 490nm, and another peak in the ultraviolet range. R7 is predominantly an ultraviolet receptor, with enhanced blue sensitivity in a subpopulations of cells. R8 is predominantly a blue–green receptor. R1 to R6 synapse onto cells in the lamina; R7 and R8 synapse onto cells in the medulla. Each receptor has its own visual axis, as shown in Figure 2.2b. Each cartridge in the lamina collects visual signals from

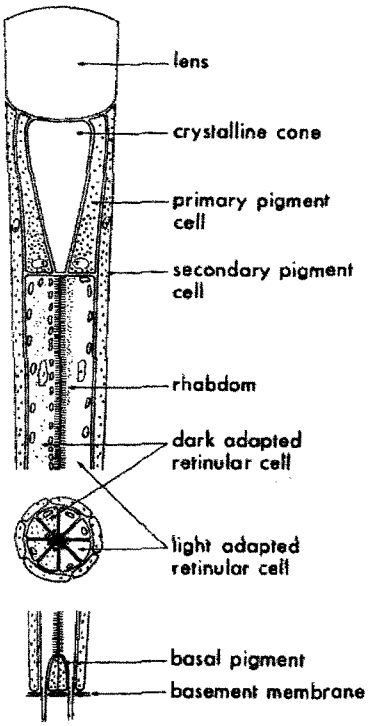

Figure 2.1: Dioptric apparatus and cells comprising an ommatidium of an apposition eye. The figure shows the detailed anatomy of the ommatidium. Source: Adapted from Stavenga [3], Figure 2, pg 360.

six rhabdomeres that point in the same visual axis. This wiring between the retina and the lamina is called **neural superposition**. Kirschfeld [1] pointed out that this wiring is a means of increasing the optical aperture of the collector and the gathering power of the eye, while retaining high visual acuity. The ommatidia are somewhat optically insulated from one another by the pigment cells. The arrangement of the eight receptors in the ommatidium is shown in Figure 2.2b. The lens in each facet inverts the image, so the axon bundles from the retina makes a 180° twist before synapsing onto the cartridges as shown in Figure 2.2c.

2.1.2 Dioptric Arrangement

Both the single lens of the vertebrate camera eye and the multi-facet optics of the compound eye perform the same kind of optical processing. The optical image is

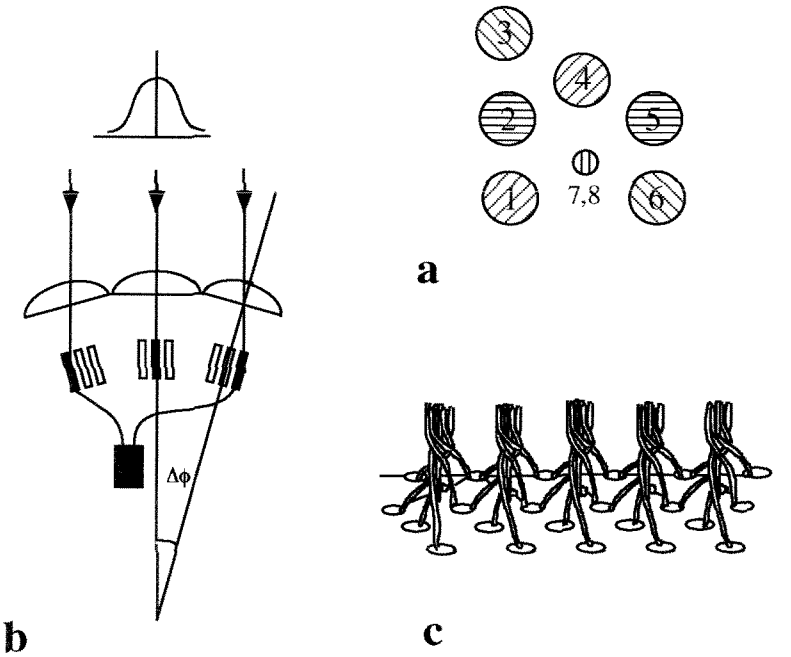

Figure 2.2: Neural superposition of receptors onto the laminar cells. (a) The figure shows the arrangement of the receptor cells, R1 to R8, in the ommatidium. (b) The figure shows the neural superposition of receptors with the same visual axes from neighboring ommatidia onto a cartridge in the lamina. The visual angle, $\Delta\phi$, is the interommatidial angle. (c) The figure shows the twist in the axons of the receptors before synapsing onto the cells in the different cartridges. Source: Figure 2.2a adapted from Kirschfeld [2], Figure 5a, pg. 68; Figure 2.2c adapted from Franceschini [33], Figure 12b, pg. S33.

projected onto the ommatidia in the compound eye, and onto the rods and cones in the vertebrate eye. However, the compound eye has lower resolution due to diffraction limits. The visual resolution is about 1° to 2° in the *Musca*, whereas the resolution is about 0.5 min in the fovea of the human eye. To obtain the high resolution of the fovea, the compound eye on a human would have a diameter of 1m, as shown by Kirschfeld [6]. The decreased resolution of compound eyes does not affect detectability of an image that covers a visual field of several ommatidia. It means that the insect has to be closer to a scene, than a human. The high refractive index of the lens creates a magnifying lens with a focal length of 50μm to 78μm. The diameter of each facet is about 25μm to 35μm, so the f-number of each eye is about 1 to 2. The optics

of insects have been studied by many researchers since Exner in 1851 [6].

2.2 Fundamental Limits in Biological and Silicon Receptors

In this section, I look at the constraints that the receptors place on the later processing layers in both neural and silicon systems. Since the visual input of interest is motion, the speed responses of the direction-selective circuitry in both systems are limited by the speed responses at the receptors. Luckily, the regular arrangement of the facets is similar to that of a regular grid of silicon receptors. Hence, we can use similar techniques to compute the speed sensitivities of both types of receptors. Much research has been carried out to determine the tradeoffs among the optics, the sampling density of the ommatidia, the visual resolution, and the eye size in insects. A review of this work can be found in [7][8]. Both Laughlin [9] and Glantz [10] have analyzed the speed sensitivities of various insect receptors. Similar analytical methods can also be applied to silicon receptors.

2.2.1 Optics

The optics of the animal or the silicon imager determines the optical cutoff frequency, ν_{co}, of the visual input to the receptors. Since the lens pupil in the insect eye is diffraction limited, we can determine ν_{co} from the Airy's disc. The diameter of the Airy's disc is $2.44\lambda/D$, where D is the diameter of the facet and λ is the wavelength of the light. We approximate the Airy's disc by a Gaussian, and the half-width of the Gaussian is λ/D. Hence, the optical cutoff frequency is given by $\nu_{co} = D/\lambda$. The facet size of the different fly species varies between 25 to 50μm. Assuming λ be 0.5μm and D be 25μm, then $\nu_{co} = 25/0.5(\text{cyc/rad}) = 0.9\text{cyc/deg}$.

In the case of the human or silicon imagers, ν_{co} is determined by the aperture of the eye or the lens. The aperture of the human eye varies between 2.4mm and 6.0mm, depending on the background intensity. Assuming that the aperture is 2mm,

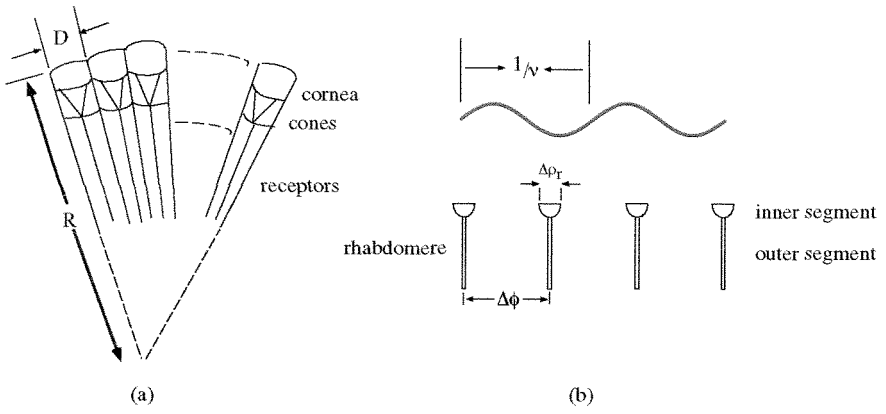

Figure 2.3: Schematic of a compound eye and a sampling array of fly receptors. (a) Figure shows the arrangement of the ommatidia in the compound eye. The diameter of the facet is D and the radius of the eye is R. (b) Figure shows an array of receptors. The interommatidial angle is $\Delta\phi$ and the angular diameter of the rhabdomere is $\Delta\rho_r$. The spatial frequency of the stimulus is ν. Source: Adapted from Snyder [7], Figure 1, pp. 696.

the optical cutoff frequency of humans is given by $\nu_{co} = 2\text{mm}/0.5\mu\text{m} \approx 60\text{cyc/deg}$. The aperture of the lens used on silicon imagers can be computed from the focal length of the lens and the f-number. Some lenses have a fixed f-number: others have f-numbers that vary from 1 to 22. Let us pick an f-number of 2, and focal length of 4mm. The aperture size is then 2mm and $\nu_{co} = 60\text{cyc/deg}$.

The sampling bandwidth of the receptors theoretically should be at least twice the optical cutoff frequency of the lens, by Nyquist's criterion. If it is not so, aliasing will occur. In fact, aliasing is seen in the responses of flies to motion.

2.2.2 Spatiotemporal Bandwidths of Fly Receptors and Silicon Receptors

The dependence of the spatial and temporal bandwidths of the fly receptors and silicon receptors over different background intensities are elucidated in this section. The speed sensitivities of the receptors are then computed from these bandwidths. The output of the receptors depends on the convolution of the visual input with the

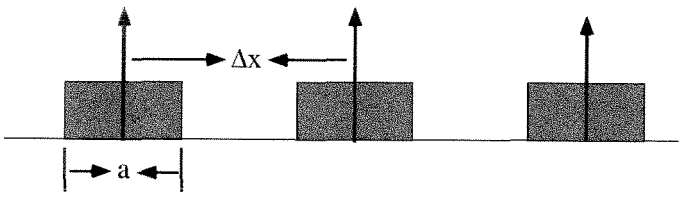

Figure 2.4: Sampling array of silicon receptors. The grid spacing is Δx and the sensor width is a.

optical modulation transfer function (MTF) and the spatial MTF of the receptors. The MTF of the receptors is determined by the width of the sensor area. The highest spatial frequency that can be reconstructed by the array of receptors depends on the sampling period of the array. Analyses of the spatial and temporal bandwidths of the silicon receptor have also been done by Sarpeshkar and colleagues [16].

The relationship between the sensor width and the sampling period determines whether aliasing occurs in the receptor output. This analysis is described in Section 2.2.3. Each pixel normally contains transistors besides the sensor region. The area occupied by the transistors is called the **dead area**. The impact of the dead area between pixels on the motion computation is described in Section 2.2.4 and a description of the visual resolution of silicon and fly receptors is described in Section 2.2.5.

Spatial Bandwidths

The sampling grid of the fly retina is shown in Figure 2.3. The angular diameter of the rhabdomere is $\Delta\rho_r$; the sampling period is defined by the interommatidial angle, $\Delta\phi = D/R$, where D is the diameter of the facet and R is the radius of the eye. For a square array of receptors, the highest resolvable spatial frequency is $\nu_s = 1/2\Delta\phi$; for a hexagonal array, ν_s is given by $\nu_s = 1/\sqrt{3}\Delta\phi$ [7].

The sampling grid of the silicon retina is shown in Figure 2.4. The sensor width, a, corresponds to the angular diameter of the rhabdomere, $\Delta\rho_r$; the grid period, Δx, corresponds to the interommatidial angle, $\Delta\phi$. The conversion of a and Δx to angular

terms depends on the lens in front of the imager. If we use a wide-angle lens with a field of view of 90° and a retina with 60 × 60 pixels, then each pixel subtends an spacing angle of 1.5°. If the lens has a 30° field of view, then the spacing angle will be 0.5°. In the case of the wide-field lens, if we assume $\Delta x = 150\mu$m, then 100μm corresponds to 1°. Assuming a sensor width of 30μm, this width corresponds to an angle of 0.3°. We need to identify a criterion to avoid aliasing in the retina. Again, assuming that $\Delta x = 150\mu$m, the sampling frequency of the retina is $f_s = \frac{1}{2\Delta x} = \frac{1}{300}(\text{cyc}/\mu\text{m}) = \frac{1}{3}\text{cyc/deg}$. The sensor at each pixel acts as a spatial lowpass filter. The filtering by the receptor helps to limit input frequencies that cause aliasing. The spatial MTF of the sensor in the frequency domain is a sinc function of form $\frac{\sin \pi f a}{\pi f}$. We can view the sinc function as a lowpass filter with a cutoff frequency at the first zero, which is $\frac{1}{a}$.

The acceptance angle, $\Delta\rho$, is given by the convolution of the optical MTF of the lens with the spatial MTF of the rhabdomere. This convolution is only an approximation because the acceptance angle varies over different intensities partially through the migration of pigment cells to the rhabdomere. Under high intensities in the locust, the acceptance angle is as low as 1.7°, under low intensities it is as high as 4°. The acceptance angle of silicon receptors is invariant with the background intensity.

Temporal Bandwidth

The temporal bandwidth of fly receptors varies only by a factor of 2 or 3 over several decades of intensity. The temporal resolution is usually defined as the half-width, Δt, of the receptor's temporal impulse response. The temporal bandwidth of our present silicon receptors, on the other hand, is linearly dependent on the background intensity. The temporal bandwidth is defined by $\frac{C}{g_m}$, where C is the capacitance at the sensor node and g_m is the transconductance of the transistor supplying the photocurrent.

Speed Sensitivity

The **speed sensitivity**, v, of the receptor can be defined as the acceptance angle over the half-width of the temporal impulse of the receptor. The speed sensitivity is

Table 2.1: Comparison of Speed Sensitivities in Silicon and Insect Receptors

	$\Delta\rho(deg)$	Δt(ms)	v(°/s)	Intensity
Calliphora	1.2	50	24	160ph/s
Calliphora	1.0	16	60	5×10^5ph/s
Lucilia	1.5	25	60	10eff ph/s
Lucilia	1.2	8.3	145	1×10^{10}eff ph/s
Locust	1.5	20	75	14ph/facet/s
Locust	2.4	48	75	3×10^5ph/facet/s
Silicon	1.5	6	25	3×10^6ph/s
Silicon	1.5	0.004	37500	3×10^{10}ph/s

+Locust results from Howard and Payne [12] and from Glantz [10]
+Lucilia results from Howard and colleagues [13] and from Glantz [10]
+Silicon results from Delbrück [20], $\Delta\rho$ computed using a 90° field of view lens and an array of 60×60 pixels
+Calliphora results from Juusola and colleagues [14] and from Smakman and colleagues [15]

a measure of the upper limit of speeds that can be detected by the receptor. Snyder [11] pointed out that the speed sensitivities of the receptors are almost invariant with intensity, because both the acceptance angle and the integration time decrease by approximately the same factor with increasing intensity. The data for $\Delta\rho$, Δt, and v of different insect receptors and silicon receptors at low and high background intensities are shown in Table 2.1.

As we can see, the speed sensitivities of the fly receptors do not vary much over intensity. In the case of silicon receptors, since the spatial bandwidth is fixed and the temporal bandwidth varies linearly with the intensity, the speed sensitivities of the silicon receptor increases linearly with the background intensity, as shown in Table 2.1. Hence, the speed sensitivity in our silicon receptors decreases too much at low background intensities. Part of this problem can be alleviated by having spatially-coupled receptors where the coupling increases at low background intensities. The spatially-coupled receptor can then be influenced by intensity over a wider region than the sensor area itself. This property is already implemented in some silicon retinae [30]. The other solution is to have an electronic shutter in front of the lens that

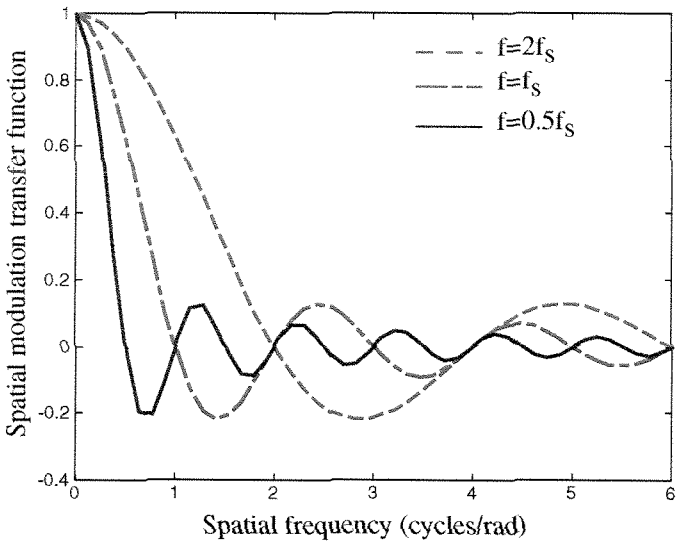

Figure 2.5: Modulation transfer function of a sampling grid of receptors. The diagram shows the MTF for three different cases, $f = f_s$, $f = 0.5f_s$, and $f = 2f_s$. The sampling frequency of the silicon grid is defined as f_s. The curves illustrate how the modulation transfer function depends on the spacing, Δx, and the sensor width, a.

changes the lens aperture at different background intensities. Yet, another solution is to decrease the rate at which the time constant changes over background intensity. The comparison of both types of receptors show that biological receptors do a better job in sensing speed at low background intensities.

2.2.3 Relationship Between the Spatial Bandwidth and Sampling Frequency

The impact of the relationship between the sensor width and the sampling period can be broken up into the three cases, $a \leq \Delta x$, $a = \Delta x$, and $a \geq \Delta x$. This analysis has been demonstrated by Theuwissen [17]. The MTF of the sensor in the frequency domain is given by

$$\text{MTF} = \frac{\sin(\pi f a)/(f_s \Delta x)}{(\pi f a)/(f_s \Delta x)}.$$

The term fa in the MTF function has been normalized by $f_s \Delta x$.

For the first case, where $a \leq \Delta x$, we assume that $a = \Delta x/2$. The MTF is given by

$$MTF = \frac{\sin \pi f/2f_s}{\pi f/2f_s}.$$

The spatial cutoff frequency of the sensor, f, is at $f = 2f_s$. The MTFs for all three cases are shown in Figure 2.5. The Nyquist criterion is not satisfied in this case. For the second case, where $a = \Delta x$, the MTF is given by

$$MTF = \frac{\sin \pi f/f_s}{\pi f/f_s}.$$

The cutoff frequency is now at $f = f_s$. Aliasing is more limited in this case. For the final case, where $a \geq \Delta x$, we assume that $a = 2\Delta x$. Hence,

$$\text{MTF} = \frac{\sin \frac{2\pi f}{f_s}}{\frac{2\pi f}{f_s}}.$$

The cutoff frequency is now at $f = 0.5f_s$. This case satisfies the Nyquist criterion. This analysis is also applicable to the acceptance angle and the interommatidial angle of the fly receptors.

There are two ways to prevent aliasing in the retina: by extending the sensor of one pixel halfway into the neighboring pixels, or by manipulating the silicon process such that electrons generated by the photons colliding with the silicon substrate can be collected by neighboring pixels. The former method is possible in only the 1D case; the latter case is possible for a 2D scenario.

2.2.4 Dead Area

What is the effect of the dead area (i.e., not photosensor area) on the motion computation? In detecting actual motion, the stimulus has to travel between at least two receptors. The time taken by the stimulus to travel between the receptors, δt,

affects the motion processing performed in subsequent layers. For example, if the signals from both receptors are directly correlated together, then δt should be less than the temporal response of the receptor, Δt. We define the dead area by ∂x and the maximum speed detected by the receptor by v_o, where $v_o = a/\Delta t$. Assuming that the speed of the stimulus is v_1, we get $\partial x/v_1 \leq \Delta t = a/v_o$. Hence, we need $v_1 \geq \frac{\partial x v_o}{a}$. If the dead area is large, then the stimulus should be fast, for the receptor outputs to correlate in time. Notice that, if $\partial x \geq a$, then the stimulus speed has to be faster than the maximum speed detected by the receptor. To solve this problem, we have to delay the output of the receptor by a sufficient amount of time, T_{lp}, so that correlation between the pixels can occur. So $\Delta t + T_{lp} \geq \delta t$. Of course, if $\partial x \leq a$, direct correlation between the receptor outputs is possible. In biological receptors, as in silicon receptors, the sensor width is smaller than the pixel spacing, so some delay is introduced in the pathway before correlation is performed on the signals. The other problem with dead area in a pixel is shown in the analysis in Section 2.2.3. If the sensor width is less than the pixel spacing, aliasing occurs.

2.2.5 Visual Resolution of Receptors

The diameter of the facet or the pixel size in silicon affects the visual resolution of the eye or the imager. The spatial resolution is determined by the number of receptors per visual angle. In the fly, eyes with large facets have a lower sampling frequency and a smaller diffraction limit. The visual acuity, however, depends on both the diameter of the facet and the local radius of curvature. If the radius is large, then the visual acuity is higher. The advantage of large facets is that the eyes have more photon collecting power, hence, a higher S/N ratio (valid for the case of a point source). The same results can be extended to the pixels in a silicon imager. The tradeoff between resolution and S/N ratio has been documented by Snyder and colleagues [18], through the use of information theory.

As the pixel size of silicon imagers shrinks and the number of pixels grows, the visual resolution of the silicon receptor starts to approach the visual acuity of the

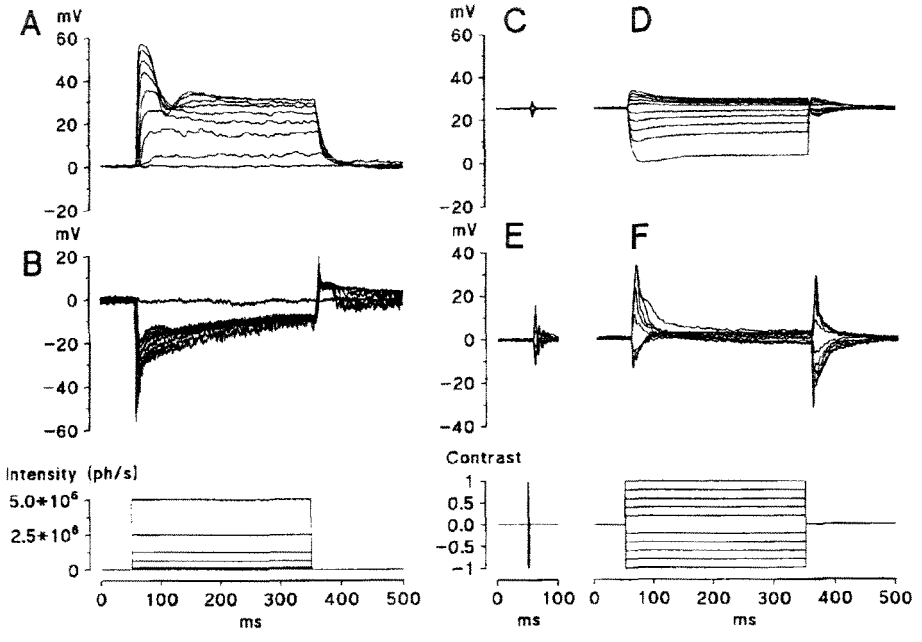

Figure 2.6: Recordings from a photoreceptor and a LMC in *Calliphora*. Step response of a dark-adapted photoreceptor (A) and a LMC to a 300ms light step. On the right are responses of a light-adapted photoreceptor (C) and a LMC (E) to a 20ms contrast step and to a 300ms contrast step (D and F respectively). Source: From Juusola and colleagues [14], Figure 2, pg. 122.

cones in the human fovea. For comparison, the cones in the fovea are 2.5μm apart and the inner segment is 2.3μm wide. The distance of the lens to the retina is 17mm. Hence, the visual acuity is 2.5/17 mrad or 0.5 min of arc. However, the S/N ratio of the pixel in the silicon imager also decreases with the decreasing pixel size so some companies have resorted to putting microlenses on each pixel to increase the collecting power of the pixel.

2.3 Noise Sources

The noise in biological photoreceptors is photon noise and transducer noise. The photon noise comes from the light; and the transducer noise is from the chemical amplification process. Barlow [19] suggested that our percept comes from photon

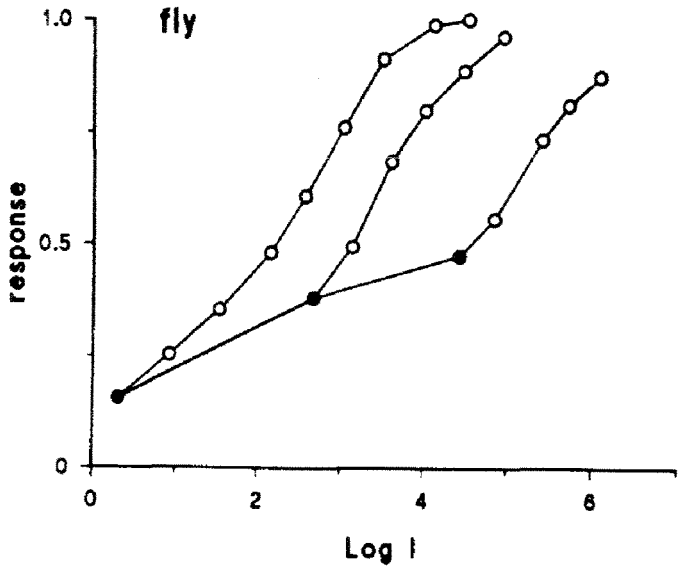

Figure 2.7: Plot of photoreceptor response versus log of intensity in the fly photoreceptors. The figure shows that the transient gain curve shifts over different background intensities. Source: From Laughlin [22], Figure 3, pg. 170.

counting, and the reliability of this counting in the behavioral response of organisms is limited by photon noise in the sensory input itself. The photon noise is classified as shot noise due to the random arrival of photons. The transducer noise is also called *dark noise* and is partly caused by the spontaneous isomerization of the photopigment rhodopsin due to thermal noise.

CCD and CMOS sensors are also subjected to the random Poisson process of photon arrival. The transducer noise gives rise to what is called *dark current* in the sensor terminology. Electron–hole pairs are generated by photons hitting the silicon substrate. The efficiency of the collection of electron–hole pairs is about 0.2 to 0.8, depending on the wavelength and the device structure. The current flowing in the transistors is also subjected to thermal noise, shot noise, and flicker noise. The thermal noise and shot noise can be characterized as Poisson events. Delbrück [20] has done a detailed characterization of the noise spectrum and the S/N ratio of silicon photoreceptors over various background intensities. The thermal noise and shot noise

in transistors are equivalent sources of noise, as shown by Sarpeshkar and colleagues [21].

2.4 Physiology of Receptors

The membrane potential of the receptors in the fly's eye depolarizes in response to an increase in the light intensity. This depolarization is unlike the response of the rods and cones in the vertebrate retina; they hyperpolarize with an increase in light illumination. The response range of the receptors varies over 60 to 80mV. At low light levels, the response reduces to the appearance of quantum bumps. The amplitude and duration of the bumps decrease under light adaptation. The physiological responses of photoreceptors have been studied by many researchers, including Laughlin [22], Juusola and colleagues [14], and Scholes [23]. Typical step and impulse responses of the photoreceptors are shown in Figure 2.6. Figure 2.6a shows the response of a dark-adapted photoreceptor to different light steps. Figure 2.6c and Figure 2.6d show the responses of a light-adapted photoreceptor to a 20ms and a 300ms contrast step respectively.

Both invertebrates and vertebrate photoreceptors adapt in response to light intensity. Otherwise, the receptors will saturate at high intensities. In fact, the gain per unit contrast is approximately constant at high intensities [24]. The shift in the response curves of the fly's photoreceptors over different intensities is shown in Figure 2.7. This shift shows that the photoreceptors are adapting to the background intensity; that ensures that the operating point of the photoreceptors will be sitting at the center of the curve where the contrast gain is the highest. As a result of light adaptation, the receptors are able to maintain a high transient gain over six to eight decades of intensities. Weckström and colleagues [25] showed that calcium channels and voltage-activated potassium channels are responsible for the time constant and adaptation in the photoreceptors.

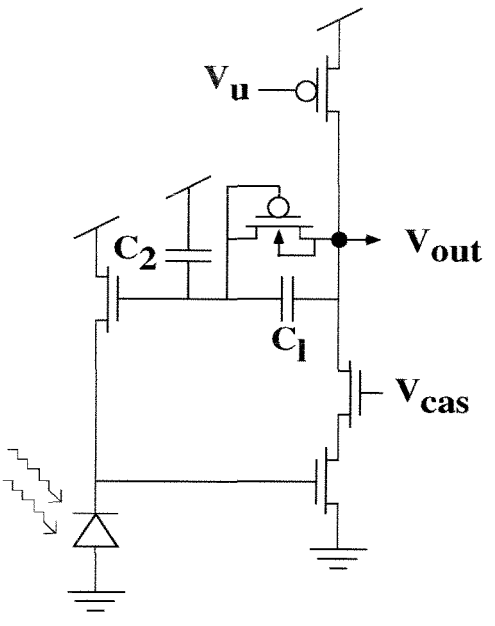

Figure 2.8: A silicon model of the photoreceptor responses by Delbrück. The transient gain of the circuit is determined by the ratio of the capacitors, $\frac{C_1+C_2}{C_1}$.

2.5 Receptor Modeling

The gain and phase responses of vertebrate receptors can be modeled by a cascade of filters as shown by Fuortes and Hodgkin [26]. They modeled the turtle cones by an RC filter with 7 to 10 stages of delay to account for the sharp high frequency cutoff in the gain plots. However, the output of the filter does not fit the data in the phase plot. The responses of invertebrate receptors can also be modeled by a cascade of filters. French [27] modeled the fly receptors by using a cascade of first-order and second-order filters. The output of the model fits the actual responses of the gain plot of the receptors but not the phase plot. Howard and Payne [12] modeled the responses of the invertebrate receptor as a nonlinear filter. The impulse response of the receptor can be approximated by the log-normal model with threshold to activate the ionic channels.

$$R(t) = e^{-log(t/t_p)^2/2w^2}$$

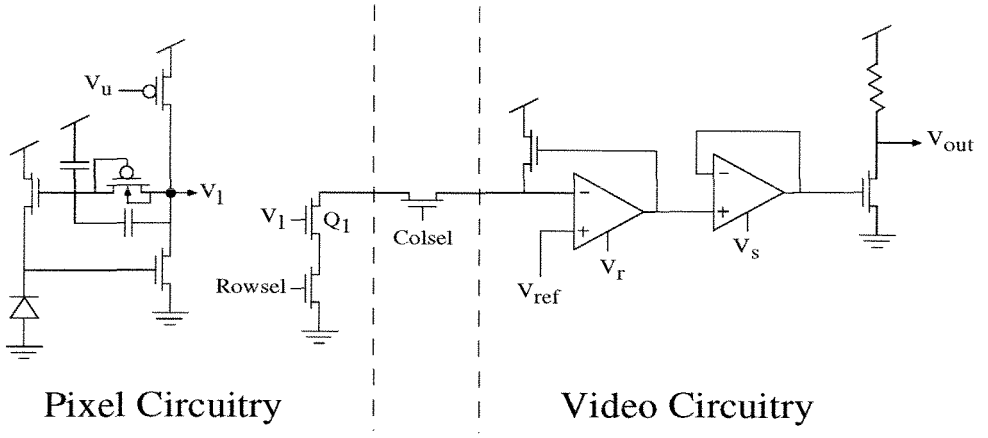

Figure 2.9: Circuitry showing the path from the pixel through the scanners in the columns and then through the video circuitry. Measurements are done at the output of the inverter.

where t_p is time to peak after a flash is delivered and w is a measure of the dispersion of t_p. The model fits the receptor's responses at low and medium backgrounds, but not at high light levels.

The silicon model of the photoreceptor by Delbrück is shown in Figure 2.8. This circuit models the adaptation responses of the biological photoreceptor to light intensities. A summary of how the circuit works is described in Section 3.4 of Chapter 3. The DC gain is defined by the κ of the transistor, where κ is the efficiency of the gate in controlling the surface potential of the transistor. The AC gain is defined by the ratio of the capacitors, C_1 and C_2 (i.e., AC gain=$(C_1 + C_2)/C_1$). This circuit is used in the pixel of the silicon retinae from which offset measurements are done, as described in Section 2.6. A movie of the output from one of these retinae consisting of 59×66 pixels can be found at the website http://www.pcmp.caltech.edu/anaprose/shih/shihretmovie.mpg. The movie was recorded with an image capture board from Precision Digital Images.

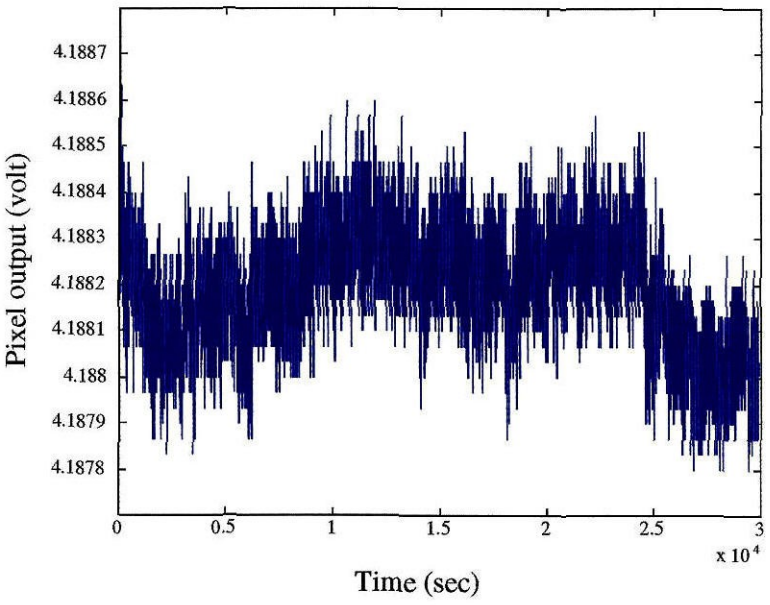

Figure 2.10: Voltage drift at a single pixel over time under constant lighting conditions.

2.6 Offset Distributions in the Silicon Retina

Both DC and AC offsets or mismatches are present in fly receptors. From Figure 2.7, two types of offsets can be inferred. One is the dc offset of the DC gain curve between the biological receptors and the other offset comes from the variation in the slopes of the DC gain curves and also that of the AC gain curves. Much like these offsets in neurons, the same type of offsets are present between pixels in silicon. Systematic offsets can be reduced by well-controlled processing, and by careful layout and circuit design. Since we frequently use commercially available CMOS technologies, process control is out of our hands. However, we can reduce offsets through careful circuit layout and design; or by using adaptation on a long time constant with tunneling-injection structures [28]. In this section, I measured the DC offsets and AC gain mismatches from two different silicon retinae with Delbrück's receptor pixels. The layouts of the pixels in the two retinae are different, and the retinae were processed on different runs by the MOSIS foundation. I obtained the DC offsets by exposing the retina to uniform lighting from an LED source; I obtained the AC gain mismatches

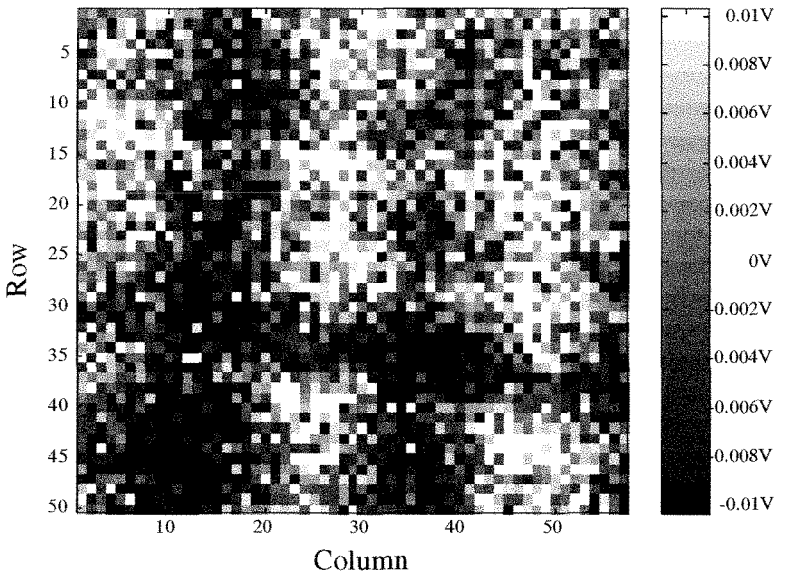

Figure 2.11: Plot showing the DC offsets distribution in a retina with 59×66 pixels. The pixel outputs were measured in the presence of a constant background intensity.

by exposing the retina to an LED driven by a square wave of varying intensities and varying contrasts.

2.6.1 Thermal Drift and DC Offsets to Uniform Lighting

The first set of results was obtained from a retina with 59×66 pixels. Figure 2.9 shows the circuitry along the path from the phototransduction stage to the measured output. The offsets of all the transistors along the path add up to the offsets observed at the output. The circuitry in each pixel is shown on the extreme left of Figure 2.9. The pass transistor in the middle of the figure is part of the circuitry in the scanners at the bottom of the retina and the video circuitry on the extreme right is at the output of the scanners. Details of the circuitry for scanning out the pixels in the array have been described by Mead and Delbrück [29][30]. Since all the pixels encounter the same video circuitry, we can assume that the offsets at the output are due to offsets between the pixels.

First, the output from a single pixel in the silicon retina was recorded over a period

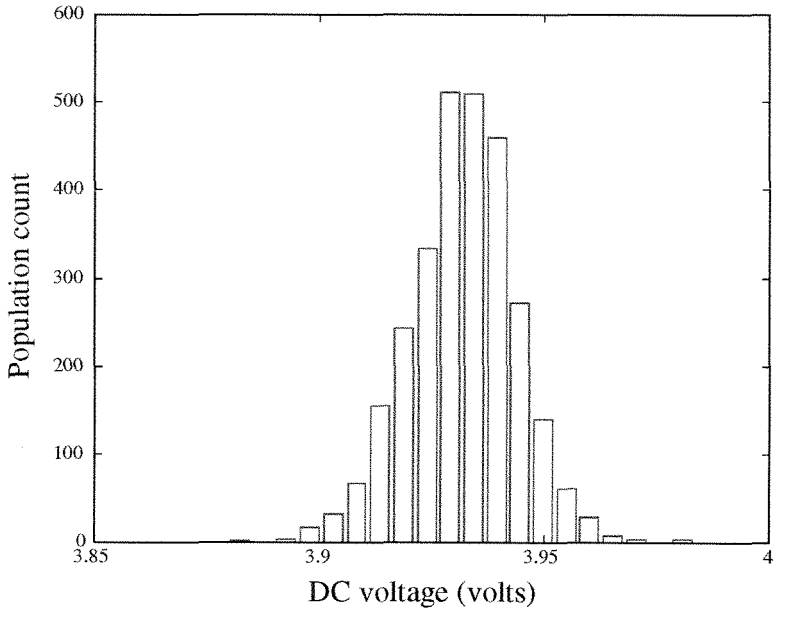

Figure 2.12: Histogram of DC response of retinal pixels to a constant background intensity. The standard deviation of the distribution is 12.1mV.

of more than 24 hours. An incandescent bulb driven by a DC source was mounted about 1 foot over the chip. Figure 2.10 shows the drift of this pixel over this time. The p–p variation in the pixel output is only about $\pm$5mV, and is due primarily to thermal noise and flicker noise. The sources of noise in transistors are discussed by Delbrück [20] and by Sarpeshkar and colleagues [21]. This variation in the output of a single pixel over time is smaller than the DC offset distribution in the array.

I obtained the DC offsets in the retina by using a green LED as the stimulus. For each pixel, the average of six readings was recorded. The mean of all the pixels was computed and then subtracted from each pixel, and the resulting output was plotted in Figure 2.11. The distribution of pixel outputs corresponds to the DC offsets between the pixels. From Figure 2.11, we can also see the systematic offsets (evident from the three strips) caused by the silicon processing. The histogram of the DC offsets is shown in Figure 2.12. The standard deviation of this histogram is about 12.1mV. This deviation is equivalent to a contrast of about 0.25 as computed from the DC gain of the pixel, which is 50mV/decade of intensity. The definition

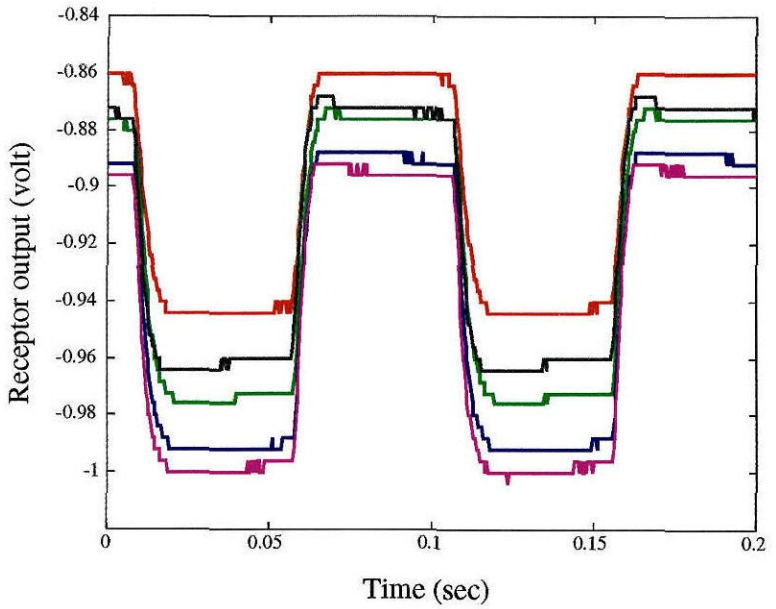

Figure 2.13: A sample of the responses of the pixels in the retina to a blinking LED. The figure shows the variations in the maximum and minimum outputs of the pixels.

of contrast here and in the remainder of this dissertation is defined as the difference of the maximum and minimum intensities over the sum of these intensities (i.e., $(I_1 - I_2)/(I_1 + I_2)$). We can also see that the drift from a single pixel over time is smaller than the DC offsets in the retina.

2.6.2 AC Gain Mismatches

The magnitude of the AC gain mismatches is critical as the AC output of the receptor represents changes in the visual input. Large AC mismatches between the pixels would degrade subsequent computations involving neighboring pixels. I calibrated the AC gain mismatches in the silicon retinae by measuring the p–p responses of the pixels to an LED that was modulated by a 10Hz square wave. The offsets were recorded for five modulations of the LED. Figure 2.13 shows a sample of the step responses of the pixels in the retina to a stimulus of contrast 0.09. For each LED modulation, the average of 128 readings from each pixel was recorded; the responses after removal of the mean of all the pixels are shown in Figure 2.14. Surprisingly, the p–p variation between

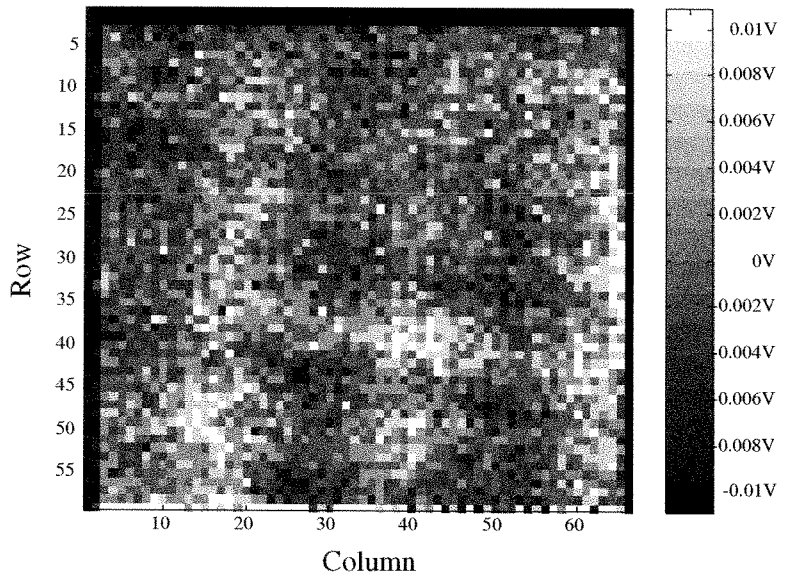

Figure 2.14: 2d image of p–p offset distribution in retina in response to a blinking LED of contrast 0.09.

the pixels was about 6 percent, which is larger than I expected. This variation can also be seen from the histogram of the distribution of the responses in Figure 2.15. The p–p response depends on the AC gain of the pixel, and this gain is the ratio of the capacitors, C_1 and C_2, in Figure 2.8. The capacitor matching in silicon is usually about 1 to 3 percent for capacitors of the size used in our receptors [31]. These large gain mismatches are also seen in the results from the next four modulations as shown in Figure 2.16.

A possible reason for the larger–than–expected mismatches might be that the offset of the readout transistor, Q_1, in Figure 2.9, is large. The evidence comes from the similarity in the AC offset pattern in Figure 2.14 and the DC offset pattern in Figure 2.11. As it turns out, the readout transistor has a minimum transistor length of 2μm in this layout. This small transistor length leads to large variations in the output response. The threshold variations for such a small transistor length creates about a 5mV offset. Since the transistor is operated in subthreshold, this offset leads to large variations in the output current.

If we assume that the AC gain mismatch data are dominated by the offset of

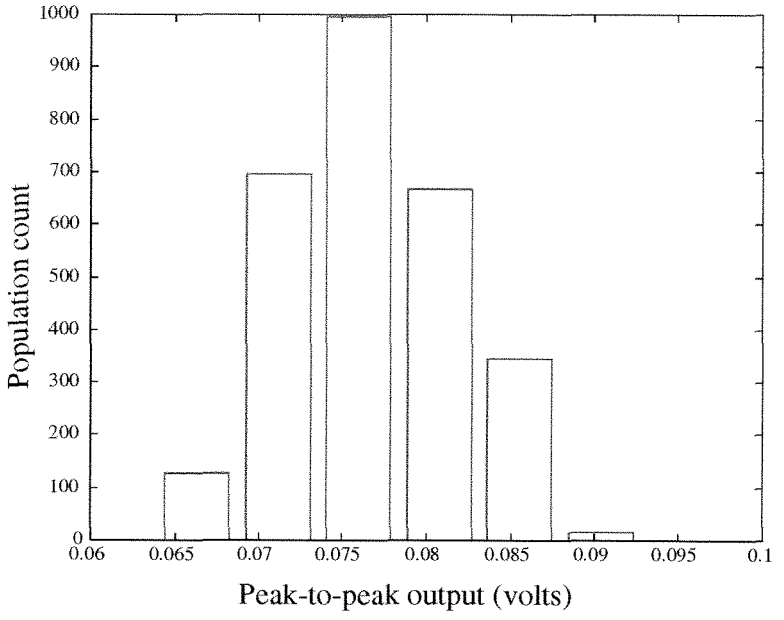

Figure 2.15: Histogram of p–p response of retinal pixels in response to a blinking LED of contrast 0.09.

the readout transistor, we can try to compute the latter offset from these data. We can then remove the readout transistor's offset from the DC offset data to obtain the actual DC offsets. Assuming that the variances (or random variables) of the transistors are independent of one another, then the DC variance, σ_{dc}^2, is the sum of the DC variance from the receptor circuit, σ_{pdc}^2, and the variance from the readout transistor, σ_r^2. Correspondingly, the AC variance, σ_{ac}^2, is the sum of the AC variance from the receptor circuit, σ_{pac}^2, and the variance from the readout transistor. Hence,

$$\sigma_{dc}^2 = (\sigma_{pdc}^2 + \sigma_r^2)G \tag{2.1}$$

and

$$\sigma_{ac}^2 = (\sigma_{pac}^2 + \sigma_r^2)G, \tag{2.2}$$

where G is the gain through the video circuitry.

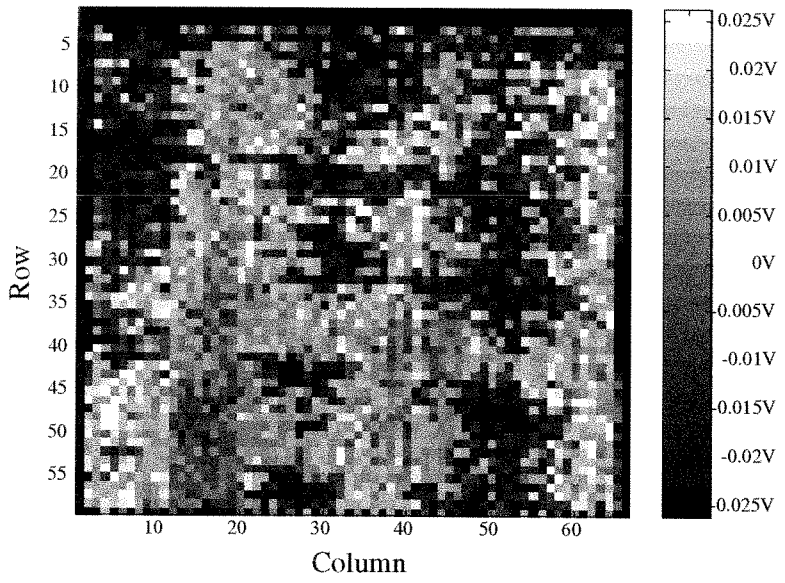

Figure 2.16: 2d image of p–p offset distribution in retina in response to a blinking LED of contrast 0.15.

The AC gain of the receptor, g_p, is given by

$$g_p = \Delta v / \frac{\Delta I}{I} = \frac{C_1 + C_2}{C_1} \frac{\mathrm{U_T}}{\kappa}, \tag{2.3}$$

where Δv is the receptor response to a contrast of $\frac{\Delta I}{I}$ and $\mathrm{U_T}$ is the thermal voltage. Here, ΔI is the modulation in the light intensity, I. We assume that the variances from the contrast, the capacitors, κ, and $\mathrm{U_T}$, are dominated by the variance from the readout transistor, σ_r. Hence, $\sigma_{ac} = \sigma_r$. This assumption is valid because we know that the capacitor mismatches are small in silicon and that κ does not differ significantly across the pixels. The mean of the responses to the contrast, $\frac{\Delta I}{I}$, is given by $\Delta v = \frac{\Delta I}{I} g_p$. The coefficient of variation (CV) of the distribution can be defined as

$$\mathrm{CV} = \frac{\sigma_{ac}}{\mathrm{mean}} = \frac{\sigma_r}{\frac{\Delta I}{I} g_p}.$$

The CVs for five different contrast values (0.0896, 0.101, 0.1124, 0.1241, and 0.1483) are plotted against the inverse of the contrast in Figure 2.17. The slope of

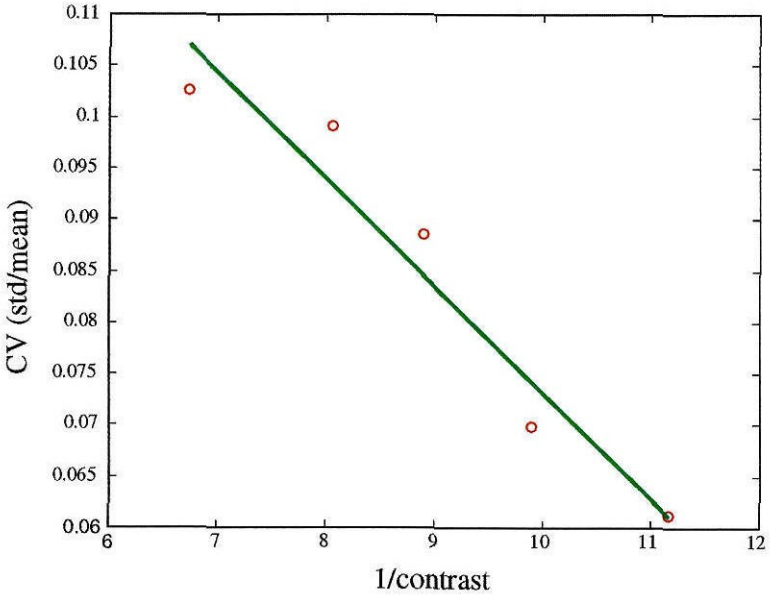

Figure 2.17: Plot of the coefficient of variation of the AC offset data against the inverse of the contrast.

the linear fit to the points in the figure is -0.0104. The standard deviation, σ_r, is then $0.0104 * g_p$. From the layout, the capacitor ratio is 8.53, and we assume a κ of 0.5. The standard deviation for the readout transistor is then 4.5mV. We have seen that the standard deviation of the DC offsets is 11.8mV. If we subtract the variance of the readout transistor from the variance of the DC offset measured, we should get the actual variance of the DC offset. In this case, it is 10.9mV.

2.6.3 Comparison Between Offsets in the Silicon Retina and the Fly Retina

How do the offsets in our retinae compare with those of the fly retina? Shown in Table 2.2 are the means and standard deviations of the AC gain mismatches measured in the silicon retina for the five different contrast values and the offsets from the fly retina. I obtained the numbers in the rightmost column by taking the CV percentage of each measurement. The numbers gives us an idea of how big the standard deviation is as compared to the mean. For larger responses in the receptor output, we expect

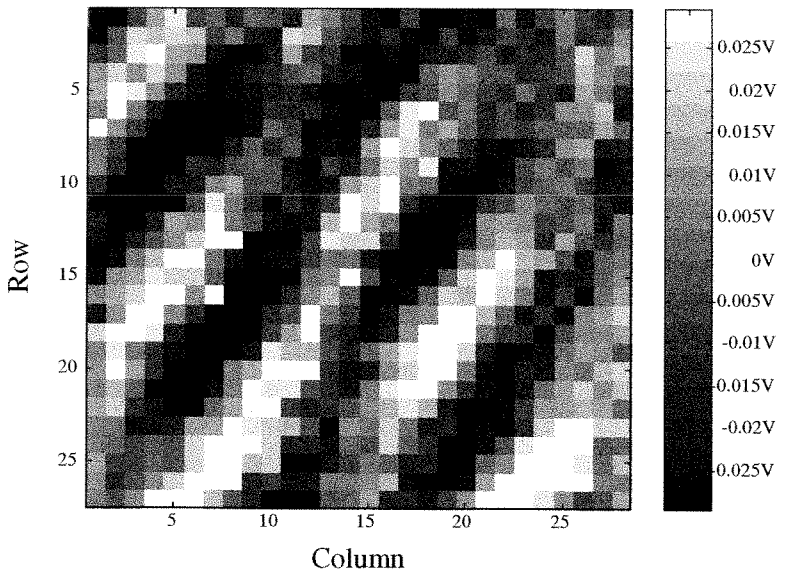

Figure 2.18: 2d image of DC offset distribution in retina under uniform lighting conditions.

the deviation in the responses also to be larger. The data for the fly receptors were obtained from the work of Juusola [32] who measured the responses of fifty-four R1-6-type receptors. The responses from each receptor were averaged 20 to 1000 times. The intensity numbers in the Table 2.2 for the fly receptors are measured in terms of effective photons/sec. The contrast in Juusola's work is defined as $I_{\max}/I_{\min}$.

If we compare the rightmost column between responses of the silicon receptors and those of the fly receptors, we see that the percentage variation is lower for the fly receptors that for the silicon receptors in this retina. As we will see in Section 2.6.4, the percentage variation of the responses in the second silicon retina is comparable to that of the fly receptors.

2.6.4 DC Offsets and AC Gain Mismatches in the Second Retina

We can test our theory that the offsets are dominated by the offsets of the readout transistor by taking the same measurements from a 32×32 silicon retina whose pixel

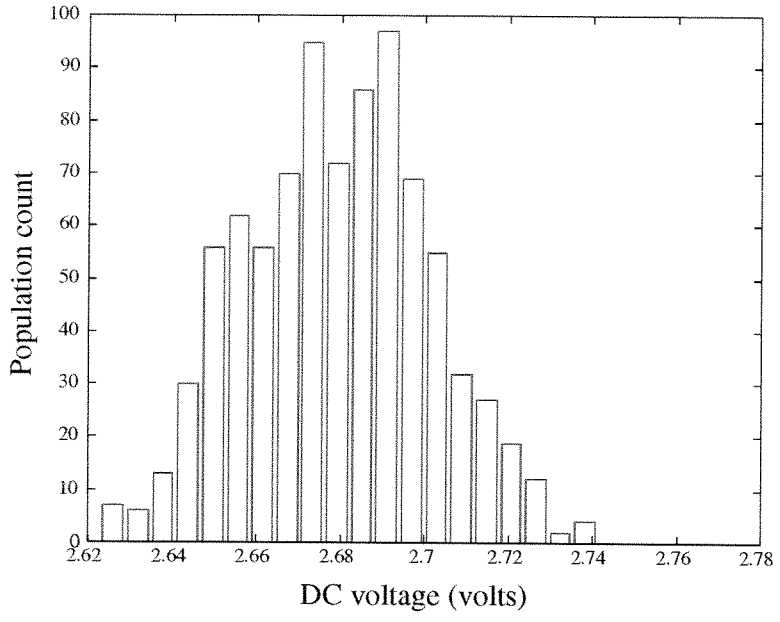

Figure 2.19: Histogram of steady-state response of pixels in the 32x32 array under uniform lighting conditions.

has a longer transistor length, 19μm. Figure 2.18 shows the DC offsets distribution in the retina; the histogram of this distribution is shown in Figure 2.19. From Figure 2.19, we can see that the standard deviation is now 21mV. The higher standard deviation probably occurs because of the different processing run. The DC gain from the pixel is 48mV/decade of intensity; hence, the deviation corresponds to a contrast of about 0.46. The systematic offsets seen in the first retina are also obvious in this retina.

The AC gain mismatches were measured at four different contrasts, as shown in Table 2.3. Figure 2.20 shows a sample of the step responses of the pixels to an LED of contrast 0.134. The variations in the maximum and minimum outputs of the pixels is smaller when compared to that in Figure 2.13. The distribution of the AC gain mismatches from the entire chip is shown in Figure 2.21. The histogram of the distribution is shown in Figure 2.22. Now as expected, the variation in the AC offsets is about one–half as much as the variation recorded in the first silicon retina. It proves that the AC offsets that we observed in the first retina were due to the offsets

Table 2.2: Comparison of Offsets in Silicon and Fly Receptors

Material	Contrast	Intensity(ph/s)	Mean(mV)	Std Dev(mV)	Variation(%)
Silicon	0.0896	2×10^{11}	76.8	4.7	6
Silicon	0.1018	2×10^{11}	87.3	6.1	7
Silicon	0.112	2×10^{11}	99.3	8.8	8.8
Silicon	0.124	2×10^{11}	106.9	10.6	9.9
Silicon	0.148	2×10^{11}	147.1	15.1	10.3
Calliphora	1.12	5000	4.1	0.2	4.8
Calliphora	-1	5000	-8.9	0.5	5.6
Calliphora	1.12	5×10^{5}	7.9	0.4	5
Calliphora	-1	5×10^{5}	-22.5	2.6	11.55

Table 2.3: Offsets in Second Silicon Retina

Contrast	Intensity(ph/s)	Mean(mV)	Std Dev(mV)	Variation(%)
0.031	2×10^{11}	50.6	2.7	5.3
0.075	2×10^{11}	97.9	3.2	3.2
0.102	2×10^{11}	145.8	3.5	2.4
0.134	2×10^{11}	195	4.2	2.15

in the readout transistor. It also illustrates that careful circuit design and layout are critical in reducing the offsets in silicon. The variation in the second retina is also now comparable to that of the fly receptors, as we can see by comparing the data in Table 2.2 with those in Table 2.3. Of course, if the receptor output was used directly by other processing circuitry within the pixel, the offsets of the readout transistor would not have played a part in the subsequent computation.

The DC offsets can be ignored if the receptor output is AC-coupled to the gate of the next transistor. However, it is not clear that this coupling is carried out in the neurons or synapses. Neurons are considered to be imprecise computational elements; yet the offset distribution between different receptors is amazingly small.

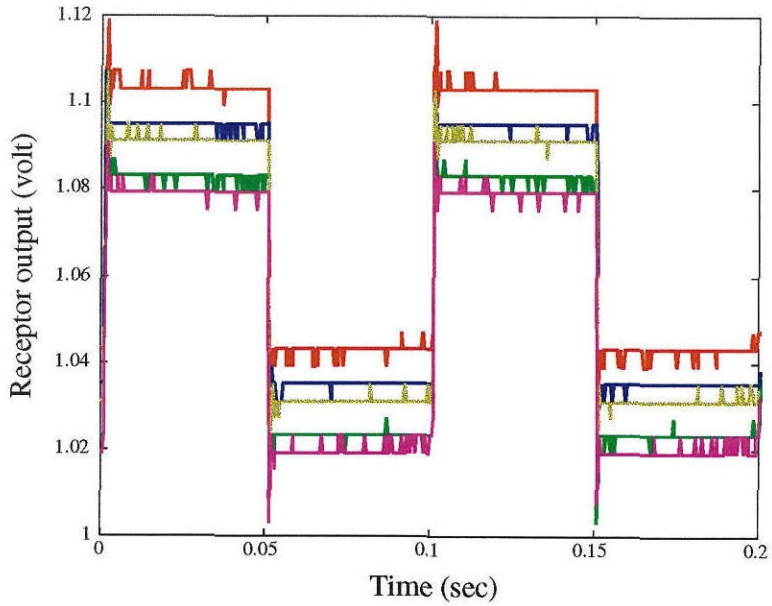

Figure 2.20: A sample of the step responses of the pixels in the second retina to an LED of contrast 0.134. The figure shows the variations in the maximum and minimum outputs of the pixels.

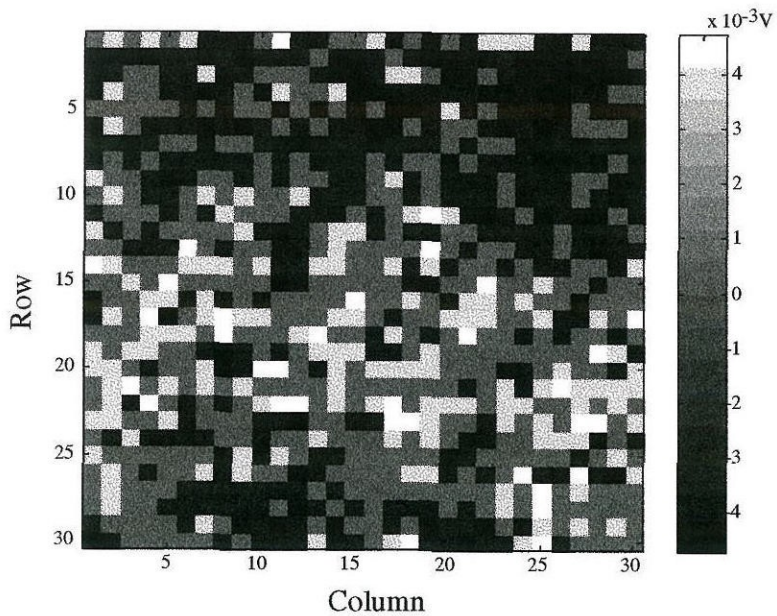

Figure 2.21: 2d image of p–p offset distribution in retina in response to a blinking LED of contrast 0.134.

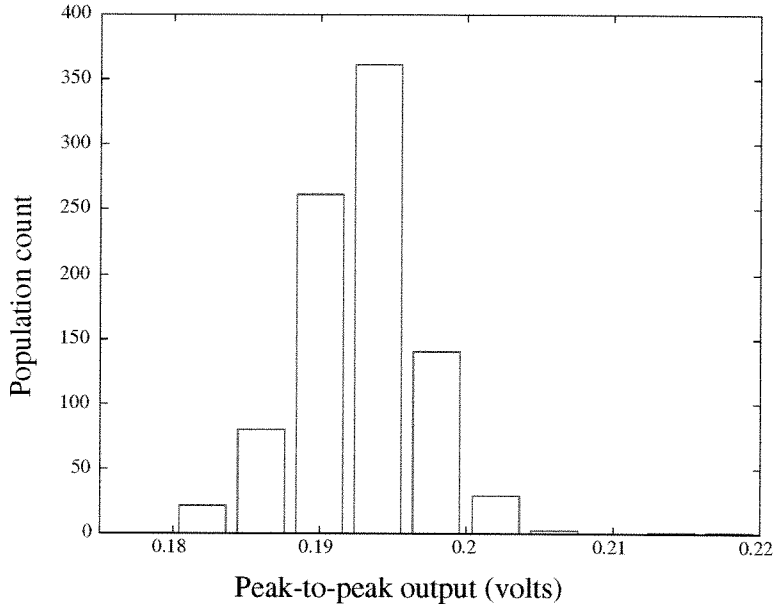

Figure 2.22: Histogram of p–p offset distribution in response to a blinking LED of contrast 0.134.

Bibliography

[1] K. Kirschfeld, "Die projektion der optischen Umwelt auf das Raster der Rhabdomere in Komplexauge von *Musca*," *Exp. Brain Res.*, **3**, pp. 248–270, 1967.

[2] K. Kirschfeld, "The visual system of Musca: Studies on optics, structure and function," *Information Processing in the Visual Systems of Arthropods*, R. Wehner, Editor, pp. 61–74, Springer–Verlag, Berlin, Heidelberg, New York, 1972.

[3] D. G. Stavenga, "Pseudopupils of compound eyes," in *Handbook of Sensory Physiology Vol VII/6A*, H. Autrum, ed. Springer-Verlag, Berlin, Heidelberg, New York, pp. 357–439, 1979.

[4] S. Shaw, "Anatomy and physiology of identified non-spiking cells in the photoreceptor-lamina complex of the compound eye of insects, especially *Diptera*," in *Neurones without Impulses*, A. Roberts and B. Bush, Editors, pp. 61–116, Cambridge Univ. Press, Cambridge, 1981.

[5] S. Shaw, "Early visual processing in insects," *Journal of Expt Biology*, **112**, pp. 225–251, 1984.

[6] K. Kirschfeld, "The resolution of lens and compound eyes," in *Neural Principles in Vision*, F. Zettler and R. Weiler, Editors, pp. 354–370, Springer–Verlag, Berlin, 1976.

[7] A. Snyder and W. H. Miller, "Photoreceptor diameter and spacing for highest resolving power," *J. Opt. Soc. Am.*, **67:5**, pp. 696–698, 1977.

[8] J. Howard and A. Snyder, "Transduction as a limitation on compound eye function and design," *Proc. R. Soc. Lond. B*, **217**, pp. 287–307, 1983.

[9] S. Laughlin, "Neural principles in the visual system," in *Handbook of Sensory Physiology Vol VII/6B*, H. Autrum, ed. Springer-Verlag, Berlin, Heidelberg, New York, pp. 133–280, 1981.

[10] R. M. Glantz, "Motion detection and adaptation in crayfish photoreceptors," *J. Gen. Physiol.*, **97**, pp. 777–797, 1991.

[11] A. Snyder, "Acuity of compound eyes: physical limitations and design," *J. Comp. Physiol.*, **116**, pp. 161–182, 1977.

[12] R. Payne and J. Howard, "Response of an insect photoreceptor: a simple log-normal model," *Nature*, **290**, pp. 415–416, 1981.

[13] J. Howard, B. Blakeslee, and S. B. Laughlin, "The intracellular pupil mechanism and photoreceptor signal:noise ratios in the fly *Lucilia cuprina*," *Proc. of Royal Society of Lond. B*, **231**, pp. 415–435, 1987.

[14] M. Juusola, R. O. Uusitola, and M. Weckström, " Transfer of graded potentials at the photoreceptor-interneuron synapse," *J. of General Physiology*, **105**, pp. 115–148, 1995.

[15] J. G. Smakman, J. H. van Hateren, and D. Stavenga, " Angular sensitivity of blowfly photoreceptors: intracellular measurements and wave-optical predictions," *J. of Comp. Physiol. A*, **155**, pp. 239–247, 1984.

[16] R. Sarpeshkar, J. Kramer, G. Indiveri, and C. Koch, "Analog VLSI architectures for motion processing - from fundamental limits to system applications," *Proceedings of the IEEE*, **84:7**, pp. 969–987, 1996.

[17] A. J. P. Theuwissen, "Solid-state imaging with charge-coupled devices," Kluwer Academic Publishers, Boston, 1995.

[18] A. W. Snyder, S. B. Laughlin, and D. G. Stavenga, "Information capacity of eyes," *Vision Research*, **17**, pp. 1163–1175, 1977.

[19] H. B. Barlow, "Retinal noise and absolute threshold," *J. Opt. Soc. Am.*, **46**, pp. 634–639, 1956.

[20] T. Delbrück, "Analog VLSI phototransduction by continous-time, adaptive, logarithmic photoreceptor circuits," CNS Memo No.30, California Institute of Technology, Pasadena, CA, 1994.

[21] R. Sarpeshkar, T. Delbrück, and C. A. Mead, "White noise in MOS transistors and resistors," *IEEE Circuits and Devices*, **9:6**, pp. 23–29, 1993.

[22] S. B. Laughlin, "Matching coding, circuits, cells, and molecules to signals - General principles of retinal design in the fly's eye," *Progress in Retinal and Eye Research*, **13:1**, pp. 165–196, 1994.

[23] J. H. Scholes, "The electrical response of the retinal receptors and the lamina in the visual system of the fly *Musca*," *Kybernetik*, **6**, pp. 149–162, 1969.

[24] F. Zettler, "Die Abhängigkeit des Ubertragungsverhaltens von Frequenz und Apatationszustand, gemessen am einzelnen Lichtrezeptor von *Calliphora erythrocephala*," *Z. Vergl. Physiol.*, **64**, pp. 432–449, 1969.

[25] M. Weckström, R. C. Hardie, and S. B. Laughlin, "Voltage-activated potassium channels in blowfly photoreceptors and their role in light adaptation," *J. Physiol. Lond.*, **440**, pp. 635–657, 1991.

[26] M. G. H. Fuortes, and A. L. Hodgkin, "Changes in time scale and sensitivity in the ommatidia of *Limulus*," *J. Physiol.*, **172**, pp. 239–263, 1991.

[27] A. French, "Phototransduction in the fly compound eye exhibits temporal resonances and a pure time delay," *Nature*, **283**, pp. 200–202, 1980.

[28] P. Hasler, "Foundations of learning in analog VLSI," *Ph.D. Thesis*, California Institute of Technology, Pasadena, CA, 1997.

[29] C. Mead and T. Delbrück, "Scanners for visualizing activity of analog VLSI circuitry," *Analog Integrated Circuits and Signal Processing*, **1**, pp. 93–106, 1991.

[30] K. Boahen, "Retinomorphic vision systems: reverse engineering the vertebrate retina," *Ph.D. Thesis*, California Institute of Technology, Pasadena, CA, 1997.

[31] B. A. Minch, C. Diorio, P. Hasler, and C. A. Mead, "The matching of small capacitors for analog VLSI," *Proceedings of the 1996 International Symposium on Circuits and Systems*, **3**, pp. 325–328, 1996.

[32] M. Juusola, " Linear and non-linear contrast coding in light-adapted blowfly photoreceptors," *J. of Comp. Physiol. A*, **172**, pp. 511–521, 1993.

[33] N. Franceschini, "Early processing of colour and motion in a mosaic visual system," *Neuroscience Research, Suppl. 2*, pp. S17-S49, 1985.

Chapter 3 Laminar Modeling

The receptors, R1 to R6, project sign-inverting synapses onto the monopolar cells in the lamina. The monopolar cells carry out a similar role to that of the bipolar cells in the OPL of the vertebrate retina. The spatiotemporal filtering properties in both cells are similar, except that the temporal factor is more dominant than the spatial factor in the monopolar cells. The monopolar cells remove the DC of the receptor output, and amplify the remaining signal to cover the full response range of the cells. The cells also remove redundancy in the temporal domain by responding transiently to signal changes. This transient behavior corresponds to self-inhibition. The spatiotemporal filtering changes with the S/N ratio, such that the bandpass filtering of the LMCs changes to lowpass under low light conditions.

In this chapter, I describe a small, compact **retino-laminar** (RL) circuit that captures the automatic local gain control properties of the receptor and **adaptive filtering** properties of the monopolar cells. The cutoff frequencies of the bandpass filtering of this circuit shift with the S/N ratio, such that in the range of 1 to 100 Hz (within the operating range of the LMCs), the circuit response changes from a highpass under high S/N conditions to a lowpass under low S/N conditions. This chapter presents three different variants of the RL circuit and shows the dependence of the frequency response of these variants on the background intensity. The adaptation time constant of the circuit is controllable via an external bias, and the adaptation behavior of the circuit over different background intensities is more symmetrical than that of Delbrück's photoreceptor circuit.

3.1 Anatomy of Laminar Layer

As we saw in Chapter 2, the first visual ganglion is the lamina. It consists of an array of retinotopically arranged cartridges, where each cartridge receives axons from six

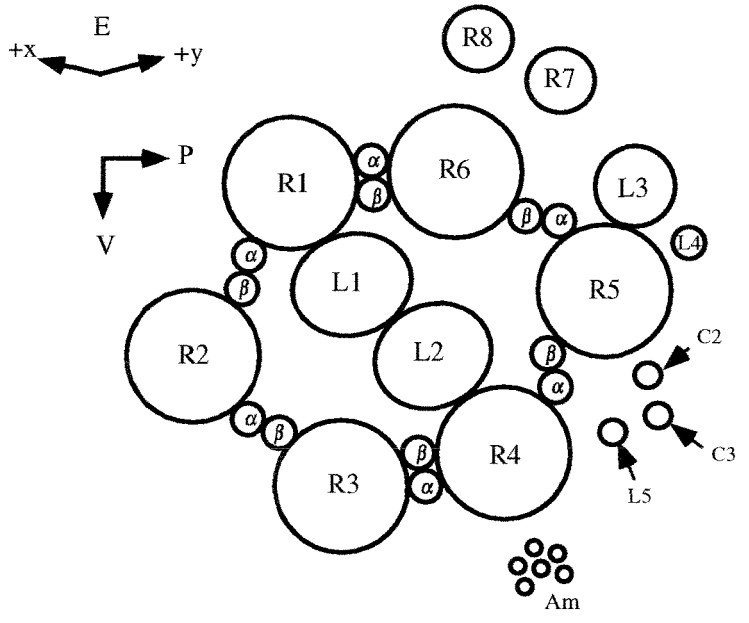

Figure 3.1: Cross-section of the cells in a cartridge of a fly, showing the the arrangement of the monopolar cells, L1 to L5, the receptor cells, R1 to R6, the centripetal cell, T_1, and the centrifugal cells, C_2 and C_3. The figure also shows the α processes of the amacrine (Am) cells and the β processes of T_1. P: posterior, V: ventral. Source: Adapted from Meinertzhagen [3], Figure 42, pg 255.

rhabdomeres with the same visual axes from neighboring ommatidia. In addition to the photoreceptor axons, each cartridge also contains a set of five centripetal first-order interneurons, called monopolar cells (L1-L5); the basketlike arborizations (β-fibers) of the centripetal T_1-cell and two small-field centrifugal elements (C_2, C_3), derived from the corresponding column in the medulla (the second visual ganglion). A simple cross-section of a cartridge is shown in Figure 3.1. There are about 14 neuronal classes of cells in the lamina. The intricate connection of these cells has been described in detail [1][2][3][4][5]. Lateral connections between neighboring cartridges are mediated by two wide-field centrifugal cells (Tan 1, Tan 2) and by the lamina

amacrine cells. The former link the medulla to the lamina. The latter reside within the lamina and provide each cartridge with the α-fibers. Adjacent cartridges are also connected by a regular network of collaterals emerging from the L4 monopolars.

Here, we only describe the synaptic connections between the receptors and the output cells in the lamina, L1 and L2. The receptors, R1 to R6, synapse onto only L1, L2 and L3. L1 is a pure output element, whereas L2 feedbacks onto R1 to R6. The tetrad synapse consisting of the receptors, L1, L2, and an α process, is the most common synapse in the cartridge. There are about 1200 of these synapses per cartridge. Each cartridge is surrounded by three epithelial glial cells (EGCs). Both α and β processes are presynaptic to the EGCs. Some researchers believe that they may have the function of controlling and blocking the extracellular route between cartridges, and that they could form an intracellular route for translaminar current [4]. The cartridges also have gap junctions among each other through the epithelial glial cells.

3.2 Physiology of LMCs

The physiology of LMCs has been expounded by various researchers [6][7][8][9]. We describe only the responses of L1 and L2 cells, which are postsynaptic to the receptor cells. The responses of L1 and L2 are similar to each other. Their resting potential is between -35 to -45mV, and the full response range covers about 50mV. The response curves shift with the background intensity as shown in Figure 3.2. Because of the amplification of the signal at the photoreceptor-LMC synapse (≈ 6), the slope of the curves in Figure 3.2 is greater than that of the receptor curves. The dynamic range of the LMCs is about 2.3 log units. When the receptors depolarize in response to a brief flash of light, the LMCs respond with a transient hyperpolarization. The hyperpolarization is generated by the release of a fast transmitter, histamine, from the receptors. Histamine activates the histamine-gated chloride channels in the postsynaptic LMC, thus generating a transient hyperpolarization in the LMC. In the case of the dark-adapted LMCs, the response is monophasic approaching that of a lowpass

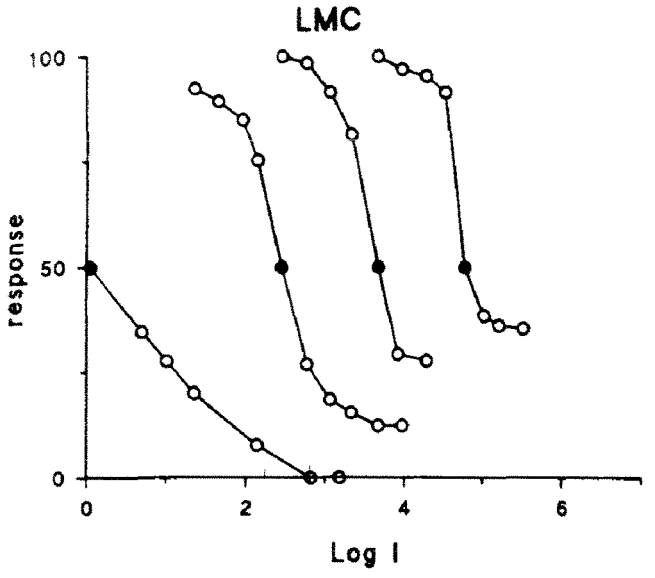

Figure 3.2: Plot of LMC response versus log of intensity. The figure shows that the transient gain curve shifts over different background intensities and the DC gain is zero. Source: From Laughlin [6], Figure 5, pg 171.

filter. With light adaptation, the response of the LMC becomes more transient and biphasic as shown in Figure 3.3. Figure 3.3b shows the response of a LMC in a dark-adapted condition to different light intensities, while Figure 3.3e and 3.3f show the response of the LMC to a 20ms and a 300ms contrast step. The depolarization of the LMC is due partially to a reduction in the synaptic input from the photoreceptor [7] and partially to a secondary effect of the changes in depolarizing conductances with positive reversal potentials.

The spatial receptive field of the LMCs varies with the background intensity [7][10][11]. At high intensities, the LMC demonstrates lateral inhibition through its center-surround receptive field. The surround is much shallower than that of bipolar cells in the OPL showing inhibition in the spatial domain is weaker than inhibition in the temporal domain. The surround can be generated by the extracellular space of the lamina [4]. This space depolarizes in response to light, because the photocurrent injected into the lamina must return to the retina by crossing epithelial glial

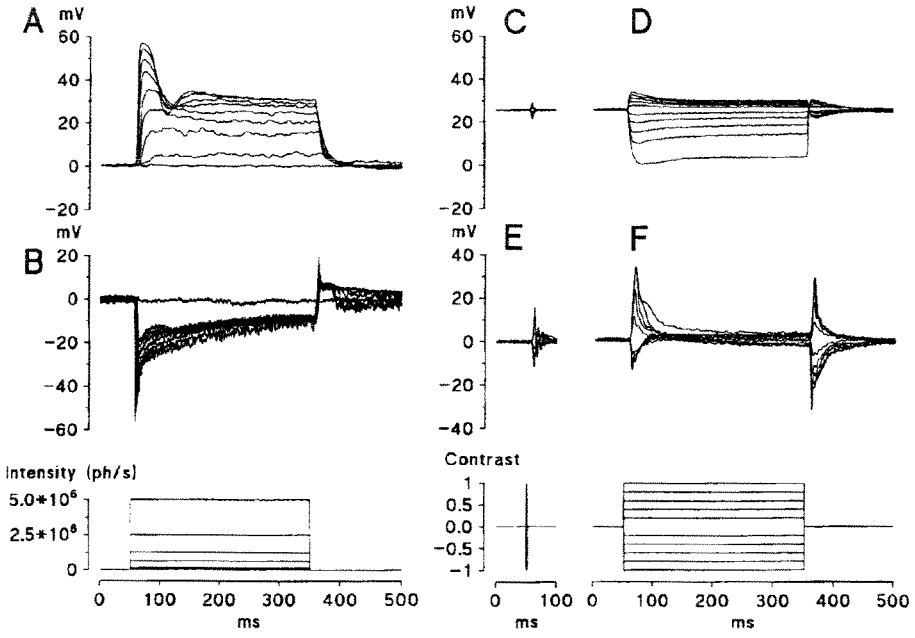

Figure 3.3: Recordings from a photoreceptor and a LMC in *Calliphora*. Step response of a dark-adapted photoreceptor (A) and a LMC to a 300ms light step. On the right are responses of a light-adapted photoreceptor (C) and a LMC (E) to a 20ms contrast step and to a 300ms contrast step (D and F respectively). Source: From Juusola and colleagues [8], Figure 2, pg. 122.

cells. Laughlin [6] models the inhibition in the LMCs by the log–subtract–amplify strategy. The weak center-surround antagonism of the LMC receptive field subtracts an estimate of the local mean from the signal. The remainder is then amplified to fill the LMC dynamic range. The background is removed so that full response range can be used. This strategy maximizes the information uptake to the LMCs from the receptors. Juusola and colleagues [12] recently characterized the kernels of the receptors and the LMCs by a second-order Volterra series. The kernels obtained are least-squares estimates, where the estimates are first-order and second-order Wiener kernels. From this estimate, they found that photoreceptor responses were approximately linear, while the LMC responses are nonlinear. The synaptic relationship between the receptor and the LMC is modeled as a nonlinear-linear-nonlinear cascade.

3.3 Role of Laminar Monopolar Cells

Different theories have been proposed for the function of the spatiotemporal properties of the LMCs. Laughlin and Hardie [13] suggested that the lateral and temporal inhibition in the LMCs is a mechanism to retrieve and amplify the contrast information from the receptors. Another theory for the function of the LMCs is by Srinivasan and colleagues [14], who used the predictive coding scheme to remove redundancy in the image. They were able to show that the form of the filters predicted by this scheme matches the spatial and temporal antagonistic fields of the LMCs. The lateral inhibition removes the existing redundancy in the image created by the spatial correlations between neighboring pixels. The temporal inhibition suppresses any response to a static signal. The hypothesis that the role of the early visual stages is to reduce redundancy was first advocated by Barlow [15]. Srinivasan and colleagues [16], later, suggested another hypothesis where they used the theory of matched filters to determine the filters needed to match the spatiotemporal distribution of the input stimulus. Their analysis showed that the LMCs are optimized to detect moving blobs at low S/N and to detect moving edges at high S/N.

Recently, van Hateren [17][18][19] suggested a theory that takes into account the spatiotemporal structure of natural scenes. The theory predicts the filters that would maximize the information flow through a noisy channel of limited dynamic range. The theory also predicts the change in spatiotemporal filtering under different S/N conditions. The predicted filters reduce redundancy at high S/N ratios, but increase redundancy at low S/N ratios. The filters exhibit the lowpass characteristics of the dark-adapted LMC and the highpass or bandpass characteristics of the light-adapted LMC. The bandpass characteristic comes about because it would pass along frequencies with decent S/N ratios. The reason for this is that information is proportional to the logarithm of the S/N. Hence, low frequencies are attenuated, so they don't occupy too much of the dynamic range, and high frequencies are attenuated since their S/N ratio is low.

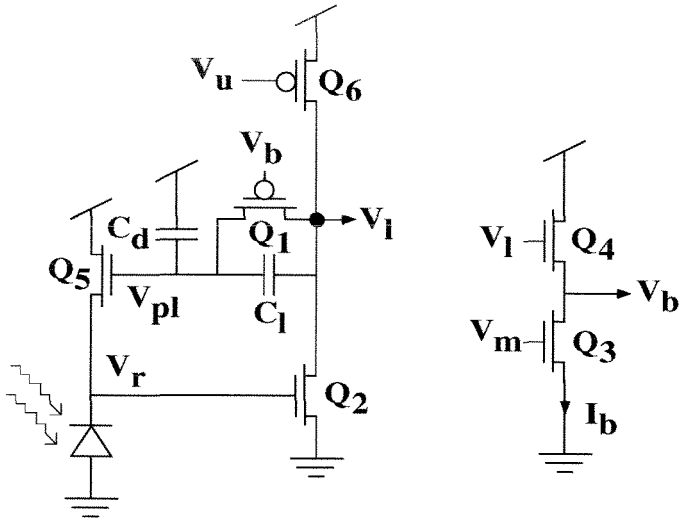

Figure 3.4: Circuit diagram of retino-laminar circuit (also RL_1). The feedback consists of a resistor implemented by a pFET transistor, Q_1. The conductance of the resistor is controlled by the external bias, V_m.

3.4 Circuit Description

In this section, I describe a small, compact, circuit model of the adaptation properties of the receptor and the adaptive filtering properties of the monopolar cells. The circuit is called the **retino-laminar** circuit (RL) since it captures properties of both the retina and the lamina. The RL circuit is shown in Figure 3.4. Here, I have replaced the adaptive element in Delbrück's receptor circuit [20] (shown in Figure 2.8, Chapter 2) by a nonlinear resistor consisting of a pFET transistor, Q_1. The implementation of a floating, voltage-controlled resistor has been described earlier by Banu and Tsividis [21]. The bias for the pFET, V_b, is generated by Q_3 and Q_4. An external bias voltage, V_m, controls Q_3, thus also controlling how much V_b is below V_l. Hence, we can control the conductance of Q_1 via V_m. We give a brief description of the circuit operation here; details are described in [20]. The receptor voltage, V_r, is clamped to the voltage needed to sink the current sourced by Q_6, which is biased by an external bias, V_u. Transistors, Q_2 and Q_6, form a high-gain, inverting amplifier. The value of V_{pl} sits at the voltage required for Q_5 to supply the photocurrent. The feedback transistor, Q_5, is operated in subthreshold so that V_r is logarithmic

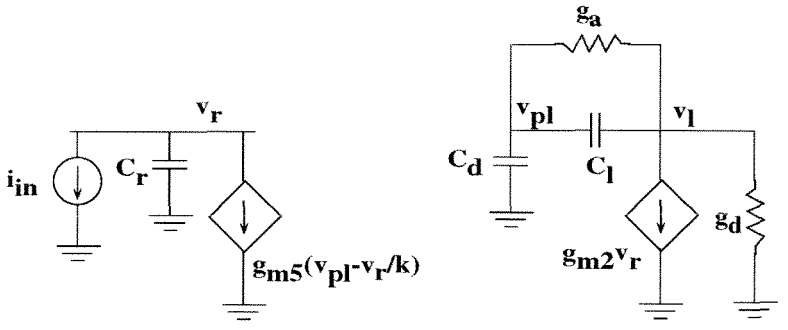

Figure 3.5: Small signal model of the circuit shown in Figure 3.4. C_r is the parasitic capacitance at the node, V_r.

in the photocurrent. When the photocurrent increases, the change in V_r leads to a large change at the output, V_l. This change in V_l is capacitively coupled through the capacitive divider, consisting of C_l and C_d, into V_{pl}, so that Q_5 supplies the extra increase in photocurrent.

3.5 Variants of the Retino-Laminar Circuit

We describe three variants of this circuit: RL_1, RL_2, and RL_3. Because RL_2 is an improved version of RL_1, we discuss them together.

3.5.1 RL_1

The first variant, RL_1 is already shown in Figure 3.4. In this section, we solve for the transfer function of the circuit and describe the dependence of the conductance of Q_1 on the background intensity.

First Variant

We first solve for the transfer function of the circuit by writing the KCL equations at the nodes, v_r, v_{pl}, and v_l, in the small-signal model shown in Figure 3.5.

$$\dot{v_{pl}}C_d + C_l(\dot{v_{pl}} - \dot{v_l}) + g_a(v_{pl} - v_l) = 0, \tag{3.1}$$

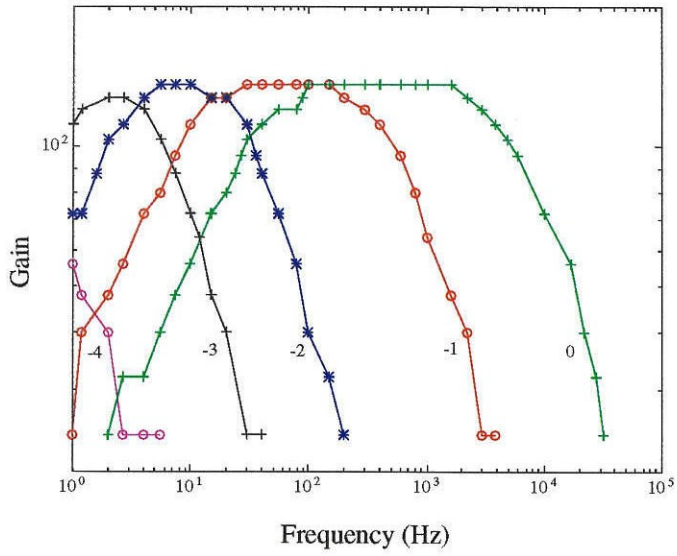

Figure 3.6: Frequency plot of the RL_1 circuit over five decades of background intensity. The number next to each curve corresponds to the log intensity of the mean value; 0 log corresponds to the intensity of a red LED. The plot shows that, in the range of 1 to 100 Hz, the circuit is a bandpass filter at high light intensities, and reduces to a lowpass filter at low light intensities.

$$g_{m2}v_r + v_l g_d + C_l(\dot{v}_l - \dot{v_{pl}}) + g_a(v_l - v_{pl}) = 0, \tag{3.2}$$

$$i_{in} + C_r\dot{v}_r = g_{m5}(v_{pl} - v_r/\kappa), \tag{3.3}$$

where g_d is the output conductance of Q_2 and Q_6, g_a is the output conductance of Q_1, g_m is the transconductance of a transistor, and C_r is the parasitic capacitance at the node, V_r. Taking the Laplace transform of Equation 3.1, we get

$$sv_{pl}C_d + sC_l(v_{pl} - v_l) + g_a(v_{pl} - v_l) = 0. \tag{3.4}$$

From Equation 3.4, we solve for v_l,

$$\begin{aligned} v_l &= \frac{v_{pl}}{sC_l + g_a}(s(C_d + C_l) + g_a) \\ &= \frac{v_{pl}}{s\tau_l + g_a/g_{m2}}(s(\tau_{ld} + \tau_l) + g_a/g_{m2}) \\ &= \frac{v_{pl}}{s\tau_l + X}K, \end{aligned} \tag{3.5}$$

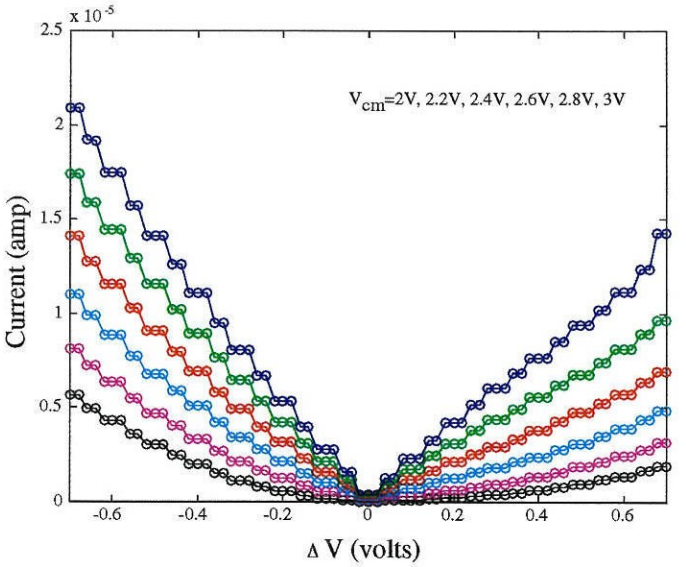

Figure 3.7: Measured I–V curve of Q_1. The curves were obtained by using different common-mode voltages. The six curves were taken with the common-mode voltage varying from 2 to 3V in steps of 0.2V. The curve with the highest slope corresponds to a common-mode voltage of 3V. The reason for the asymmetry in the curves is described in the text.

where $K = s(\tau_{ld} + \tau_l) + X$ and $X = \frac{g_a}{g_{m2}}$. The time constants, τ_l, τ_r, and τ_{ld}, are defined as follows:

$$\tau_l = \frac{C_l}{g_{m2}}; \tau_r = \frac{C_r}{g_{m5}}; \tau_{ld} = \frac{C_d}{g_{m2}}.$$

Taking the Laplace transform of Equation 3.2, we get

$$g_{m2}v_r + v_l g_d + sC_l(v_l - v_{pl}) + g_a(v_l - v_{pl}) = 0. \tag{3.6}$$

Solving for v_r from Equation 3.6 and substituting for $A_{amp} = \frac{g_{m2}}{g_d}$, we get

$$\begin{aligned} v_r &= -v_l(1/A_{amp} + s\tau_l + X) + (s\tau_l + X)v_{pl} \\ &= -\frac{v_{pl}}{s\tau_l + X}K(1/A_{amp} + s\tau_l + X) + (s\tau_l + X)v_{pl} \end{aligned}$$

$$= -\frac{v_{pl}}{s\tau_l + X}(K(1/A_{amp} + s\tau_l + X) - (s\tau_l + X)^2). \quad (3.7)$$

Taking the Laplace transform of Equation 3.3, we get

$$i_{in} + sC_r v_r = g_{m5}(v_{pl} - v_r/\kappa).$$

The following set of equations solve for $\frac{i_{in}}{g_{m5}}$:

$$i_{in} + v_r(sC_r + g_{m5}/\kappa) = g_{m5}v_{pl},$$

$$\frac{i_{in}}{g_{m5}} + v_r(s\tau_r + 1/\kappa) = v_{pl}.$$

We substitute v_{pl} from Equation 3.7 in the preceding equation:

$$\frac{i_{in}}{g_{m5}} + v_r M = -\frac{(s\tau_l + X)v_r}{K(1/A_{amp} + s\tau_l + X) - (s\tau_l + X)^2},$$

where $M = s\tau_r + 1/\kappa$. Hence, $\frac{i_{in}}{g_{m5}}$ is described by

$$\frac{i_{in}}{g_{m5}} = -(M + \frac{(s\tau_l + X)}{K(1/A_{amp} + s\tau_l + X) - (s\tau_l + X)^2})v_r. \quad (3.8)$$

The transfer functions—$\frac{v_r}{i_{in}}$, $\frac{v_l}{i_{in}}$, and $\frac{v_{pl}}{i_{in}}$— are given by

$$\frac{v_r}{i_{in}} = -\frac{1}{g_{m5}}\frac{K(1/A_{amp} + s\tau_l + X) - (s\tau_l + X)^2}{M(K(1/A_{amp} + s\tau_l + X) - (s\tau_l + X)^2) + s\tau_l + X}, \quad (3.9)$$

$$\frac{v_l}{i_{in}} = \frac{K}{g_{m5}}\frac{1}{M(K(1/A_{amp} + s\tau_l + X) - (s\tau_l + X)^2) + s\tau_l + X}, \quad (3.10)$$

$$\frac{v_{pl}}{i_{in}} = \frac{(s\tau_l + X)}{g_{m5}}\frac{1}{M(K(1/A_{amp} + s\tau_l + X) - (s\tau_l + X)^2) + s\tau_l + X}. \quad (3.11)$$

We can reduce the denominators of Equations 3.9 to 3.11 to a second-order expression:

$$K(1/A_{amp} + s\tau_l + X) - (s\tau_l + X)^2 = (s\tau_l + X)(1/A_{amp} + s\tau_{ld}) + 1/A_{amp}(s\tau_{ld})$$

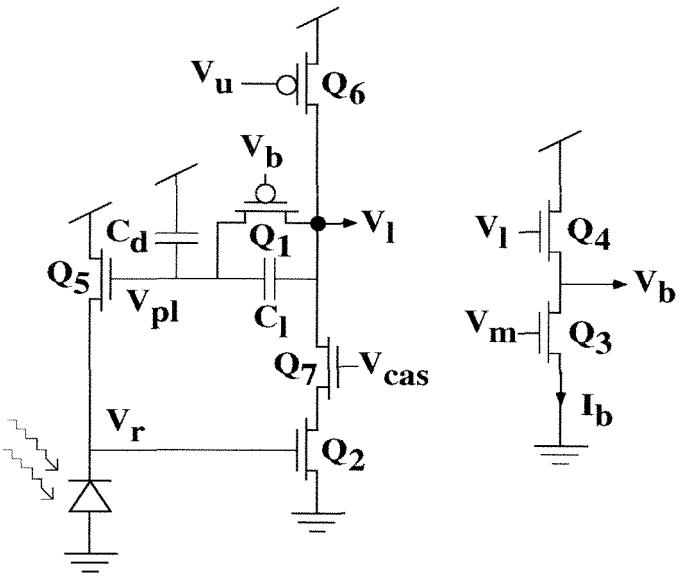

Figure 3.8: Circuit diagram of the variant, RL_2. The circuit is the same as that in Figure 3.4, except that we added a cascode transistor, Q_7, to decrease the Miller capacitance at the node, V_r.

$$= (s\tau_l + X)\left(1/A_{amp} + s\tau_{ld}) + \frac{s\tau_{ld}}{A_{amp}(s\tau_l + X)}\right).$$

Equations 3.8 through 3.11 then can be expressed as

$$\begin{aligned}
\frac{i_{in}}{g_{m5}} &= -\left(M + \frac{1}{1/A_{amp} + s\tau_{ld} + \frac{s\tau_{ld}}{A_{amp}(s\tau_l+X)}}\right) v_r, \\
\frac{v_r}{i_{in}} &= -\frac{1}{g_{m5}}\left[\frac{1/A_{amp} + s\tau_{ld} + \frac{s\tau_{ld}}{A_{amp}(s\tau_l+X)}}{(s\tau_r + 1/\kappa)(1/A_{amp} + s\tau_{ld} + \frac{s\tau_{ld}}{A_{amp}(s\tau_l+X)}) + 1}\right], \\
\frac{v_{pl}}{i_{in}} &= \frac{1}{g_{m5}}\left[\frac{1}{(s\tau_r + 1/\kappa)(1/A_{amp} + s\tau_{ld} + \frac{s\tau_{ld}}{A_{amp}(s\tau_l+X)}) + 1}\right], \\
\frac{v_l}{i_{in}} &= \frac{1}{g_{m5}}\left[\frac{\frac{s(\tau_{ld}+\tau_l)+X}{s\tau_l+X}}{(s\tau_r + 1/\kappa)(1/A_{amp} + s\tau_{ld} + \frac{s\tau_{ld}}{A_{amp}(s\tau_l+X)}) + 1}\right] \\
&= \frac{1}{g_{m5}}\left[\frac{\frac{s(\tau_{ld}+\tau_l)+g_a/g_{m2}}{s\tau_l+g_a/g_{m2}}}{(s\tau_r + 1/\kappa)(1/A_{amp} + s\tau_{ld} + \frac{s\tau_{ld}}{A_{amp}(s\tau_l+g_a/g_{m2})}) + 1}\right]. \qquad (3.12)
\end{aligned}$$

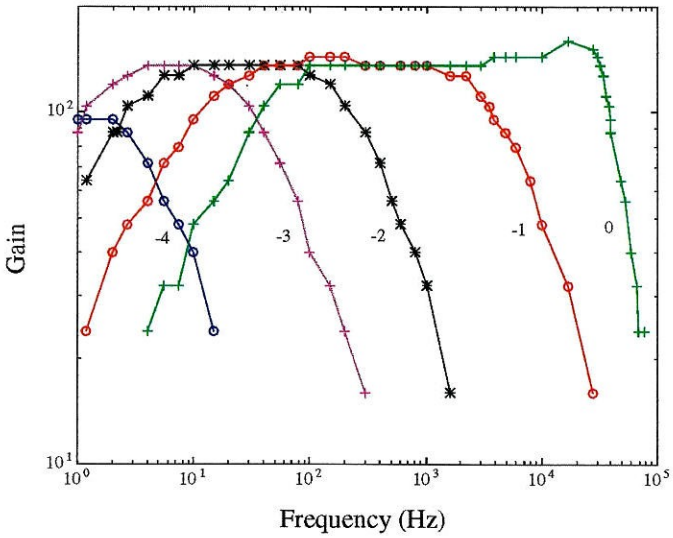

Figure 3.9: Frequency plot of the variant, RL_2, over five decades of background intensity. The bandwidths of the frequency curves are extended through the addition of a cascode transistor, as shown in Figure 3.8.

The low-frequency gain of the circuit from Equation 3.12 is then

$$\frac{v_l/\mathrm{U_T}}{i_{in}/I_{\mathrm{ph}}} = \frac{1}{\kappa}\frac{A_{amp}}{1+\kappa A_{amp}},$$

and the circuit has a zero at

$$\begin{aligned} z_0 &= -\frac{g_a}{g_{m2}}\frac{1}{\tau_{ld}+\tau_l} \\ &= -\frac{g_a}{C_d+C_l}. \end{aligned}$$

The frequency response curves in Figure 3.6 are measured from the fabricated circuit over five decades of background intensity. We obtain the curves by using a sine-wave modulated red LED source. The number next to each curve is the log intensity of the mean value; 0 log is the intensity of the LED source. We obtain the remaining curves by interposing neutral density filters between the LED and the chip. Figure 3.6 shows that, in the range of 1 to 100 Hz, the circuit is a bandpass

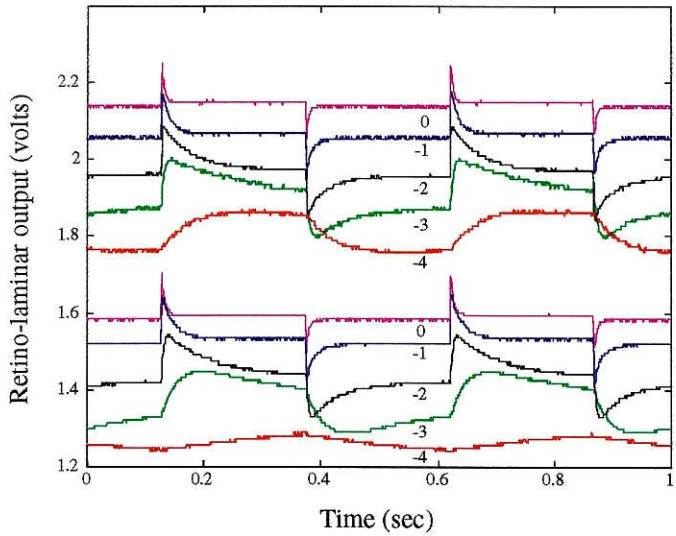

Figure 3.10: Temporal responses of the variants, RL_1 and RL_2 over five decades of background intensity. The top set of curves corresponds to the responses from RL_2 and have been shifted up by 0.5V for ease of comparison. The input stimulus is a red LED of contrast 0.15. The circuit acts as a highpass filter (that is, a differentiator) at high intensities, and as a lowpass filter as the intensity drops.

filter at high light levels, and reduces to a lowpass filter at low light levels. For each frequency curve, the gain is flat in the middle, and is given by $A_{cl} = \frac{C_1+C_d}{C_1}$. The cutoff frequencies change with the background intensity; this change is analyzed next.

I–V Relationship

Here, we analyze the dependence of the cutoff frequencies of the circuit on the background intensity. The equation for the current through Q_1 can be written as

$$\begin{aligned} I &= I_{op}e^{-\kappa_p V_b}(e^{(\overline{V}+\Delta V/2)} - e^{(\overline{V}-\Delta V/2)}) \\ &= I_{op}e^{-\kappa_p V_b}e^{\overline{V}}(e^{\Delta V/2} - e^{-\Delta V/2}) \\ &= 2I_{op}e^{-\kappa_p V_b}e^{\overline{V}}\sinh(\Delta V/2)), \end{aligned} \tag{3.13}$$

where $\overline{V} = \frac{V_1+V_{pl}}{2}$ and $\Delta V = V_1 - V_{pl}$. The exponential relationship for Equation 3.13 is for a pFET transistor operating in subthreshold, where I_{op} is the quiescent

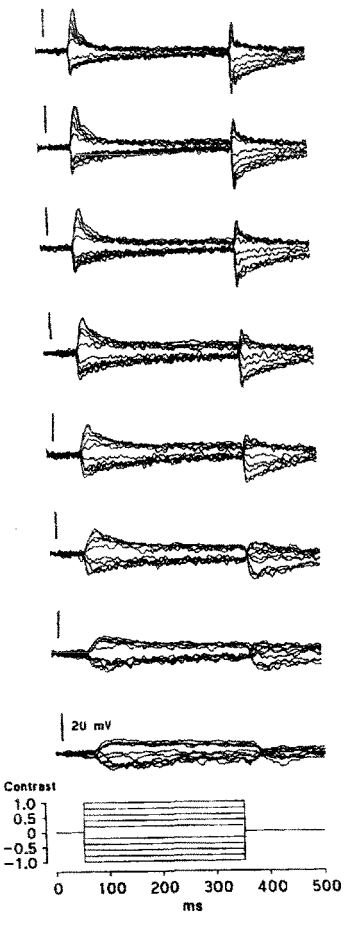

Figure 3.11: Contrast responses of LMC over eight different background intensities at 0.5 log intensity units apart. Responses are to 300ms contrast steps. Source: From Juusola and colleagues [8], Figure 4, pg. 125.

leakage current of the transistor, and κ_p is the effectiveness of the gate in controlling the surface potential of the channel of the pFET.

The KCL equation for the bias circuit consisting of Q_3 and Q_4 is given by

$$I_b = I_{on} e^{\kappa_n(\overline{V}+\Delta V/2)} e^{-V_b}, \tag{3.14}$$

where $V_1 = \overline{V}+\Delta V/2$, I_{on} is the quiescent leakage current of the nFET transistor, and κ_n is the effectiveness of the gate in controlling the surface potential of the channel

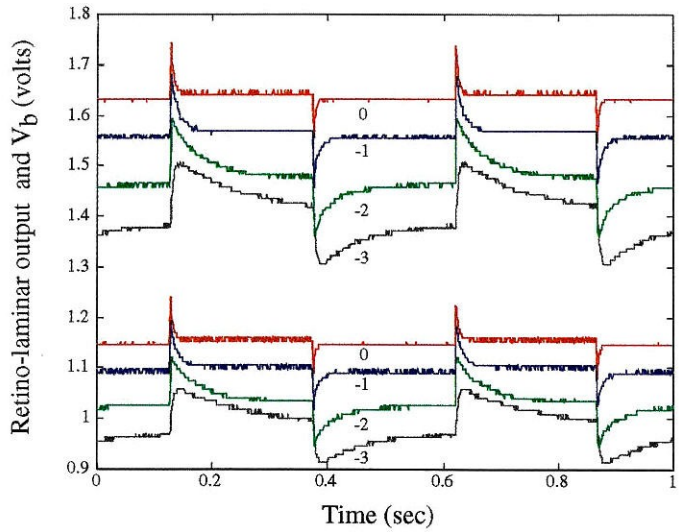

Figure 3.12: Response of V_1, and V_b of RL_2 to a step response over four decades of intensities. The bias curves have been shifted by 0.6V. The input stimulus is a square-wave modulated LED source with a contrast of 0.15. The larger difference between V_1 and V_b at high intensities is due to the body effect of Q_4.

of the nFET. We rearrange the terms in Equation 3.14 to solve for $e^{-\kappa_p V_b}$:

$$e^{-\kappa_p V_b} = (\frac{I_b}{I_{on}})^{\kappa_p} e^{-\kappa_n \kappa_p (\overline{V} + \Delta V/2)}. \tag{3.15}$$

Substituting Equation 3.15 into Equation 3.13, we get the I–V relationship for Q_1:

$$I = 2I_{op}(\frac{I_b}{I_{on}})^{\kappa_p} e^{(1-\kappa_n\kappa_p)\overline{V}} e^{-\kappa_n\kappa_p \Delta V/2} \sinh(\Delta V/2). \tag{3.16}$$

Measured I–V curves of Q_1 with six different common-mode voltages are shown in Figure 3.7. The common-mode voltage varies from 2V to 3V in steps of 0.2V. The curve with the highest slope (i.e., transconductance) is taken with a common-mode voltage of 3V. The curve is asymmetrical because Q_1 acts like a resistor when V_1 is higher than V_{pl}, and acts like a diode when V_1 is less than V_{pl}. Interestingly, an increase in the voltage, V_1, leads to a decrease in κ_p of Q_1 and to an increase in κ_n of Q_4. Hence, the change in the κ effects tend to cancel out each other. We know that

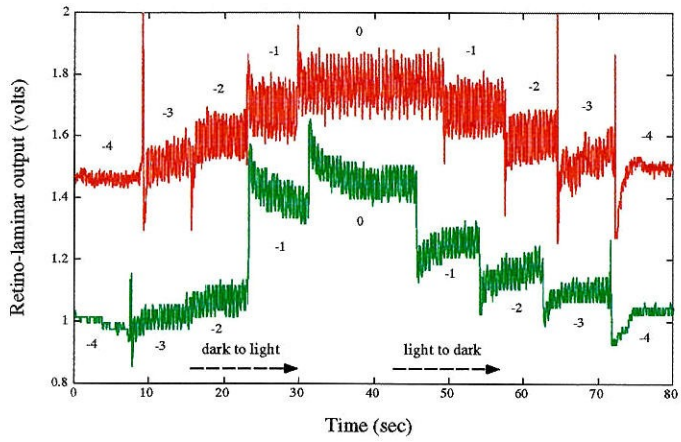

Figure 3.13: Plots of adaptation responses of RL_2 and of Delbrück's circuit. The input stimulus is a red LED driven by a square wave of contrast 0.18. The bottom curve corresponding to Delbrück's receptor has been shifted down so that we can compare the two curves. The adaptation response of the RL_2 circuit is more symmetrical than that of Delbrück's circuit when the circuit goes from dark to light conditions and back.

$V_{\rm pl}$ biases Q_5, which supplies the photocurrent, $I_{\rm ph}$. Since $I_{\rm ph} = I_{on}e^{\kappa_n V_{\rm pl} - V_{\rm r}}$,

$$(\frac{I_{\rm ph}e^{V_{\rm r}}}{I_{on}})^{1/\kappa_n} = e^{V_{\rm pl}}. \tag{3.17}$$

Substituting Equation 3.17 into Equation 3.16, and substituting for $\overline{V} = \frac{V_{\rm l}+V_{\rm pl}}{2} = V_{\rm pl} + \Delta V/2$, we get

$$\begin{aligned} I &= 2I_{op}(\frac{I_b}{I_{on}})^{\kappa_p} e^{(1-\kappa_n\kappa_p)V_{\rm pl}} e^{(1-2\kappa_n\kappa_p)\Delta V/2} \sinh(\Delta V/2) \\ &= I_\alpha I_{\rm ph}^{(1-\kappa_n\kappa_p)/\kappa_n} e^{(1-2\kappa_n\kappa_p)\Delta V/2} \sinh(\Delta V/2), \end{aligned} \tag{3.18}$$

where $I_\alpha = 2I_{op}(\frac{I_b}{I_{on}})^{\kappa_p}(\frac{eV_{\rm r}}{I_{on}})^{(1-\kappa_n\kappa_p)/\kappa_n}$. Equation 3.18 shows that conductance, g_a, of Q_1 in Figure 3.5, is proportional to the background intensity, $I_{\rm ph}$. As $I_{\rm ph}$ increases, g_a increases, so the cutoff frequencies shift to the right, as seen in Figure 3.6. If we compare both the "0" curve and the "-1" curve, we can see that the cutoff frequencies are approximately different by a factor of 10. Thus, the exponent of $I_{\rm ph}$, $(1-\kappa_n\kappa_p)/\kappa_n \approx 1$. Since the κ values change with the current through the transistor,

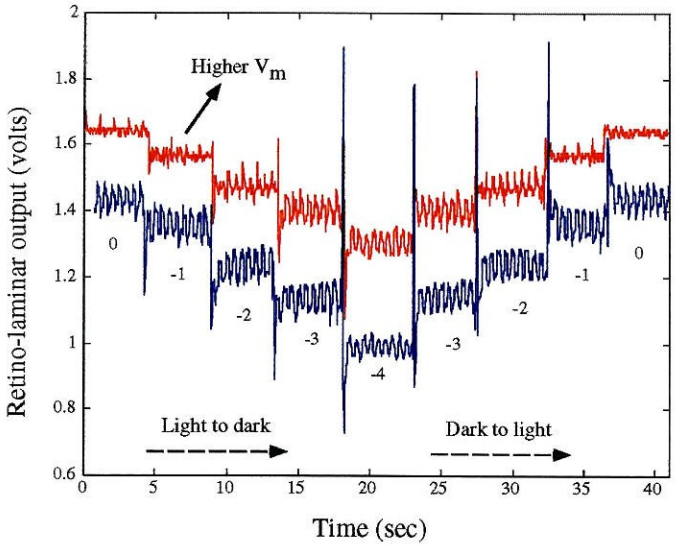

Figure 3.14: Adaptation responses of the RL_2 circuit for two values of V_m. The curves show how the adaptation time constant of the circuit changes with V_m(or I_b), when the circuit goes from dark to light conditions and back. The bottom curve corresponds to a smaller value of V_m, the bottom curve is shifted down by 0.2V for ease of comparison.

the exponent also changes. The different values of the exponent with I_{ph} can be seen from the different amounts of shifts in the cutoff frequencies of the curves.

3.5.2 RL_2

The next variant of the retino-laminar circuit, RL_2, improves RL_1, by adding a cascode transistor, Q_7, as shown in Figure 3.8. The addition of the cascode transistor increases the bandwidth of the circuit by about a decade. In this section, we describe the temporal responses of RL_2, and compare the adaptation response of RL_2 with that of Delbrück's circuit.

Temporal responses

The cascode transistor reduces the Miller capacitance observed by the node, V_r, and thus, increases the bandwidth of the circuit under all background intensities. The increase in the bandwidth of the circuit is shown in Figure 3.9, where we obtain the

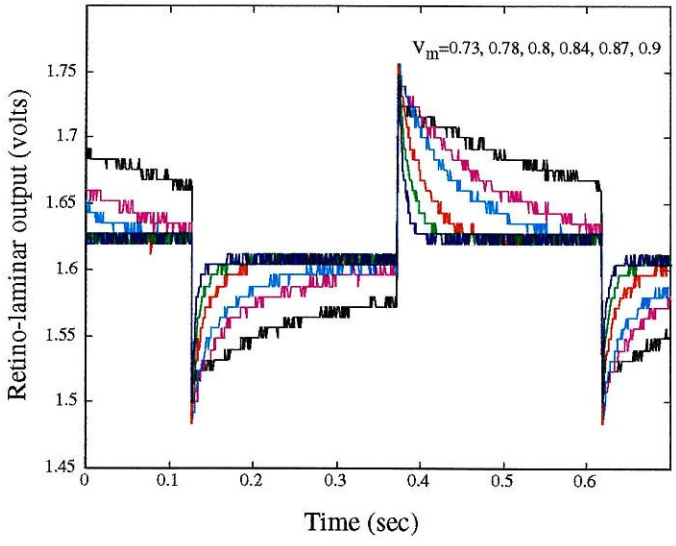

Figure 3.15: Response of V_l of RL_2 to a step response for different values of V_m. The input stimulus is a square-wave modulated red LED source. The value of V_m was varied from 0.73 to 0.9 V. The curve with the longest time constant of decay corresponds to the lowest value of V_m.

curves using the same LED source as that described for Figure 3.6. The temporal responses of the circuit under five different light levels for both RL_1 and RL_2 are shown in Figure 3.10.

The input stimulus to the circuit is a square-wave modulated LED with a contrast of 0.15. The data in Figure 3.10 show the change in filtering behavior of both circuits with different background intensities. The temporal responses observed in these circuits are comparable to the contrast responses recorded from the LMCs as shown in Figure 3.11 [8]. The LMC response to a 300ms contrast step in Figure 3.11 was taken at eight different background intensities at 0.5 log intensity units apart.

The change in the time constant of the circuit is due to the change in the conductance, g_a, as the background intensity changes. The conductance, g_a, is greater at high background intensities because of the increased body effect at Q_4 due to a higher source voltage. The larger difference between V_l and V_b at high intensities can be seen in Figure 3.12. Here, the step response of V_l and V_b is measured over four decades of intensities.

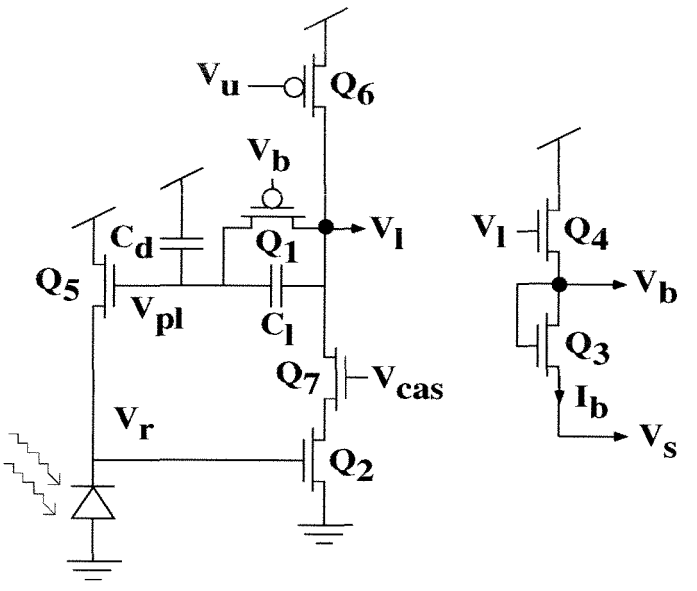

Figure 3.16: Circuit diagram of the variant, RL_3. This circuit is the same as the RL_2 circuit, except that Q_3 is diode connected.

Adaptation Properties

We can look at the RL circuit as a version of the Delbrück circuit with an adaptation time constant that is set by an external bias. In the Delbrück circuit, the adaptation time constant is predetermined at the design phase and by process parameters. In Figure 3.13, we compare the adaptation properties of RL_2 with those of Delbrück's circuit. The input stimulus consists of a square-wave modulated LED source with a contrast of about 0.18. We take the circuit from dark to light conditions, and back again, by using neutral density filters. The top curve corresponds to the response from RL_2, and the bottom curve corresponds to the response from the Delbrück circuit. The RL_2 circuit adapts symmetrically, when it goes from light to dark conditions and back. In contrast, Delbrück's circuit shows an asymmetrical adaptative behavior; it adapts more slowly when it goes from dark to light conditions. The curve also shows that the adaptation time constant of Delbrück's circuit, unexpectedly, depends on the background intensity. The time constant of the adaptive element probably changes because the minority carriers generated in the photodiode area migrate to the well in

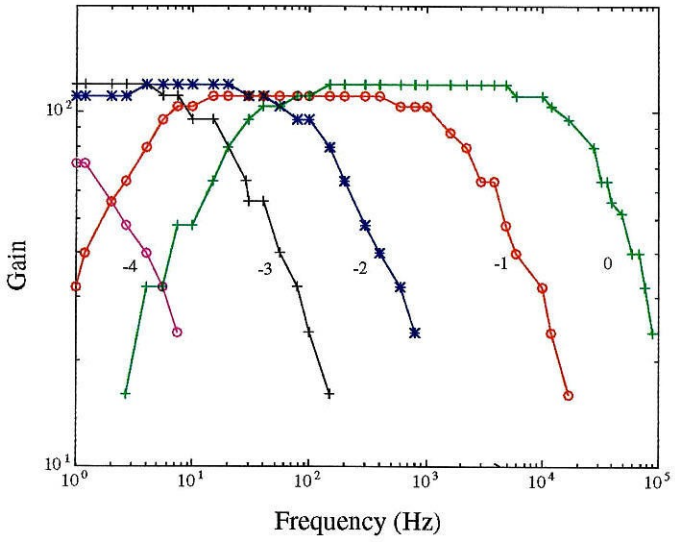

Figure 3.17: Frequency plot of the RL_3 circuit over five decades of background intensity. The curves show that, in the range of 1 to 100 Hz, the circuit acts as a highpass filter for high light levels and as a lowpass filter under low light levels.

which the adaptive element sits, and change the conductance of this element.

As described earlier, the adaptation time constant of the RL_2 circuit can be controlled via the bias voltage, V_m. Figure 3.14 shows the adaptation properties of the circuit for two different values of V_m. The top curve in the figure corresponds to a larger value of V_m, and hence to an increased conductance, g_a, or to a decreased time constant. We can see that the adaptation time constant is smaller for the top curve than for the bottom curve. Figure 3.14 also shows that the adaptation time constant is less affected by changes in V_m, when the circuit goes from light to dark than when it goes from dark to light conditions. This asymmetry comes about because Q_4 acts as a source follower only when V_1 goes high. When V_1 goes low, Q_3 discharges V_b at a linear rate.

The dependence of the time constant of the circuit on V_m is further demonstrated by recording the step response of the circuit to an LED source of contrast 0.15 for various values of V_m. The output data are shown in Figure 3.15 for 5 different values of V_m.

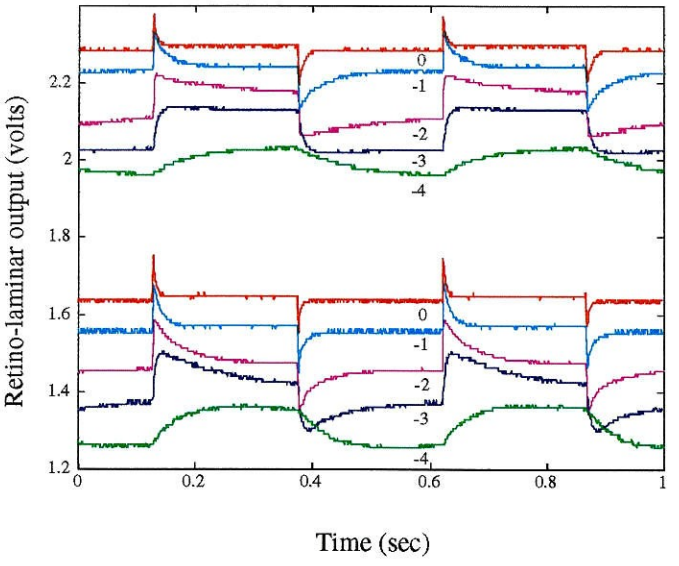

Figure 3.18: Step responses of the RL_2 and RL_3 circuits. The curves show the responses of both variants of the circuit over five decades of background intensity to an LED source of contrast 0.18. The top set of curves shows the responses from RL_3, while the bottom set of curves shows to the responses from RL_2. The biases, V_m and V_s, have been adjusted such that the time constants of both circuits at the highest intensity are about equal.

3.5.3 RL_3

Figure 3.16 shows the third version of the retino-laminar circuit, RL_3. The difference between this circuit and RL_2 is that Q_3 is diode connected and the source of the transistor is brought out externally via V_s. This version was suggested by Rahul Sarpeshkar [23]. Even though the cascode transistor has been included in the figure, the results shown here are from a variant without the cascode transistor. The transfer function of this circuit is similar to that of RL_1, except that the conductance, g_a, has a different dependence on the photocurrent, I_{ph}. The dependence of the time constant of RL_3 on the background intensity is smaller than that of RL_1.

I–V Relationship

We do an analysis similar to that in Section 3.5.1, to determine the dependence of g_a on the photocurrent, I_{ph}. We first solve for the I–V relationship of Q_1. The

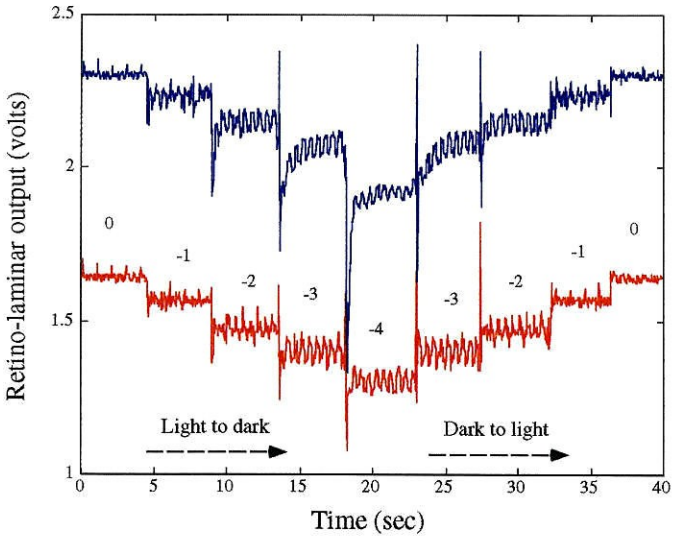

Figure 3.19: Plots of adaptation responses of RL_2 and RL_3 under five decades of background intensity. The input stimulus is a red LED driven by a square wave of contrast 0.18. The top curve corresponds to the response from RL_3. The bottom curve corresponds to the response from RL_2.

equation for the bias circuit is

$$\begin{aligned} I_b &= I_{on} e^{\kappa_n(\overline{V}+\Delta V/2)} e^{-V_b} \\ &= I_{on} e^{\kappa_n V_b - V_s}, \end{aligned} \tag{3.19}$$

where $V_1 = \overline{V} + \Delta V/2$. We rearrange the terms in Equation 3.19 to solve for $e^{-\kappa_p V_b}$:

$$e^{-\kappa_p V_b} = e^{-\frac{\kappa_n \kappa_p}{\kappa_n+1}(\overline{V}+\Delta V/2)} e^{-\frac{\kappa_p}{\kappa_n+1} V_s}. \tag{3.20}$$

Substituting Equation 3.20 into Equation 3.13 (Section 3.5.1), and substituting for $\overline{V} = \frac{V_1+V_{pl}}{2} = V_{pl} + \Delta V/2$, we get

$$\begin{aligned} I &= 2I_{op} e^{(1-\frac{\kappa_n\kappa_p}{\kappa_n+1})\overline{V}} e^{-\frac{\kappa_n\kappa_p}{\kappa_n+1}\Delta V/2} \sinh(\Delta V/2) e^{-\frac{\kappa_p}{\kappa_n+1} V_s} \\ &= 2I_{op} e^{(1-\frac{\kappa_n\kappa_p}{\kappa_n+1})V_{pl}} e^{1-2\frac{\kappa_n\kappa_p}{\kappa_n+1}\Delta V/2} \sinh(\Delta V/2) e^{-\frac{\kappa_p}{\kappa_n+1} V_s}. \end{aligned} \tag{3.21}$$

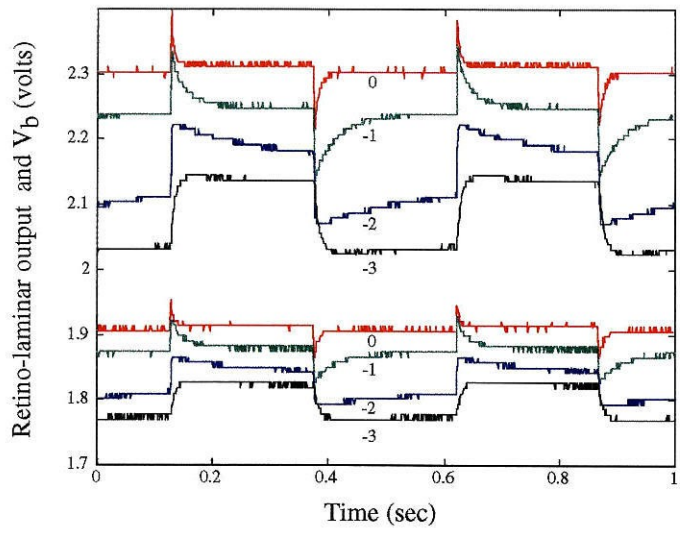

Figure 3.20: Response of V_l, and V_b of RL_3 to a step response over four decades of intensities. The bias curves have been shifted by 0.6V. The input stimulus is a square-wave modulated red LED source of contrast 0.15. The larger difference between V_l and V_b at high intensities is due to the body effect of Q_4.

We now substitute in I_{ph} from Equation 3.17 into Equation 3.21:

$$I = I_\beta I_{ph}^{(1-\frac{\kappa_n\kappa_p}{\kappa_n+1})/\kappa_n} e^{(1-2\frac{\kappa_n\kappa_p}{\kappa_n+1})\Delta V/2} \sinh(\Delta V/2),$$

where $I_\beta = 2I_{op}(\frac{eV_r}{I_{on}})^{(1-\frac{\kappa_n\kappa_p}{\kappa_n+1})/\kappa_n}$.

The frequency-response curves for this circuit are shown in Figure 3.17. The data show that, in the frequency range of 1 to 100 Hz, the circuit acts as a highpass filter under high intensities, and reduces to a lowpass filter as the intensity drops. The corresponding temporal responses are shown in Figure 3.18. Here, the figure shows the step responses of RL_2 and RL_3 to an LED source of contrast 0.18 over five decades of background intensity. The top set of curves shows the responses from RL_3; the bottom set of curves shows the responses from RL_2. The biases, V_s and V_m, have been set such that the time constant for both circuits is approximately equal at the largest background intensity. If we compare the dependence of the time constant of RL_3 on the background intensity, and that of RL_1 in Figure 3.10, we see that the time constant of RL_3 varies less with intensity. With a diode-connected Q_3, the change in

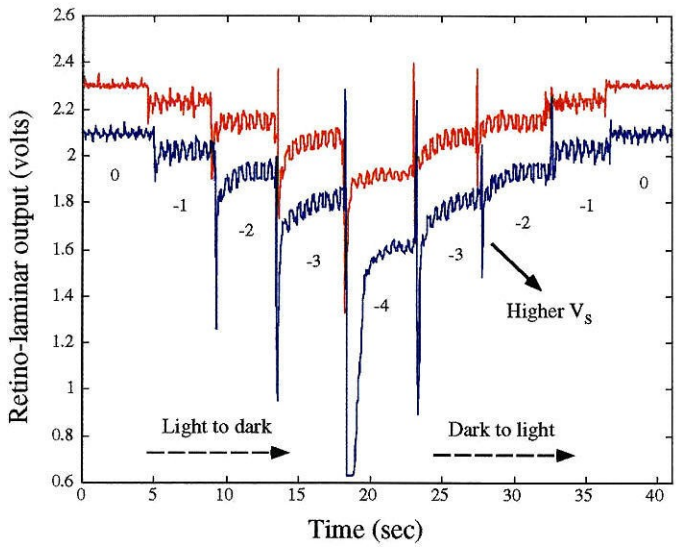

Figure 3.21: Adaptation responses of RL_3 for two different values of V_s. The bottom curve corresponds to a higher value of V_s. The curve has been shifted down by 0.2V for ease of comparison. A higher value of V_s corresponds to a decrease in conductance of Q_1, or to an increase in the adaptation time constant

V_b in RL_3 is $1/(1+\kappa_n)$ less than the change in V_b in RL_1, for a given change in V_l. This difference in dependence can be seen from the prefactor of the $\overline{V} + \Delta V/2$ term in Equations 3.15 and 3.20.

As we have seen in the case of the RL_2 circuit, the change in the temporal filtering over different intensities is due to the body effect of Q_4. Figure 3.20 shows the larger difference in V_l and V_b (i.e., g_a is larger) at high intensities. The data in this figure are the step responses of V_l and V_b over four decades of intensities to an LED source of contrast 0.15.

Adaptation Properties

A comparison of the adaptation behaviors of RL_2 and RL_3 is shown in Figure 3.19. The top curve shows the adaptive behavior of RL_3; the bottom curve shows the response from RL_2. The adaptation response is symmetrical for both RL_1 and RL_2, when the circuit goes from dark to light conditions and back. There is a difference in the initial response when the RL_3 circuit goes from "-4" to "-3" conditions: The positive-going response is followed by a sharp negative-going response. The RL_2

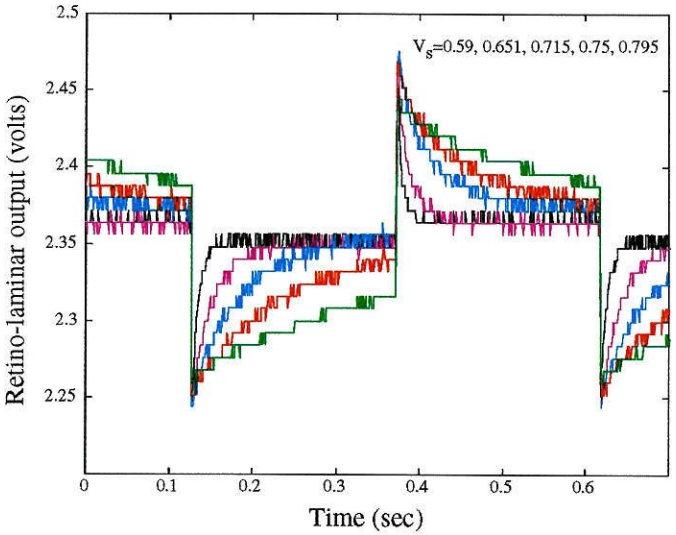

Figure 3.22: Response of V_l of RL_3 to a step response for different values of V_s. The input stimulus is a square-wave modulated red LED source. The value of V_s was varied from 0.59 to 0.795V. The curve with the longest time constant corresponds to the value of $V_s = 0.795$.

circuit does not show this response under similar conditions. The adaptation time constant of the RL_3 circuit can also be controlled externally via V_s. In Figure 3.21, the adaptation behavior of RL_3 is shown for two different values of V_s. The bottom curve shows the response of the circuit with a higher value of V_s. A higher value of V_s corresponds to a decrease in the conductance, g_a, or an increase in the adaptation time constant. As in the case of RL_2, we can demonstrate the dependence of the time constant of the circuit on V_s by recording the step response of the circuit to an LED source for various values of V_s. The output data are shown in Figure 3.22 for 5 different values of V_s.

3.6 Layout

A hexagonal array of 20 × 20 pixels of the variant, RL_1, has been fabricated in the $1.2\mu m$ CMOS ORBIT technology. Figure 3.24 shows the layout of this array and Figure 3.23 shows the layout of a single pixel. The green areas in both figures

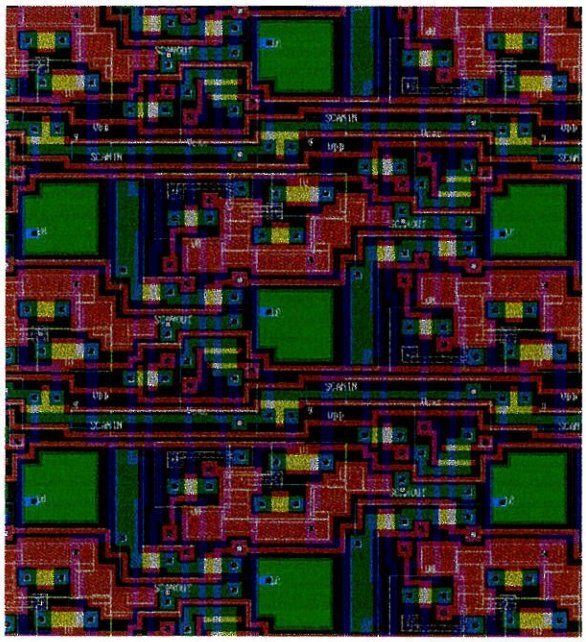

Figure 3.23: Layout of the variant, RL_1.

correspond to the photosensor area. The second layer of metal in the layout covers the entire chip, except over the photosensor regions. This metal layer prevents photons from entering the circuits.

3.7 Discussion

This chapter described a compact silicon model of the adaptive filtering properties of the laminar cells. The circuit does not model the zero DC gain of the LMC. Moini and colleagues [24] modeled the LMC by a differentiator circuit which gives zero DC gain. However, the adaptive filtering properties of the LMC are not modeled by this circuit.

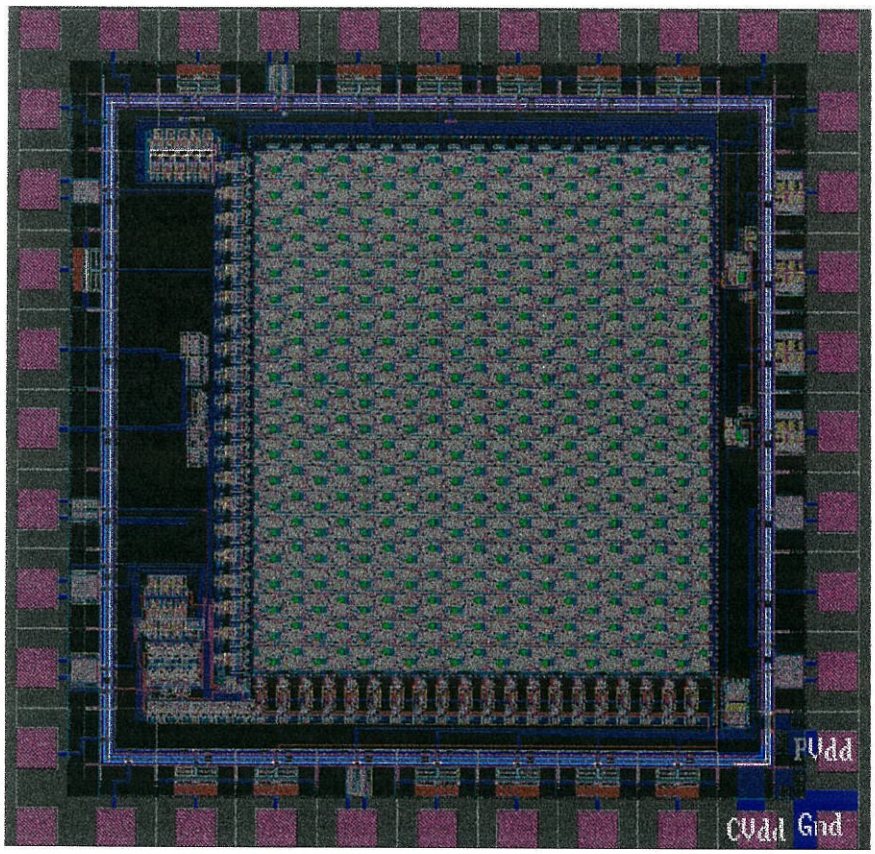

Figure 3.24: 2D layout of an array of 20×20 pixels of the variant, RL_1, in $1.2\mu m$ ORBIT technology.

Bibliography

[1] H. J. Strausfeld and J. A. Campos-Ortega, "Vision in insects: pathways possibly underlying neural adaptation and lateral inhibition," *Science*, **195**, pp. 894–897, 1977.

[2] O. Trujillo-Cenoz, "Some aspects of the structural organisation of the intermediate retina of dipterans," *J. Ultrastr. Res*, **13**, pp. 1–33, 1965.

[3] I. A. Meinertzhagen and S. D. O'Neil, "Synaptic organization of columnar elements in the lamina of the wild type in *Drosophila melanogaster*," *Journal of Comparative Neurology*, **305:2**, pp. 232–263, 1991.

[4] S. Shaw, "Anatomy and physiology of identified non-spiking cells in the photoreceptor-lamina complex of the compound eye of insects, especially *Diptera*," in *Neurones without Impulses*, A. Roberts and B. Bush, Editors, pp. 61–116, Cambridge Univ. Press, Cambridge, 1981.

[5] V. Braitenberg, "Patterns of projection in the visual system of the fly. I. Retina-lamina projections," *Exp. Brain Research*, **3**, pp. 271–298, 1967.

[6] S. B. Laughlin, "Matching coding, circuits, cells, and molecules to signals - General principles of retinal design in the fly's eye," *Progress in Retinal and Eye Research*, **13:1**, pp. 165–196, 1994.

[7] S. B. Laughlin, and D. Osorio, "Mechanisms for neural signal enhancement in the blowfly compound eye," *J. Exp. Biol.*, **144**, pp. 113–146, 1989.

[8] M. Juusola, R. O. Uusitola, and M. Weckström, " Transfer of graded potentials at the photoreceptor-interneuron synapse," *J. of General Physiology*, **105**, pp. 115–148, 1995.

[9] N. M. Jansonius and J. H. van Hateren, "Fast temporal adaptation of on-off units in the first optic chiasm of the blowfly," *J. Comp. Physiology A*, **168**, pp. 631–637, 1991.

[10] A. Dubs, "The spatial integration of signals in the retina and lamina of the fly compound eye under different conditions of luminance," *J. Comp. Physiology A*, **146**, pp. 321–343, 1982.

[11] F. Zettler and M. Järvilehto, " Lateral inhibition in an insect eye," *Z. Vergl. Physiology*, **76**, pp. 233–244, 1972.

[12] M. Juusola, M. Weckström, R. O. Uusitola, M. J. Korenberg, and A. S. French, "Nonlinear models of the first synapse in the light-adapted fly retina," *J. of Neurophysiology*, **74:6**, pp. 2538–2547, 1995.

[13] S. B. Laughlin and R. C. Hardie, "Common strategies for light adaptation in the peripheral visual systems of fly and dragonfly," *J. Physiol. Lond.*, **128**, pp. 319–340, 1978.

[14] M. V. Srinivasan, S. B. Laughlin, and A. Dubs, "Predictive coding: a fresh view of inhibition in the retina," *Proc. R. Soc. Lond. Series B Biological Sciences*, **216:1205**, pp. 427–459, 1982.

[15] H. B. Barlow, "The coding of sensory messages," in *Current problems in animal behavior*, W. H. Thorpe and O. L. Zangwill, eds, pp. 331–360, Cambridge Univ. Press, Cambridge, 1961.

[16] M. V. Srinivasan, R. B. Pinter, and D. Osorio, "Matched filtering in the visual systems of the fly: large monopolar cells of the lamina are optimized to detect moving edges and blobs," *Proc. R. Soc. Lond. Series B Biological Sciences*, **240:1298**, pp. 279–293, 1990.

[17] J. H. van Hateren, "Theoretical predictions of spatiotemporal receptive fields of fly LMCS, and experimental validation," *J. Comp. Physiology A*, **171:2**, pp. 157–170, 1992.

[18] J. H. van Hateren, "A theory of maximizing sensory information," *Biological Cybernetics*, **68:1**, pp. 23–29, 1992.

[19] J. H. van Hateren, "Real and optimal images in early vision," *Nature*, **360**, pp. 68–70, 1992.

[20] T. Delbrück, "Analog VLSI phototransduction by continous-time, adaptive, logarithmic photoreceptor circuits," *CNS Memo No.30*, California Institute of Technology, Pasadena, CA, 1994.

[21] M. Banu and Y. Tsividis, "Floating voltage-controlled resistors in CMOS technology," *Electronics Letters*, **18:15**, pp. 678–679, 1982.

[22] M. Juusola, " Linear and non-linear contrast coding in light-adapted blowfly photoreceptors," *J. Comp. Physiology A*, **172**, pp. 511–521, 1993.

[23] R. Sarpeshkar, Private Communication, 1997.

[24] A. Moini, A. Bouzerdoum, K. Eshraghian, A. Yakovleff, X. T. Nguyen, A. Blanksby, R. Beare, D. Abbott, and R. E. Bogner, " An insect vision-based motion detection system," *IEEE Journal of Solid-State Circuits*, **32:2**, pp. 279–284, 1997.

Chapter 4 Motion Adaptation

In this chapter, I describe a new **adaptive correlator** that models the adaptation observed in the fly's motion system from recordings done on the H1 neuron. This adaptation process allows the motion system of the fly to match its temporal resolution to the speeds in the visual scene. This phenomenon of temporal resolution improvement with increasing presentations of moving stimuli is also observed in psychophysical experiments done on humans [1]. There is no evidence as yet that shows that the visual system of insects possesses cells that peak at different temporal frequencies in response to moving stimuli, similar to the cells in the motion processing area of cats and monkeys. This difference in the structure of the motion neural circuitry of vertebrates and invertebrates is probably due to the fact that the visual system of the fly consists of only about 0.5 million neurons, as compared to 10^{11} neurons in the human cortex. Faced with such scarcity of neurons, the insect must increase its time resolution by adapting the time constant of its motion system to the incoming motion signal. Recordings from the H1 neuron (one of the wide-field, direction-selective neurons in the lobula plate) show that the adaptation process allows the visual system to respond reliably to moving stimuli over 4 decades of temporal frequencies. The adaptation of the motion system to steady-state motion allows the system to respond to relative changes in motion, rather than constant motion. Similar adaptation phenomenon has been reported in photoreceptors and synapses (also called short-term synaptic depression) [2]. By adapting out the background lighting, the photoreceptor cell can respond to relative changes in intensity, or contrast over seven decades of background intensity. Similarly by adapting out the presynaptic firing rate, the post-synaptic cell can respond to relative changes in firing rate, rather than the absolute firing rate.

The output of the fly's motion system is typically modeled by the Hassenstein–Reichardt detector (or the correlation model). The adaptive correlator described here

is a variant of this model that includes adaptation of the time constant in the model. This adaptive model is implemented in an aVLSI circuit. Both simulation and chip results from this model are presented in this chapter. I compare the predictive results from my model with experimental adaptation results obtained from the H1 neuron by several research groups [3][4][5]. I also discuss the importance of the adaptation process in increasing the time resolution of the motion system.

4.1 Anatomy

The anatomy and physiology of the large-field tangential neurons in the lobula complex have been described extensively [6][7][8][9][10][11]. There are about 50 neurons in the lobula complex of *Calliphora*. Some of these neurons are shown in Figure 4.1. The immense dendritic arborizations of these neurons suggest that they integrate from a lot of presynaptic cells. The cells respond to motion in the preferred or null direction, either with graded responses, action potentials or both. The neurons respond to motion in only four directions; progressive, regressive, upwards and downwards. These neurons are involved in controlling the fly's flight course [12][13]. The output neurons either synapse onto neurons driving the neck and flight motor neurons, or onto neurons driving the leg motor neurons [14].

Research into the behavioral responses of the fly and the study of the physiology of the direction-selective cells have been actively pursued by researchers at the Max-Planck Institute in Tuebingen [6][12][13][15][16][17][18][19][20].

4.2 Adaptation in the Fly's Motion System

The H1 neuron is a wide-field, direction-selective cell in the lobula plate, which integrates information spatially from elementary motion detectors (EMDs) [21][22][23]. The neuron responds preferentially to movement from the back to the front on the ipsilateral eye. The H1 neuron is a spiking neuron and it responds to stepwise displacements by increasing its firing rate to a peak before the firing rate decays back

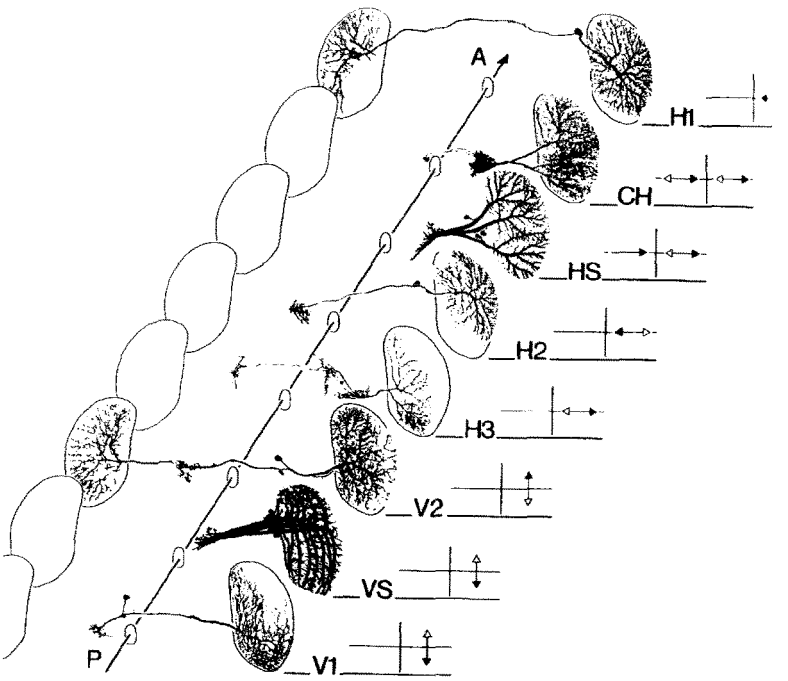

Figure 4.1: Tangential cells in the lobula plate of *Calliphora*. The figure shows the immense arborization of the dendrites of these cells. A: anterior, P: posterior. Source: From Hausen [7], Figure 3, pg. 55.

to a quiescent level. An example of the response of the neuron is shown in Figure 4.2. Using recordings on this neuron, several research groups [3][4][5][24] have shown that the time constant of the motion circuitry in flies adapts in response to moving stimuli.

In experiments performed by de Ruyter van Steveninck and associates [3], the H1 neuron in the blowfly *Calliphora erythrocephala* was first adapted to a moving square-wave grating for about 3.2s. The movement of the grating was stopped after a few seconds and a stepwise displacement in the grating was presented to the neuron after 0.2s. The firing rate of the neuron increases sharply before decaying exponentially to its resting level. They measured the time constant of the decay of the firing rate for different speeds of the adapting grating and observed that the time constant decreased in response to an increase in speed of the adapting grating. These results indicate that

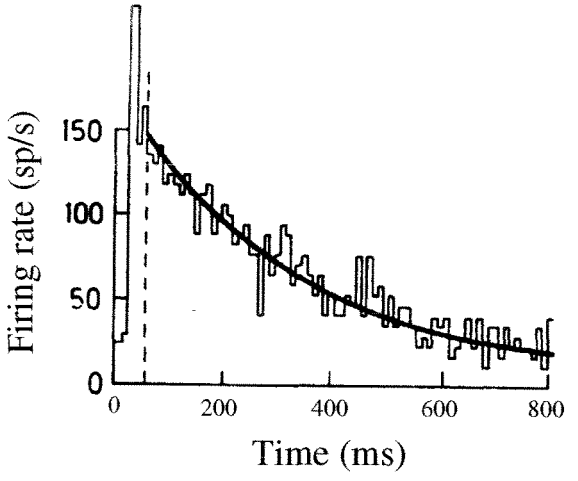

Figure 4.2: Example of the response of H1 to a stepwise displacement of a stimulus presented to the neuron in the preferred direction. Source: From de Ruyter van Steveninck and colleagues [3], Figure 1, pg. 224.

the time constant of the motion system adapts to the speed of the moving stimuli. The adaptation of the time constant is local, insensitive to contrast and the direction of motion, as shown in Figure 4.3 and Figure 4.4.

In a separate experiment, Maddess and Laughlin [4] also showed that the H1 neuron in the fly *Lucilia cuprina* adapts in response to motion, but their results indicate that the adaptation is dependent on contrast frequency, rather than on the speed of the moving stimulus. In their experiment, they adapted the neuron by moving a random grating for 6.7s after 16.7s of no motion. The H1 neuron responds to the start of the movement by increasing its firing rate to a peak before the firing rate adapts exponentially down to the background rate. The time constant of the decay of the firing rate in the presence of steady motion was measured for various speeds of the moving grating. Figure 4.5 shows the plot of the time constant of the adaptation versus the velocity of the grating. Maddess and Laughlin inferred that the H1 neuron responds to velocity contrast following Weber's law, much like photoreceptors respond to signal contrast rather than to background intensity. Laughlin [25] points out that the purposes of the adaptation process are to prevent the H1 neuron from saturating,

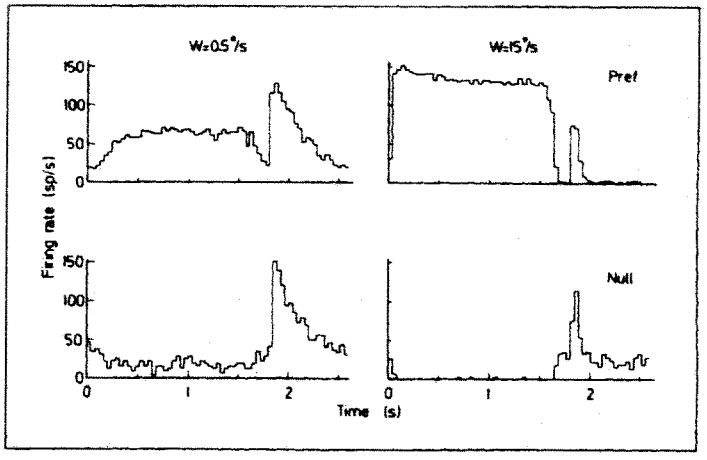

Figure 4.3: Experiments by de Ruyter van Steveninck and associates which show that adaptation occurs independent of direction of motion. The H1 neuron is first adapted to a constant speed (W) square-wave grating for several seconds. The grating was stopped for 200ms before a sudden step in the grating was presented to the fly. The figures in the first row show the response of the neuron to the grating moving in the preferred direction at two different adapting speeds, 0.5°/s and 15°/s. The time constant of the exponential decay of the neuron's response to a stepwise displacement of the grating is smaller in the case of the faster adapting speed, 15°/s. The figures in the bottom row show that the change in time constant occurs even if the adapting stimulus was moving in the null direction. Source: From de Ruyter van Steveninck and colleagues [3], Figure 4, pg. 226.

and to maintain high sensitivity to deviations in velocity from the mean level. This increase in sensitivity of H1 is seen in Maddess and Laughlin's work where they first adapted the H1 neuron to a moving stimulus at 58°/s for 6.7s after a stationary phase of 8.3s. During the 6.7s phase, 16 equally spaced increments and decrements of 23.4°/s were added to the velocity of the stimulus. The results are shown in Figure 4.6.

A distinction should be made here between the time constants defined in the work of de Ruyter van Steveninck and colleagues and that of Maddess and Laughlin. The first time constant describes the decay of the cell's response to a single test step and the range is from 300ms to 10ms as shown in Figure 4.4. The second time constant describes the speed with which the response to a maintained velocity decays. When

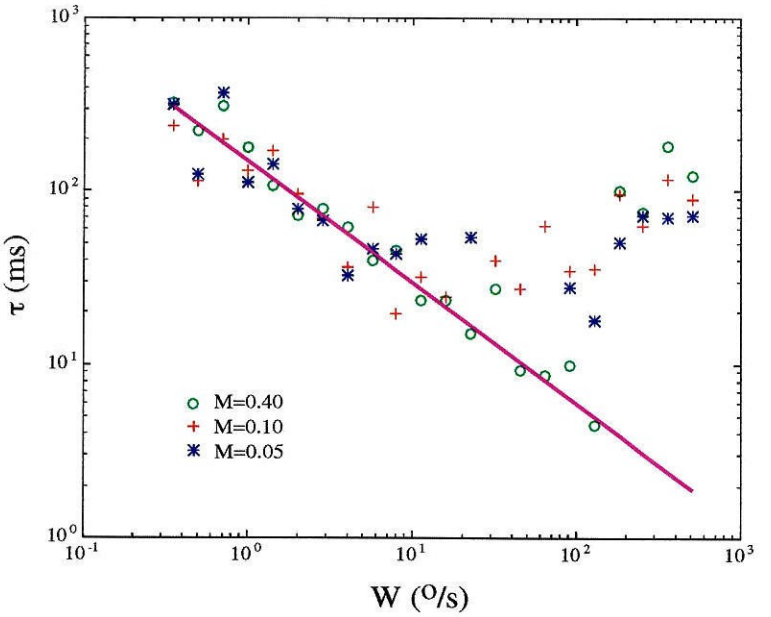

Figure 4.4: Plot of the adapted time constant versus the velocity of the adapting stimulus. The figure shows that the time constant of H1 adapts to the velocity, W, of the moving stimulus and that the time constant, τ, adapts independent of the contrast magnitude. The slope of the fit to the data is -0.7. A possible reason for the slope being less than -1 is described in Section 4.6. Source: From de Ruyter van Steveninck and colleagues [3], Figure 3, pg. 226.

the H1 neuron is stimulated by a pattern that starts moving at a maintained velocity, its initial high response decays to a plateau in a few seconds. Figure 4.5 shows that this time constant depends on the contrast frequency of the pattern. The decay in the firing rate in the second case is probably partly due to the fact that the time constant in Fig 4.4 is adapting to the new velocity. Thus, the second time constant could be reflecting the speed with which the first time constant adapts to the new conditions. In support of this view, in a direct measurement [3] on the neuron, the speed of adaptation of the first time constant was found to be of the order of seconds.

Jian and Horridge [26] confirmed Maddess and Laughlin's results that showed that the response of the H1 neuron to a constant velocity contrast is fairly independent of the adapting velocity. They also showed that the response of the H1 neuron increases with velocity contrast independently of background velocity, contrast frequency or

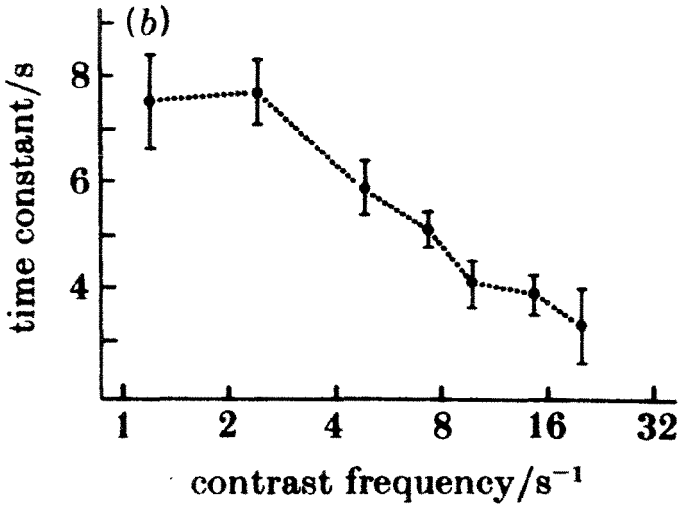

Figure 4.5: Adapted time constant versus contrast frequency. Source: From Maddess and Laughlin [4], Figure 9, pg. 263.

velocity modulation frequency. Similar results that show that the adaptation depends on contrast frequency rather than speed are borne out by the experiments of Borst and Egelhaaf on the H1 and HSE neurons in the blowfly [5].

From the results of the research groups above, we know that the adaptation process is spatially localized, is independent of contrast (for high-contrast stimuli), spatial wavelength, and of direction of motion. The adaptation also occurs on a long time scale of 6 to 7s.

4.3 Correlation Model

The responses of the H1 neuron can be modeled by the Hassenstein–Reichardt correlator, as shown in Figure 4.7. The Hassentein–Reichardt correlator was initially formulated to model the optomotor responses of the *Chlorophanus* beetle. Different variants of the Reichardt correlator [27] have also been used to model human motion detection. The blocks in the correlator have a fixed time constant, and hence do not model the change in time constant observed in the adaptation experiments described

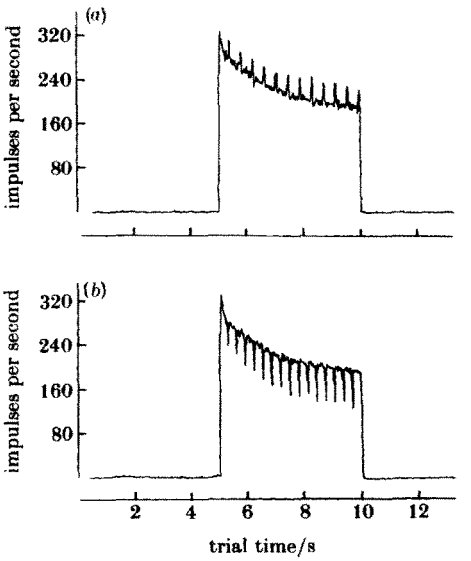

Figure 4.6: Curves from Maddess and Laughlin showing that the H1 neuron is sensitive to velocity contrast. The trial consists of 8.3s of stationary grating, then a phase where the grating moved at 58°/s for 6.7s. In the 6.7s, 16 equally spaced (a) increments and (b) decrements of 23.4°/s were added to the velocity of the grating. Source: From Maddess and Laughlin [4], Figure 4, pg. 258.

in Section 4.2. In the correlator, the output of the lowpass filter is correlated with the input signal when the latter signal reaches the neighboring pixel. We can see that the correlation between the output of the left filter with the input at the neighboring pixel is greater when the input signal moves from left to right than when the signal moves from right to left. The outputs of the multipliers are time averaged before they are subtracted, as shown at the bottom of Figure 4.7a, so that the dependence on the flicker at the input is removed. In Figure 4.7b, another variation of the correlator is shown where the input goes through 2 different filters, F_1 and F_2. We use this model to compute the temporal-averaged response of the correlator. We assume that the input signal is a sine wave, $I + \Delta I \sin(\omega t + \theta)$, where I is the mean intensity level, θ is the spatial phase, and ω is the temporal frequency. Let the spacing between the pixels be a, and let λ be the spatial wavelength of the input signal. The input to the

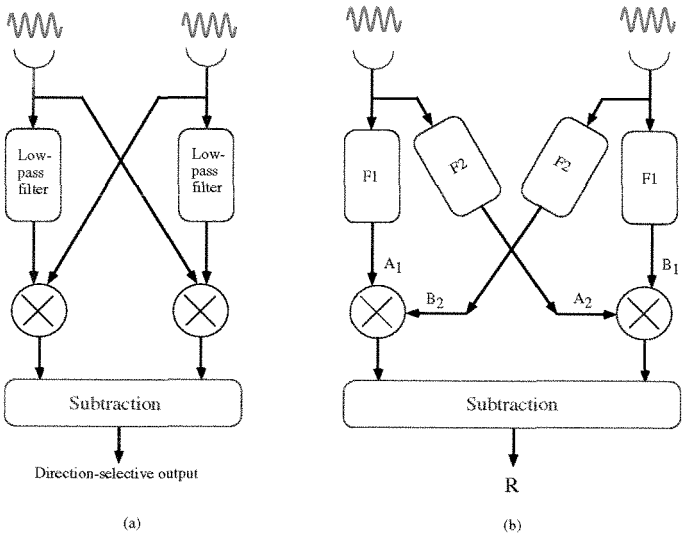

Figure 4.7: Correlation models. (a) This model was originally formulated by Hassenstein and Reichardt to model direction selectivity in the motion system of the beetle. The input at each pixel is delayed by a lowpass filter with a fixed time constant. The output of the filter is correlated with the input signal when the latter signal reaches the neighboring pixel. The outputs of the multipliers are time averaged before they are subtracted so that the common-mode dependence on the input can be removed. (b) A generic model of the correlator where the input at each pixel goes through two filters, F_1 and F_2, with different time constants before the outputs of the filters are multiplied together.

neighboring detector, is then $I + \Delta I \sin(\omega t + \theta + \frac{2\pi a}{\lambda})$.

Let the transfer function of F_1 be $L(\omega)e^{i\theta_l(\omega)}$, and that of F_2 be $H(\omega)e^{i\theta_h(\omega)}$. The outputs of the four filters are A_1, A_2, B_1, and B_2 as shown in Figure 4.7b. These outputs can be written as

$$\begin{aligned}
A_1 &= L(0)I + L(\omega)\Delta I \sin(\omega t + \theta + \theta_l(\omega)), \\
A_2 &= H(0)I + H(\omega)\Delta I \sin(\omega t + \theta + \theta_h(\omega)), \\
B_1 &= L(0)I + L(\omega)\Delta I \sin(\omega t + \frac{2\pi a}{\lambda} + \theta + \theta_l(\omega)), \\
B_2 &= H(0)I + H(\omega)\Delta I \sin(\omega t + \frac{2\pi a}{\lambda} + \theta_h(\omega) + \theta).
\end{aligned}$$

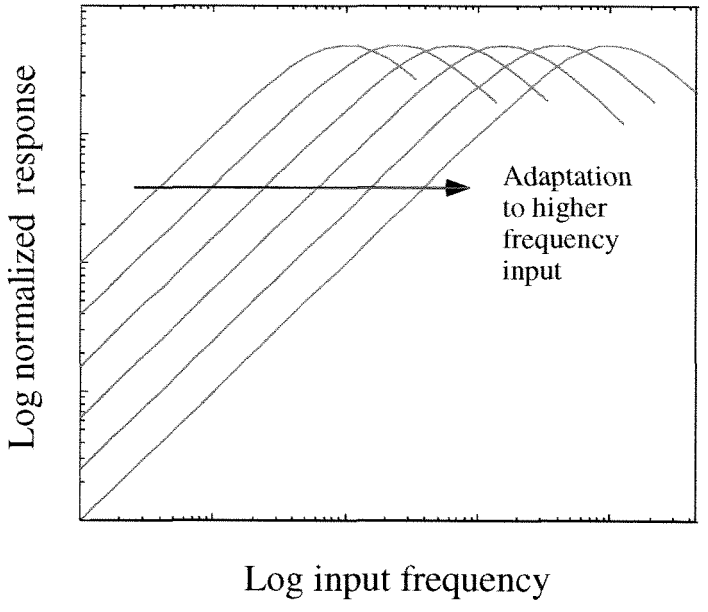

Figure 4.8: Output of the Hassenstein–Reichardt correlator for various fixed time constants. The family of curves shows that if the time constant of the filters in the correlator is made adaptive, the system can respond over a larger range of input frequencies.

The expected value of the correlated output, $A_1 * B_2$, is

$$\begin{aligned}
E[A_1 * B_2] &= E[L(0)H(0)I^2] + E[H(0)L(\omega)I\Delta I \sin(\omega t + \theta + \theta_l(\omega))] \\
&\quad + E[L(0)IH(\omega)\Delta I \sin(\omega t + \frac{2\pi a}{\lambda} + \theta_h(\omega) + \theta)] \\
&\quad + E[H(\omega)L(\omega)\Delta I^2 \sin(\omega t + \theta + \theta_l(\omega)) \sin(\omega t + \frac{2\pi a}{\lambda} + \theta_h(\omega) + \theta)] \\
&= L(0)H(0)I^2 + E[H(\omega)L(\omega)/2\Delta I^2(\cos(\theta_l(\omega) - \theta_h(\omega) - \frac{2\pi a}{\lambda}) \\
&\quad - \cos(2\omega t + 2\theta + \theta_l(\omega) + \theta_h(\omega) + \frac{2\pi a}{\lambda})] \\
&= L(0)H(0)I^2 + H(\omega)L(\omega)\Delta I^2 \cos(\theta_l(\omega) - \theta_h(\omega) - \frac{2\pi a}{\lambda})/2.
\end{aligned}$$

Similarly, the correlated output, $A_2 * B_1$, can be reduced to

$$E[A_2 * B_1] = L(0)H(0)I^2 + H(\omega)L(\omega)\Delta I^2 \cos(\theta_h(\omega) - \theta_l(\omega) - \frac{2\pi a}{\lambda})/2].$$

The final direction-selective output, R, which is $A_1 * B_2 - A_2 * B_1$, is

$$\begin{aligned} R &= \frac{H(\omega)L(\omega)}{2}\Delta I^2(\cos(\theta_l(\omega) - \theta_h(\omega) - \frac{2\pi a}{\lambda}) - \cos(\theta_h(\omega) - \theta_l(\omega) - \frac{2\pi a}{\lambda})) \\ &= H(\omega)L(\omega)\Delta I^2 \sin(\frac{2\pi a}{\lambda}) \sin(\theta_h(\omega) - \theta_l(\omega)). \end{aligned}$$

If the filters have the same time constant, τ, and the phase offset between the filters is 90°, then

$$H(\omega)L(\omega) = \frac{\omega\tau}{1 + \omega^2\tau^2}.$$

We can write the time-averaged output of this correlator as

$$R = \Delta I^2 \frac{\omega\tau}{1 + \omega^2\tau^2} \sin(\frac{2\pi a}{\lambda}).$$

The time constant of decay of the firing rate of the H1 neuron corresponds to the time constant of the lowpass filter in Figure 4.7a. In Figure 4.8, we show a family of curves corresponding to the output of the correlator over different temporal frequencies. Each curve in the plot corresponds to a certain fixed time constant of the filters. If the filters have an adaptive time constant, the family of curves illustrates the subsequent response of the correlator. The plot shows that a correlator with an adaptive time constant responds over a larger range of input frequencies, similar to the response of the H1 neuron in the fly.

4.4 Adaptive Correlation Model

I describe a variant of the correlation model (shown in Figure 4.10b), that I called the adaptive correlation model, where the time constant of the filters adapts to the motion input. The circuitry for adapting the time constant of the filters is shown in Figure 4.9a. The input first goes through both a lowpass and a highpass filter with the same time constant or cutoff frequency. The gain curves of these filters are shown in Figure 4.9b. The comparator in Figure 4.9a uses the difference in the peak amplitudes of the output of the filters as an error signal in adapting the time constant

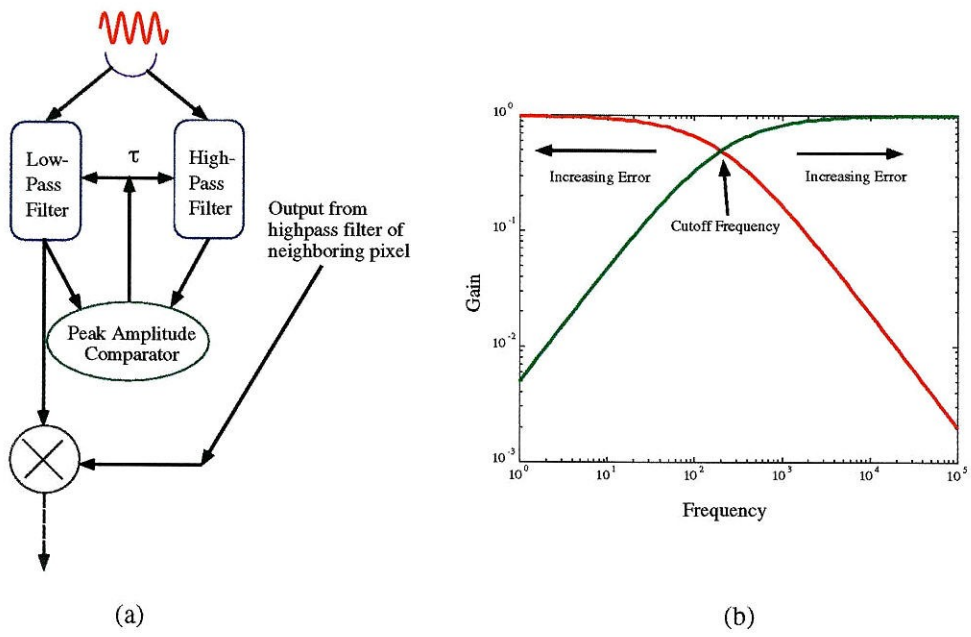

(a) (b)

Figure 4.9: Adaptive correlation model and the gain curves of the filters in the model. (a) The input signal goes through both a lowpass filter and a highpass filter with the same time constant. The comparator uses the difference between the peak amplitudes of the outputs of the filters as an error signal in adapting the time constant of the filters. (b) The gain curves of highpass and lowpass filters with the same cutoff frequency are shown in the plot. The magnitudes of the filter outputs are equal only at the cutoff frequency. The difference between the outputs increases as the input frequency deviates more from the cutoff frequency.

of the filters. From Figure 4.9b, we see that the error signal increases as the input frequency deviates further away from the present cutoff frequency or time constant. The comparator adapts the cutoff frequency of the filters until the cutoff frequency approximates that of the input. Thus, the cutoff frequency codes the time scale of the input. The adaptation process in this model is independent of the signal contrast and of direction of motion, and is spatially localized to each pixel, as observed in the experimental results from the H1 neuron [3][4].

One version of the Reichardt correlator circuit, (also called the **minimal correlation model**), which includes a lowpass filter and a highpass filter with the same time constant was proposed by Kirschfeld [28][29][30]. This configuration is shown in

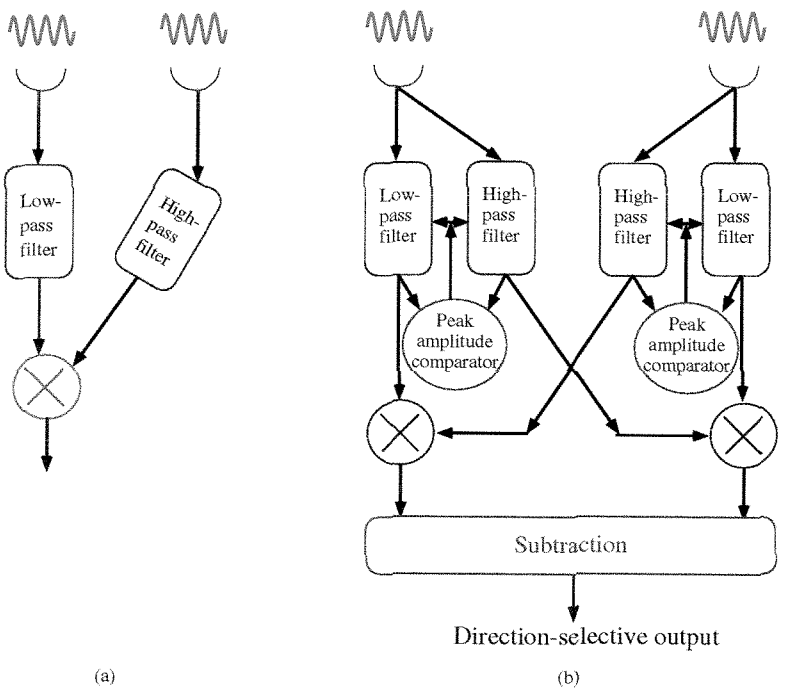

Figure 4.10: Adaptive correlation model.(a) Hassenstein–Reichardt correlator as modified by Kirschfeld. The filters consist of a lowpass filter and highpass filter with the same time constant. (b) The adaptive correlation model, which consists of Kirschfeld's correlator with the inclusion of the peak amplitude comparator. The peak amplitude comparator adapts the cutoff frequency of the filters so that the cutoff frequency matches the motion frequency. Thus, the time constant of the filters codes for the temporal resolution of the motion.

Figure 4.10a. The outputs of the filters have a 90° phase offset over all frequencies. The constant phase offset between the outputs allows maximal overlap in the correlation of the inputs, and hence extends the input range of the frequencies to which the correlator responds. Our time-constant adaptation circuitry can be incorporated in Kirschfeld's correlation model to form the adaptive correlation model, which is shown in Figure 4.10b.

4.5 aVLSI Model of the Adaptive Correlator

The adaptation circuitry in Figure 4.9 was implemented on an aVLSI circuit as shown in Figure 4.11. The lowpass filter is a follower integrator; the highpass filter is a

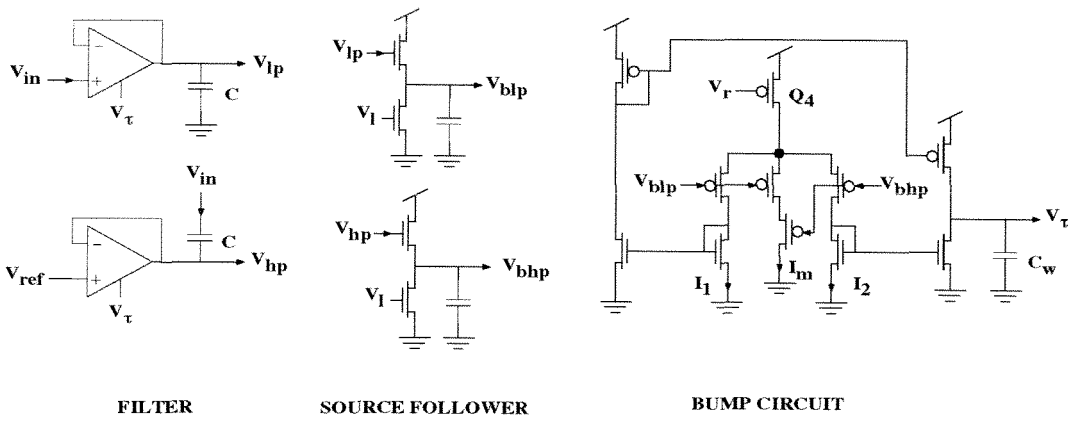

Figure 4.11: Circuitry for adaptation to the motion frequency. The input goes through two filters. The peak amplitudes of the outputs of the filters, $V_{\rm lp}$ and $V_{\rm hp}$, are obtained from the outputs of the source followers. These outputs, $V_{\rm blp}$ and $V_{\rm bhp}$, are compared by the bump circuit. The bias voltage, V_τ, that controls the time constant of the filters is charged or discharged depending on the difference between $V_{\rm blp}$ and $V_{\rm bhp}$.

follower differentiator. The time constant of the filters, τ, is determined by the capacitor, C and by the bias voltage, V_τ. The time constant, τ, is given by $\frac{C}{g_m} = \frac{C U_{\rm T}}{\kappa I} = \frac{C U_{\rm T}}{\kappa I_0 e^{k V_\tau / U_{\rm T}}}$. The output of each filter goes to a source follower operated as a peak detector, which outputs the maximum value of the filter outputs. The peak value is measured over a user-defined time constant determined by $V_{\rm l}$.

The outputs of all source followers are, in turn, connected to a bump circuit, described previously by Delbrück [31]. The operation of the bump circuit is as follows. The middle branch acts a current correlator between the two inputs. If the difference between the two inputs is small, then most of the bias current, I_b, flows through this branch. The current through this branch is

$$I_{\rm mid} = \frac{I_b}{1 + \frac{4}{S}\cosh^2 \frac{\kappa \Delta V}{2}},$$

where $\Delta V = V_{\rm blp} - V_{\rm bhp}$ and S is a geometric constant. If the input, $V_{\rm blp}$, is significantly greater than $V_{\rm bhp}$, then most of I_b flows through the left branch and V_τ is charged up. On the other hand, V_τ is discharged when $V_{\rm bhp} \geq V_{\rm blp}$.

The adaptation works as follows. If the input temporal frequency is greater than

the cutoff frequency (the inverse of τ) of the filters, then the output of the highpass filter will be larger in amplitude than the output of the lowpass filter. Since $V_{\mathrm{bhp}} \geq V_{\mathrm{blp}}$, V_τ is discharged, decreasing τ or increasing the cutoff frequency. The discharge of V_τ continues until the cutoff frequency is equal to the input frequency. Notice that, when the cutoff frequency approaches the input frequency, the discharging slows down because most of I_b is diverted to the middle branch of the bump circuit. This characteristic helps to ensure the stability of the circuit loop. Correspondingly, V_τ is charged when the input frequency is less than the cutoff frequency of the filters. In equilibrium, τ is matched to the input frequency.

4.6 Adaptation of the Filter Time Constant

In this section, we analyze the time response of the filters's time constant in the small-signal case, from the adaptation circuitry in Figure 4.11.

4.6.1 Dynamics of Time-Constant Adaptation

The time constant of the filters, τ, is determined by $\frac{C\mathrm{U_T}}{\kappa_n I} = \frac{C\mathrm{U_T}}{\kappa_n I_0 e^{\kappa V_\tau / \mathrm{U_T}}}$. The rate of change of τ can be determined by

$$\frac{\partial \tau}{\partial t} = \frac{\partial \tau}{\partial V_\tau}\frac{\partial V_\tau}{\partial t} = -\frac{\kappa_n}{\mathrm{U_T}}\tau\frac{\partial V_\tau}{\partial t}.$$

The rate of change of V_τ depends on the charging current, I_{lp}, and on the discharging current, I_{hp}, in the bump circuit according to the following equation:

$$C_{\mathrm{w}}\frac{\partial V_\tau}{\partial t} = I_{\mathrm{lp}} - I_{\mathrm{hp}}.$$

The rate of change of the time constant is then:

$$\frac{\partial \tau}{\partial t} = -\frac{\kappa_n}{C_{\mathrm{w}}\mathrm{U_T}}\tau(I_{\mathrm{lp}} - I_{\mathrm{hp}}).$$

The currents in the bump circuit depend on the outputs of the lowpass and high-

pass filters. We assume that the input signal is a sine wave of form, $V + \Delta V \sin(\omega t)$. The output of the lowpass filter, $V_{\rm lp}$ is $V + 2M\frac{1}{\sqrt{1+\omega^2\tau^2}}\sin(\omega t)$; that of the highpass filter is $V_{\rm hp} = V + 2M\frac{\omega\tau}{\sqrt{1+\omega^2\tau^2}}\sin(\omega t)$, where $2M$ is the p–p amplitude of the sine wave. Let $I_1 - I_2 = I_{\rm lp} - I_{\rm hp}$ in the bump circuit. Then

$$I_b = I_1 + I_2 + \alpha\frac{I_1 I_2}{I_1 + I_2}. \tag{4.1}$$

Let $I_1 = I_0 e^{(\kappa_n V_{\rm lp} - V)/{\rm U_T}}$ and $I_2 = I_0 e^{(\kappa_n V_{\rm hp} - V)/{\rm U_T}}$ and define $\frac{I_1}{I_2} = e^{\kappa_n(V_{\rm lp} - V_{\rm hp})} = e^{\kappa_n \Delta V}$. Then, substituting into Equation 4.1,

$$\begin{aligned} I_b &= I_2 e^{\kappa_n \Delta V/{\rm U_T}} + I_2 + \alpha\frac{I_2 e^{\kappa_n \Delta V/{\rm U_T}}}{1 + e^{\kappa_n \Delta V/{\rm U_T}}} \\ &= I_2(1 + e^{\kappa_n \Delta V/{\rm U_T}} + \alpha\frac{e^{\kappa_n \Delta V/{\rm U_T}}}{1 + e^{\kappa_n \Delta V/{\rm U_T}}}) \\ &= I_1(1 + e^{-\kappa_n \Delta V/{\rm U_T}} + \alpha\frac{e^{-\kappa_n \Delta V/{\rm U_T}}}{1 + e^{-\kappa_n \Delta V/{\rm U_T}}}). \end{aligned}$$

Solving for $I_1 - I_2$ and letting $x = \kappa_n \Delta V/{\rm U_T}$, we obtain

$$\begin{aligned} I_1 - I_2 &= I_b(\frac{1 + e^{-x}}{(1 + e^{-x})^2 + \alpha e^{-x}} - \frac{1 + e^{x}}{(1 + e^{x})^2 + \alpha e^{x}}) \\ &= I_b\frac{(1 + e^{-x})(1 - e^{-x})}{(1 + e^{-x})^2 + \alpha e^{-x}} \\ &= I_b\frac{\sinh(\kappa_n \Delta V/{\rm U_T})}{\alpha/2 + 2\cosh^2(\kappa_n \Delta V/(2{\rm U_T}))}. \end{aligned}$$

So the rate of change of the time constant is defined as follows:

$$\frac{1}{\tau}\frac{\partial \tau}{\partial t} = -\frac{\kappa_n I_b}{C_{\rm w}{\rm U_T}}[\frac{\sinh(\kappa_n \Delta V/{\rm U_T})}{\alpha/2 + 2\cosh^2(\kappa_n \Delta V/(2{\rm U_T}))}],$$

where ΔV is the difference between the peak amplitudes of both filters.

$$\begin{aligned} \Delta V &= V_{\rm bhp} - V_{\rm blp} \\ &= M(\frac{\omega\tau}{\sqrt{1 + \omega^2\tau^2}} - \frac{1}{\sqrt{1 + \omega^2\tau^2}}), \end{aligned}$$

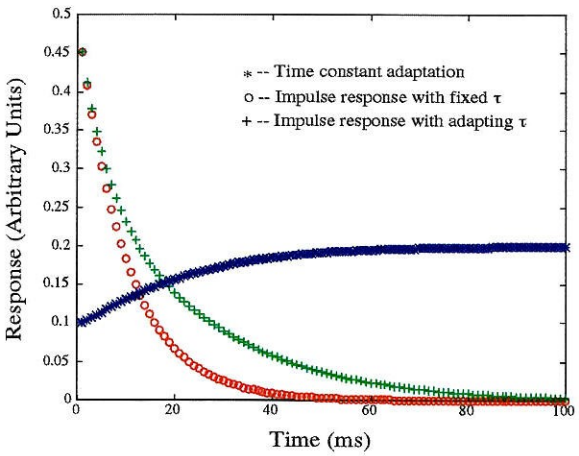

Figure 4.12: Adaptation of the time constant of system to a change in the motion frequency. The curve with $*$ shows the time constant adaptation to its final value. The curve with $\circ$ shows the impulse response of a lowpass filter with a fixed time constant; the curve with $+$ shows the impulse response of a lowpass filter with the adapting time constant.

where $2M$ is the p–p amplitude of the input signal to the filters. For small x, $\sinh(x) \approx x, \cosh(x) = 1$. So,

$$\frac{\partial \tau}{\partial t} \cong -\frac{2\kappa_n^2 I_b}{(\alpha+4)C_{\mathrm{w}}\mathrm{U_T}} M \frac{\tau(\omega\tau - 1)}{\sqrt{1+\omega^2\tau^2}}. \tag{4.2}$$

The updating rate for τ is then $\gamma = \frac{2\kappa_n^2 I_b M}{(\alpha+4)C_{\mathrm{w}}\mathrm{U_T}}$. Equation 4.2 also shows that when $\omega\tau = 1$, τ is in equilibrium and the time constant of the system is the inverse of the input frequency. Figure 4.12 shows a plot of the time constant of the filters adapting with time as described by Equation 4.2. The figure also shows the impulse response of a lowpass filter with both a fixed time constant and an adapting time constant.

If the input is a superposition of two input frequencies, ω_1 and ω_2, then the difference in the inputs to the bump circuit is

$$\Delta V = M\left(\frac{\omega_1\tau - 1}{\sqrt{1+\omega_1^2\tau^2}} + \frac{\omega_2\tau - 1}{\sqrt{1+\omega_2^2\tau^2}}\right).$$

The updating ends when $\Delta V = 0$; that is,

$$(\omega_1\tau - 1)(\sqrt{1+\omega_2^2\tau^2}) + (\omega_2\tau - 1)(\sqrt{1+\omega_1^2\tau^2}) = 0.$$

Solving for τ, we see that the new time constant is the inverse of the geometric mean of the two frequencies:

$$\tau = \sqrt{1/(\omega_1\omega_2)}.$$

4.6.2 Steady-state Response

The response of the Hassenstein–Reichardt correlator as shown in Section 4.3 is

$$R = \Delta I^2 \frac{\omega\tau}{1+\omega^2\tau^2} \sin(\frac{2\pi a}{\lambda}).$$

In the adapted steady-state case, $R = \Delta I^2 \sin(\frac{2\pi a}{\lambda})/2$. The direction-selective output thus conveys no information about the temporal frequency. However, the data from Maddess and Laughlin [4] show that the steady-state response of the H1 neuron changes as a function of temporal frequency as shown in Figure 4.13a. The data from their work also indicate that the time constant of the system decays with time to a quiescent time constant when no input is present to the system. The adaptation circuitry in Figure 4.11 does not provide for a quiescent time constant.

There is an important reason for not adapting τ to be the inverse of the temporal frequency. Figure 4.8 shows that the response of the correlator is maximal at $\omega\tau = 1$. Hence, the adapted response of the correlator sits at the peak of the curve and does not sit on the high gain portion of the curve. The adapted response should be on either side of the peak so that the correlator will be highly sensitive to any changes in the temporal frequency. In Section 4.7, I show that how the circuit in Figure 4.11 can be modified so that the output of the correlator sits on the high-gain part of the curve, as shown in Figure 4.14. The sensitivity of the correlator output is increased, because any change in the motion frequency leads to a greater change

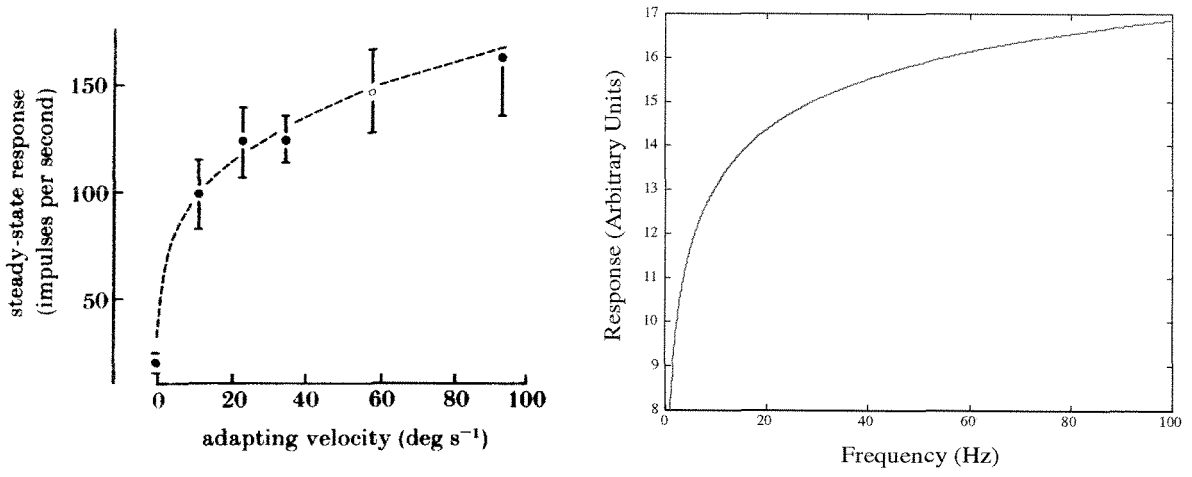

(a) (b)

Figure 4.13: Comparison of the steady-state adapted responses of the H1 neuron and of the model for different adapting velocities. (a) Steady-state adapted response of the H1 neuron for different adapting velocities as measured by Maddess and Laughlin. Source: From Maddess and Laughlin [4], Figure 7, pg. 261. (b) Steady-state adapted response as computed from the modified adaptation dynamics described by Equation 4.6.

in the correlator output. The fact that the adapted time constant is not the exact inverse of the temporal frequency would explain why the slope of the fit in Figure 4.4 and Figure 4.5 is less than -1.

4.7 Dynamics of Time-Constant Adaptation with Quiescent Time Constant

The circuit shown in Figure 4.11 can be modified so that the system has a quiescent time constant. The new circuit is shown in Figure 4.15. The quiescent time constant is set by the voltage, V_e, in the bump circuit. The dynamics of this new system is described in the remainder of this section.

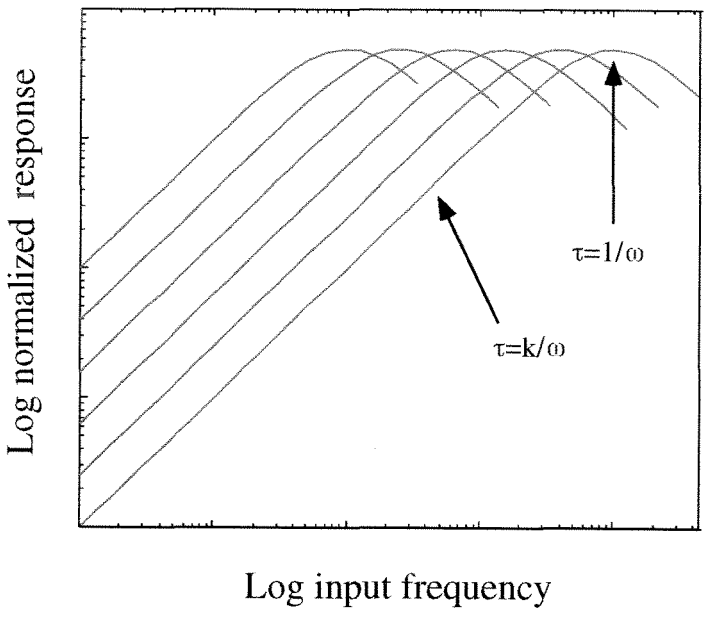

Figure 4.14: Plot shows that the adapted output of the Hassenstein–Reichardt correlator should sit on the high gain portion of the curve. The constant, k, describes the location of each steady-state adaptation relative to $\tau = 1/\omega$.

4.7.1 Rate Change of Time-constant Adaptation

The new rate of change of time constant is defined as

$$\frac{\partial \tau}{\partial t} = -\gamma\tau\left(\frac{\omega\tau - 1}{\sqrt{1+\omega^2\tau^2}} + g_m(V_e - V_\tau)\right), \tag{4.3}$$

where g_m is the transconductance of the follower and V_e is the voltage that determines the quiescent time constant. If we equate the left side of Equation 4.3 to zero, we get

$$\frac{\omega\tau - 1}{\sqrt{1+\omega^2\tau^2}} + g_m V_e = g_m V_\tau. \tag{4.4}$$

Substituting $V_\tau = \frac{U_T}{\kappa}\ln(\frac{CU_T}{\kappa I_0 \tau})$ into Equation 4.4, we have

$$\frac{\omega\tau - 1}{\sqrt{1+\omega^2\tau^2}} + g_m V_e = g_m \frac{U_T}{\kappa}\ln(\frac{CU_T}{\kappa I_0 \tau}).$$

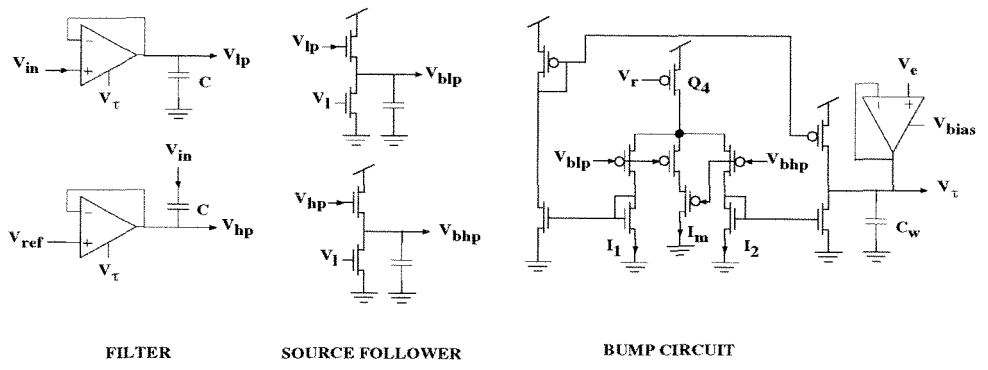

Figure 4.15: Circuit modified from the one shown in Figure 4.11 so that it has a quiescent time constant. The quiescent time constant is set by the voltage, V_e, in the bump circuit.

Let $\alpha = g_m V_e$, $\beta = g_m \frac{U_T}{\kappa}$. Then,

$$\frac{\omega\tau - 1}{\sqrt{1+\omega^2\tau^2}} + \alpha = \beta \ln(\frac{CU_T}{\kappa I_0 \tau}).$$

We rearrange the terms to solve for ω, and let $X = (\beta \ln(\frac{CU_T}{\kappa I_0 \tau}) - \alpha)^2$:

$$\begin{aligned} (\omega\tau - 1)^2 &= (1+\omega^2\tau^2)(\beta \ln(\frac{CU_T}{\kappa I_0 \tau}) - \alpha)^2 \\ &= (1+\omega^2\tau^2)X. \end{aligned} \tag{4.5}$$

From Equation 4.5, we get $\omega = \frac{1 \pm \sqrt{1-(1-X)^2}}{\tau(1-X)}$. The implicit expression for the adapted time constant is $\tau = \frac{1 \pm \sqrt{1-(1-X)^2}}{\omega(1-X)}$. Solving for R in steady state, we have

$$\begin{aligned} R &= \Delta I^2 \frac{\omega\tau}{1+\omega^2\tau^2} \sin(\frac{2\pi a}{\lambda}) \\ &= \frac{\Delta I^2 (1-X)}{2} \sin(\frac{2\pi a}{\lambda}) \\ &= \frac{\Delta I^2}{2}(1 - (\beta \ln(\frac{CU_T}{\kappa I_0 \tau}) - \alpha)^2) \sin(\frac{2\pi a}{\lambda}). \end{aligned} \tag{4.6}$$

Figure 4.13 shows a comparison between the steady-state response of H1 as measured by Maddess and Laughlin and the steady-state response of the correlator as defined by Equation 4.6.

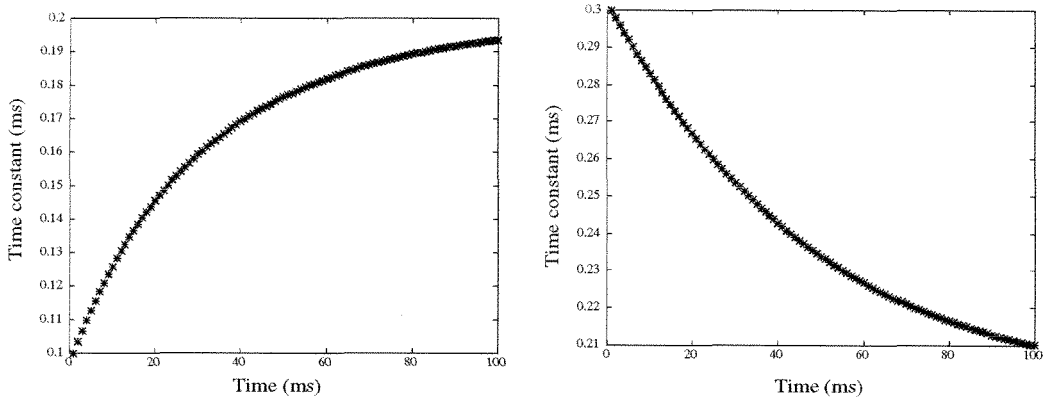

(a) (b)

Figure 4.16: Plots showing the recovery of the filters's time constant back to the quiescent time constant. (a) Recovery of the system from motion with a high temporal frequency. (b) Recovery of the system from motion with a high temporal frequency.

4.7.2 Recovery Time

When the stimulus stops moving, the time constant of the system adapts down to the quiescent value with dynamics controlled by:

$$\frac{\partial \tau}{\partial t} = -\gamma\tau(g_m(V_e - V_\tau)).$$

V_e defines the quiescent time constant, τ_0, as follows:

$$V_e = \frac{U_T}{\kappa}\ln(c/\tau_0),$$

where $c = \frac{\kappa I_0}{C U_T}$. Similarly, V_τ defines the time constant, $\tau(t)$, as follows:

$$V_\tau = \frac{U_T}{\kappa}\ln(c/\tau(t)). \tag{4.7}$$

Integrating Equation 4.7, we have

$$\begin{aligned}\frac{\partial \tau}{\partial t} &= -\gamma\tau(g_m U_T/\kappa(\ln(c/\tau_0) - \ln(c/\tau(t))) \\ &= -K\tau(\ln(c/\tau_0) - \ln(c/\tau(t)))\end{aligned}$$

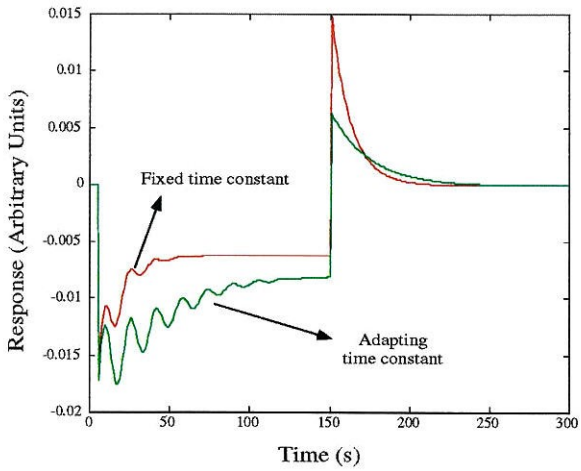

Figure 4.17: Simulated step response of correlator to a moving sine wave grating with a fixed time constant and an adapting time constant.

$$= \quad -K\tau(\ln(\tau(t)/\tau_0)),$$

where $K = \gamma g_m \mathrm{U_T}/\kappa$.

The dynamics of the recovery of the system when the input stimulus at different temporal frequencies stops moving is shown in Figure 4.16. Figure 4.16a shows the recovery of the system from a stimulus moving a high temporal frequency and Figure 4.16b shows the recovery of the system from a stimulus moving a low temporal frequency.

4.8 Step Response of Correlator to a Sine-Wave Input

We look at the step response of the correlator to a sine-wave input when the input is initially stationary from $-\infty$ to 0. The input then is displaced stepwise. The analysis is similar to that described by de Ruyter and colleagues [3]. Let the signal at the first receptor be $x_1^- = \Delta I \sin(\phi)$ at $t \leq 0$, and $x_1^+ = \Delta I \sin(\phi - \eta)$ at $t \geq 0$. The signal at the second receptor is shifted by a spatial phase of θ_s. Hence, the input here is

$y_1^- = \Delta I \sin(\phi + \theta_s)$ at $t \leq 0$, and is $y_1^+ = \Delta I \sin(\phi + \theta_s - \eta)$ at $t \geq 0$. The step response of the lowpass filter is $1 - e^{-t/\tau}$, while the step response of the highpass filter is $e^{-t/\tau}$. We ignore the mean luminance, I, since the terms involving I will go to 0 when we compute R. Using the correlator intermediate terms defined in Figure 4.7, the output of the lowpass filter, F_1, of the first receptor for $t \geq 0$ is

$$A_1 = x_1^- + (x_1^+ - x_1^-)(1 - e^{-t/\tau}).$$

Similarly, the output of the highpass filter, F_2, of the first receptor for $t \geq 0$ is

$$A_2 = x_1^- + (x_1^+ - x_1^-)e^{-t/\tau}.$$

Corresponding filter outputs of the second receptor are,

$$\begin{aligned} B_1 &= y_1^- + (y_1^+ - y_1^-)(1 - e^{-t/\tau}) \\ B_2 &= y_1^- + (y_1^+ - y_1^-)e^{-t/\tau}. \end{aligned}$$

The correlated output, R, is

$$\begin{aligned} R &= B_2 \times A_1 - B_1 \times A_2 \\ &= (x_2^+ x_1^- - x_1^+ x_2^-)(2e^{-t/\tau} - 1) \\ &= \Delta I^2 \sin \frac{2\pi \Delta x}{\lambda} \sin \eta (2e^{-t/\tau} - 1). \end{aligned}$$

The response of the correlator with a fixed time constant and an adapting time constant to a sine-wave grating that starts and stops moving is shown in Figure 4.17.

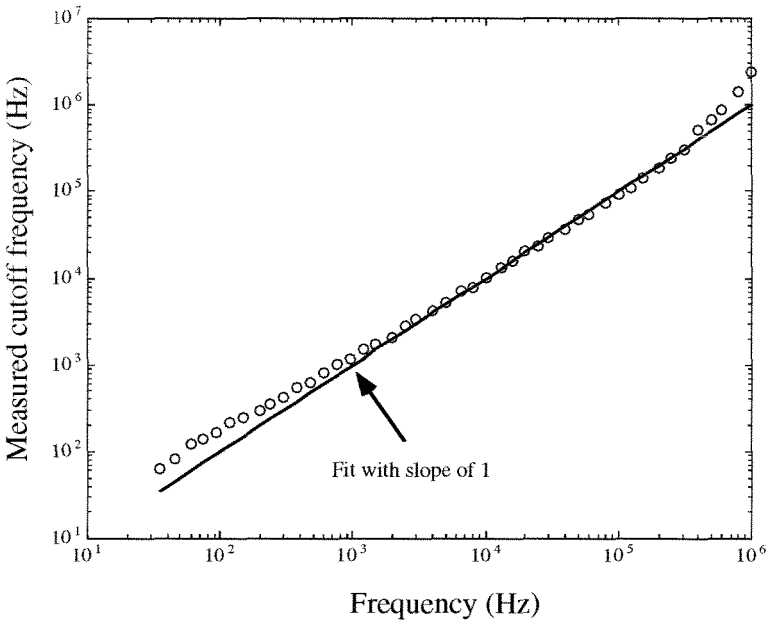

Figure 4.18: Adaptation of the cutoff frequency of the filters to a sine wave with a p–p amplitude of 100mV. The frequency of the sine wave was varied over 4 decades, and the cutoff frequency of the filters was measured after the time constant of the system has adapted to the new input frequency.

4.9 Results from the aVLSI Model of the Adaptation Circuitry

In this section, we show results from a silicon implementation of the adaptation circuitry using analog subthreshold circuits. The VLSI circuitry is shown in Figure 4.11. We have not yet implemented the modified circuit with a quiescent time constant as shown in Figure 4.15. The input to the adaptation circuitry consists of a sine wave with a p–p amplitude of 100mV. The frequency of the sine wave was varied over four decades, and the cutoff frequency of the filters was measured after the system had adapted to the new input frequency. These data are shown in Figure 4.18; they demonstrate that the adaptive model adapts the cutoff frequency of the filters linearly to the input temporal frequency for over 4 decades of frequency.

The p–p outputs of the lowpass and highpass filters were measured at each adapt-

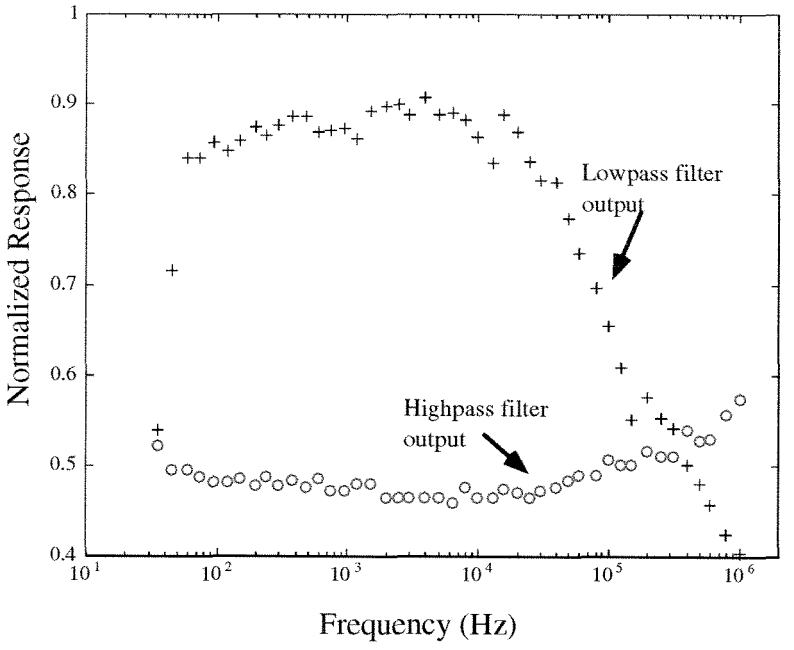

Figure 4.19: Normalized p-p outputs of lowpass and highpass filters over 4 decades of frequency. The p-p outputs were normalized with respect to the p–p amplitude of the input. The data deviate around 10 kHz, because the cutoff frequency of the readout circuits through which the outputs travel, starts to affect the data.

ing frequency, and normalized with respect to the p–p amplitude of the input. The normalized data are shown in Figure 4.19. The time constant, τ, of the filters can be described by $\tau = C/G$, where G is the conductance and C is the capacitance of each filter. Because I miscalculated the capacitor sizes on one of the filters, the time constant of the filters is not at the input frequency, and the output amplitudes of the two filters are different, as shown in Figure 4.19. The data also show that the output amplitudes of the two filters do not vary substantially over the range of input frequencies used, indicating that the system is adapting the time constant of the filters. The data start deviating around 10 kHz, because the outputs of the filters go through readout circuits on the chip before they are measured offchip, and the cutoff frequency of the readout circuits starts to affect the output data.

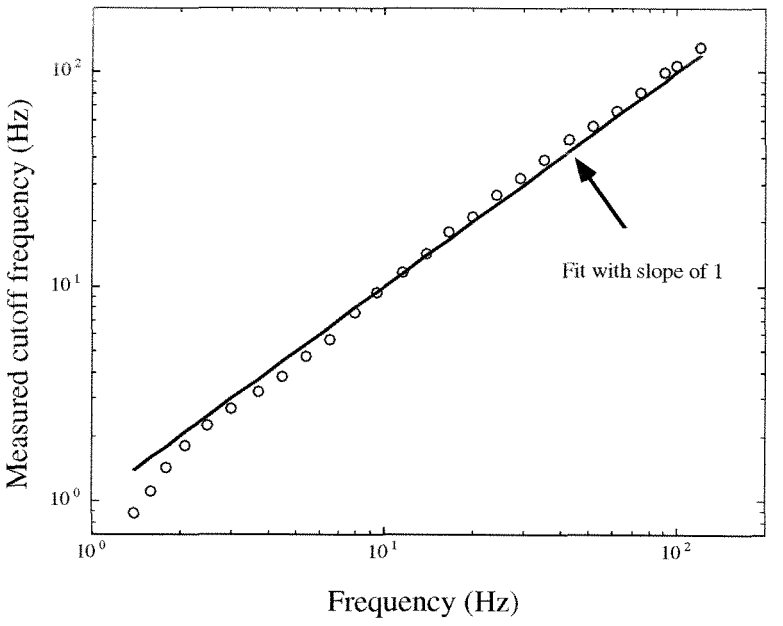

Figure 4.20: Adaptation of the cutoff frequency of the filters to various input frequencies of a sine wave that drives a red LED light incident on the chip. The contrast from the LED is about 0.3.

4.9.1 Adaptation Data after Filtering through the Photoreceptor

We next illuminated the chip with a red LED light that was driven by a sine wave. The contrast from the LED was about 0.3 as measured by a photometer. A photoreceptor circuit on chip transduced the light from the LED and passed the signal to the adaptive correlator. The photoreceptor circuit acts like a lowpass temporal filter. The frequency of the sine wave driving the LED was varied, and the cutoff frequency of the filters was then measured after the circuit had adapted to each input frequency. The data in Figure 4.20 show that the cutoff frequency of the filters adapts linearly to the input temporal frequency from the LED for about 2 decades. This range of 1 Hz to 100 Hz is within the range of natural moving objects.

4.9.2 Adaptation Dynamics of Adaptive Correlator

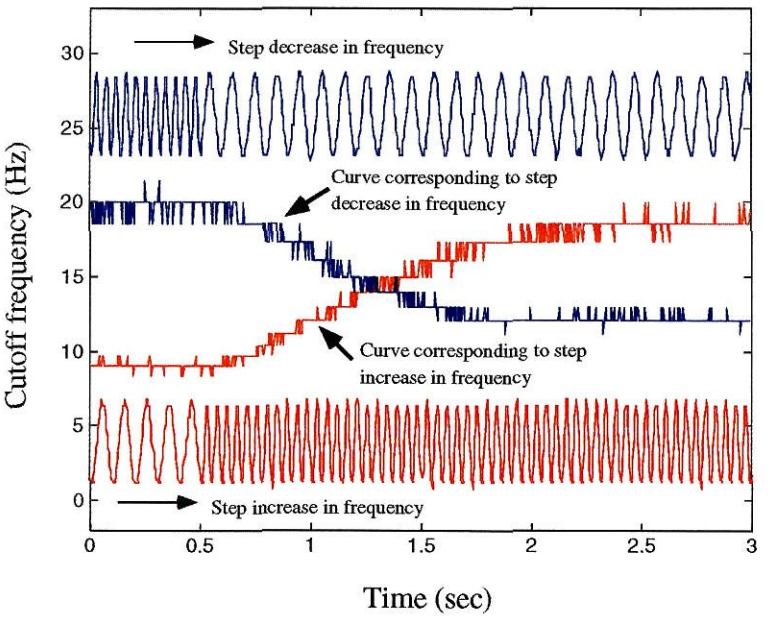

Figure 4.21: Curves showing adaptation of the cutoff frequency of the filters to a 58 percent step increase from a 20Hz sine wave, and to a 58 percent step decrease to a 20Hz sine wave that drives a red LED light incident on the chip.

In the next set of experiments, the incident light on the chip was again from the red LED, which was driven by a 0.35V p–p 20Hz sine wave riding on top of a 0.8V DC voltage. The contrast from the LED was 0.3. We first adapted the system to an input frequency of 20Hz, before a step increase of 58 percent in the frequency occurred. We measured the change in cutoff frequency of the filters in response to the new frequency. Figure 4.21 shows the cutoff frequency of the filters as it adapts monotonically to the new input frequency. After the system had adapted to this new frequency, a step decrease of 58 percent back down to 20Hz occurred, and we again measured the cutoff frequency of the filters. The adaptation of the cutoff frequency to the 20Hz sine wave is again shown in Figure 4.21.

We then used a 20Hz square wave, instead of a sine wave, to drive the red LED, so that we could see the response of the adaptation circuitry to a superposition of sine waves, rather than to only a pure sine wave. Figure 4.22 shows the adaptation of the cutoff frequency of the filters to a step increase of 58 percent in the frequency of a 20Hz square wave, as compared to the adaptation of the cutoff frequency to a

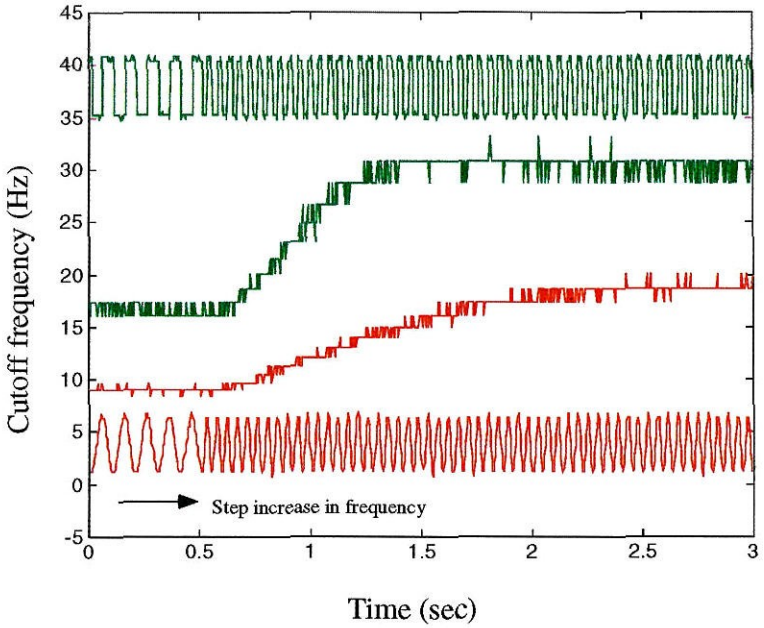

Figure 4.22: Curves showing the adaptation of the cutoff frequency to a step increase of 58 percent in the input frequency of a 20Hz square wave (top curve), and of a 20Hz sine wave driving a red LED incident on the chip (bottom curve).

20Hz sine wave driving the LED. The cutoff frequency adapts to a higher value in the case of the square wave, because the square wave contains higher harmonics of the fundamental frequency of 20Hz.

4.10 Comparisons with other Models

De Ruyter van Steveninck and colleagues in their paper proposed that the adapted responses of the H1 neuron can be predicted by the Reichardt's correlator with adapting lowpass filters. Clifford and Langley [32] have also proposed a model of the temporal adaptation of H1, where the locally integrated response of a one-dimensional array of EMDs is fed back to adapt the time constants of the filters. Their model, which is a form of a leaky predictor, is able to predict many of the adaptation experimental results of Maddess and Laughlin [4], and of Jian and Horridge [26]. My model differs from their model in that the signal used in adapting the time constants of the filter

is obtained from the filters before the correlation. Hence, local spatial integration before the global integration of H1 from the EMDs is not required.

Bibliography

[1] S. P. McKee, and L. Welch, "Sequential recruitment in the discrimination of velocity," *Journal of Optical Society of America A*, **2:2**, pp. 243–251, 1985.

[2] C. Koch, "Computation and the single neuron," *Nature*, **385:6613**, pp. 207–210, 1997.

[3] R. R. de Ruyter van Steveninck, W. H. Zaagman, and H. A. K. Mastebroek, "Adaptation of transient responses of a movement-sensitive neuron in the visual system of the blowfly *Calliphora erythrocephala*," *Biological Cybernetics*, **54:4-5**, pp. 223–236, 1986.

[4] T. Maddess, and S. B. Laughlin, "Adaptation of the motion-sensitive neuron H1 is generated locally and governed by contrast frequency," *Proc. R. Soc Lond*, **B 225:1239**, pp. 251–275, 1985.

[5] A. Borst, and M. Egelhaaf, "Temporal modulation of luminance adapts time constant of fly movement detectors," *Biological Cybernetics*, **56:4**, pp. 209–215, 1987.

[6] M. Egelhaaf and W. Reichardt, "Dynamic response properties of movement detectors: theoretical analysis and electrophysiological investigation in the visual system of the fly," *Biol. Cybernetics*, **56**, pp. 69–87, 1987.

[7] K. Hausen, "Monokulare und binokulare Bewegungsauswertung in der Lobula-Platte der Fliege," *Verh Dtsch Zool Ges*, **74**, pp. 49–70, 1981.

[8] K. Hausen, "The lobula-complex of the fly: structure, function and significance in visual behavior," in *Photoreception and vision in invertebrates*, M. A. Ali, Editor, pp. 523–559, Plenum, New York, 1984.

[9] K. Hausen, "Motion sensitive interneurons in the optomotor system of the fly. I. The horizontal cells: structure and signals," *Biol. Cybernetics*, **45**, pp. 143–156, 1982.

[10] K. Hausen, "Motion sensitive interneurons in the optomotor system of the fly. II. The horizontal cells: receptive field organization and response characteristics," *Biol. Cybernetics*, **46**, pp. 67–79, 1982.

[11] R. Hengstenberg, "Common visual properties of giant vertical cells in the lobula plate of the blowfly *Calliphora*," *J. Comp. Physiology*, **149**, pp. 179–193, 1982.

[12] K Hausen and C. Wehrhahn, "Neural circuits mediating visual flight control in flies. II. Separation of two control systems by microsurgerical brain lesions," *Journal of Neuroscience*, **10**, pp. 351–360, 1990.

[13] M. Egelhaaf, K Hausen, W. Reichardt, and C. Wehrhahn, "Visual course control in flies relies on neuronal computation of object and background motion," *Trends in Neuroscience*, **11**, pp. 351–358, 1988.

[14] N. J. Strausfeld and C. Gilbert, "Small-field neurons associated with oculomotor control in muscoid flies: cellular organization in the lobula plate," *Journal of Comparative Neurology*, **316**, pp. 56–71, 1992.

[15] M. Egelhaaf, and A. Borst, "Transient and steady-state response properties of movement detectors," *Journal of the Optical Society of America A*, **6:1**, pp. 116–127, 1989.

[16] A. Borst, "How do flies land?" *BioScience*, **40:4**, pp. 292–299, 1990.

[17] W. Reichardt and T. Poggio, "Figure-ground discrimination by relative movement in the visual system of the fly, Part I: Experimental results," *Biological Cybernetics*, **35**, pp. 81–100, 1979.

[18] W. Reichardt,T. Poggio, and K. Hausen, "Figure-ground discrimination by relative movement in the visual system of the fly, Part II: Towards the neural circuitry," *Biological Cybernetics*, **46**, pp. 1–30, 1983.

[19] J. Haag, M. Egelhaaf, and A. Borst, "Dendritic integration of motion information in visual interneurons of the blowfly," *Neuroscience Letters*, **140**, pp. 173–176, 1992.

[20] J. Haag and A. Borst, "Amplification of high-frequency synaptic inputs by active dendritic membrane processes," *Nature*, **379**, pp. 639–641, 1996.

[21] K. Hausen and M. Egelhaaf, "Neural mechanisms of visual course control in insects," In *Facets of vision*, ed. D. Stavenga and R. Hardie, pp. 360–390, Berlin, Springer–Verlag, 1989.

[22] N. Franceschini, A. Riehle, and A. Le Nestour, "Directionally-selective motion detection by insect neurons," In *Facets of vision*, ed. D. Stavenga and R. Hardie, pp. 391–424, Berlin, Springer–Verlag, 1989.

[23] N. Franceschini, "Early processing of colour and motion in a mosaic visual system," *Neuroscience Research, Suppl. 2*, pp. S17-S49, 1985.

[24] W. H. Zaagman, H. A. K. Mastebroek, and R. R. de Ruyter van Steveninck, "Adaptive strategies in fly vision: on their image-processing qualities," *IEEE Transactions on Systems, Man, and Cybernetics*, **13:5**, pp. 900–906, 1983.

[25] S. B. Laughlin, "Coding efficiency and visual processing," in *Vision: Coding and Efficiency*, C. Blakemore, ed. Cambridge Univ. Press, Cambridge, pp. 25–31, 1993.

[26] S. Jian, and G. A. Horridge, "The H1 neuron measures change in velocity irrespective of contrast frequency, mean velocity or velocity modulation frequency," *Phil. Trans. R. Soc. London.* **B331**, pp. 205–211, 1991.

[27] J. P. H. van Santen, and G. Sperling, "Elaborated Reichardt detectors," *Journal of the Optical Society of America, A*, **2:2**, pp. 300–321, 1985.

[28] K. Kirschfeld, "The visual system of Musca: Studies on optics, structure and function," in *Information Processing in the Visual Systems of Arthropods*, R. Wehner, ed. Springer-Verlag, Berlin, Heidelberg, New York, pp. 61–74, 1972.

[29] E. Buchner, "Elementary movement detectors in an insect visual system," *Biological Cybernetics*, **24**, pp. 85–101, 1976.

[30] W. H. Zaagman, H. A. K. Mastebroek, and J. W. Kuiper, "On the correlation model: Performance of a movement detecting neural element in the fly visual system," *Biol. Cybernetics*, **31**, pp. 163–168, 1978.

[31] T. Delbrück, "*Bump* circuits for computing similarity and dissimilarity of analog voltages," *Int. Joint Conf. on Neural Networks*, Seattle, WA, 1991.

[32] C. W. G. Clifford, and K. Langley, "A model of temporal adaptation in fly motion vision," *Vision Research*, **36:16**, pp. 2595–2608, 1996.

Chapter 5 Analog Model of Direction Selectivity

Most analog motion circuits use robust features extracted through thresholding or zero-crossings. The input signals are either binary or discretized in time. In cases where a threshold is set, only high-contrast signals are detected as robust features because the low-contrast signals are at the same level as the noise in the circuit. However, from the optomotor experiments in flies, we know that the fly is able to compute motion from a minimum contrast of 0.005. In this chapter, I propose a novel analog method of computing local direction selectivity from continuous, graded inputs through **temporal averaging** and **mutual inhibition**. The motion circuit does not extract discretized signals, but rather does a continuous-time computation from the graded input signals. It integrates the input information over time before making a decision on the direction of motion of the stimulus. The latency for low-contrast signals is longer than that for high-contrast signals, since the circuit takes a longer time to integrate the information from the low-contrast signal. The model implements most of the components of the traditional Reichardt model including the temporal averaging block. Previous circuit models have not implemented temporal averaging with continuous signals. The mutual inhibition block also models the inhibition seen in the direction-selective cells in the lobula plate. This analog circuit model shows that local direction selectivity can be computed through correlation of continuous-time signals.

5.1 Direction-Selective Models

The Hassenstein–Reichardt model [1] describes the properties of the direction-selective cells in the fly. This model has been modified by Santen and Sperling to handle di-

rection selectivity in the human visual system [2][3]. Specifically, the researchers included spatial filters in front of the Reichardt model. These filters correspond to prefiltering executed in the areas preceding the motion processing layers. Santen and Sperling also showed that the correlator model and the spatiotemporal energy model are equivalent even though the subblocks of the models look different. The Santen–Sperling–Reichardt model also applies to the fly visual system, where the filters represent the spatial and temporal filters in the retina, lamina, and medulla. The importance of the spatiotemporal filtering in the vertebrate retina before motion computation has also been expounded by Beaudot [4] and by Boahen [5]. The spatiotemporal filtering models in flies were discussed in Chapter 3.

5.2 History of Motion Chips

Motion algorithms have been traditionally implemented on serial computers with CCD cameras as the front end. As a result, the algorithms are constrained by the processing speed of the computers themselves and by the frame rate of CCD cameras. Initially, the bottleneck was the speed of the computers, but as speeds of microprocessors and DSP chips increased, the bottleneck eventually shifted to the frame rate of the CCDs. These systems are cumbersome because of the sizes of the camera and of the computer. In the past decade, researchers have shifted their interest to combining the sensor and the motion circuitry on the same chip or on a set of chips. The motion algorithms are implemented in the analog, digital, or hybrid domains for parallelism and speed. The sensors are also replaced by continuous-time CMOS sensors. The set of chips can then be used as the front end to surveillance cameras or to autonomous navigating platforms. In the neuromorphic world, the outputs of these chips can be used for saccadic and smooth pursuit systems, and for active vision.

In the domain of neuromorphic-inspired motion chips, the circuits either use intensity-based input or features obtained from zero-crossings or thresholding. The motion algorithms implemented are based on one of the following: the gradient method [8], the correlation method [9][10][11][12][13][14][15][16][17], the energy method

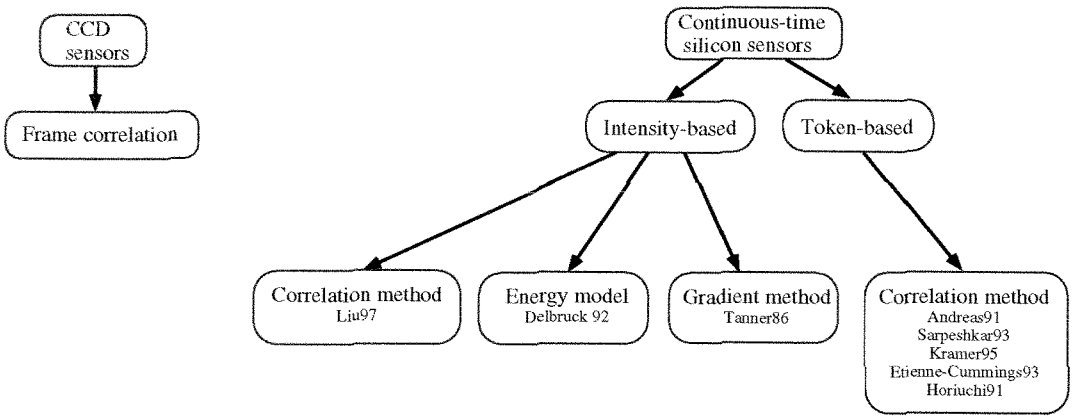

Figure 5.1: Tree diagram of the various motion schemes implemented in silicon.

[18], and the Barlow-Levick's model [19][20] which describes direction selectivity in the rabbit's retina. Figure 5.1 shows a tree diagram of the different implemented versions. These tree diagram does not list other motion systems that use CCD/CMOS hybrids or systems that implement frame correlation with CMOS sensors [21]. Comparisons of the different systems have been explicated by Sarpeshkar and colleagues [13] and also by Etienne-Cummings [16]. Some of these implementations provide direction selectivity information only; others provide both speed and direction-selectivity outputs. The factors that decide the implementation of a motion algorithm are based on the visual input, the sensor, the computing substrate, and also the number of transistors. Frequently, since the sensor is combined with the motion circuitry within the same pixel, the pixel spacing grows disproportionately with the sensor area. The increase in the pixel dead area compromises the subsequent motion process. These compromises are outlined in Chapter 2. Hence, a more efficient motion algorithm might be compromised by the extra number of transistors needed to implement the function. The address-event protocol designed by Mahowald [22], improvements of this protocol by Lazzaro and colleagues [23] and by Boahen [5], and versions of a interchip communication protocol [24][25] make viable a layered system, where the receptors reside on a chip that communicates to separate chips that compute motion.

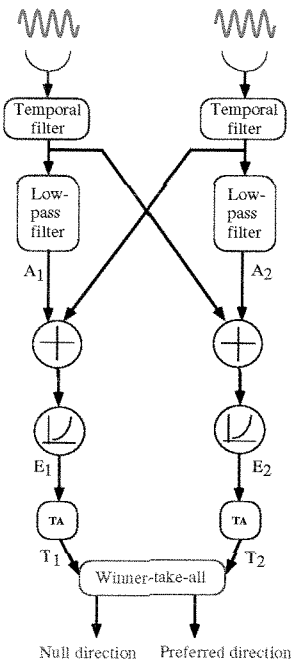

Figure 5.2: Block diagram of new motion model for direction selectivity. The nonlinearity in this circuit model is represented by an exponential. The summation and exponential blocks are equivalent to a multiplication in the circuit domain.

5.3 Correlation Model of Direction-Selective Circuit

The analog circuit model for direction selectivity is shown in Figure 5.2. The inputs go through a temporal filter that represents the filtering in the retina and laminar layer. The signals are then delayed by a lowpass filter. The nonlinearity in this model is represented by an exponential, instead of by a multiplier as in the traditional Reichardt's model. However, the summation and exponential blocks are equivalent to a multiplication in the circuit model. The correlated signals are averaged over time. The temporally averaged signals mutually inhibit each other. This inhibition is also observed in the direction-selective cells.

The adaptive correlator model in Chapter 4 can be included into this model, so that the motion system will be sensitive to changes in input frequency. The circuit implementation of the combined model has not been completed, so it will not be

discussed in this dissertation.

5.3.1 Transfer Function

Similar to the analysis in Chapter 4, we compute the transfer function of the direction-selective circuit. Let the complex transfer function of the lowpass filters be $L(\omega)e^{i\theta(\omega)}$, and let the spatial phase between the two pixels be ϕ. We assume the input to be a sine wave of form $I + \Delta I \sin(\omega t)$. The outputs of the filters, A_1 and A_2, (shown in Figure 5.2), can be written as

$$\begin{aligned} A_1 &= L(0)I + L(\omega)\Delta I \sin(\omega t - \theta(\omega)), \\ A_2 &= L(0)I + L(\omega)\Delta I \sin(\omega t + \phi - \theta(\omega)). \end{aligned}$$

We ignore the DC intensity, I, in the remainder of the analysis. The outputs, A_1 and A_2, are then summed into exponential blocks. The outputs, E_1 and E_2, of these blocks can be written as

$$\begin{aligned} E_1 &= e^{L(\omega)\Delta I\,(\sin(\omega t - \theta(\omega)) + \sin(\omega t + \phi))}, \\ E_2 &= e^{L(\omega)\Delta I\,(\sin(\omega t) + \sin(\omega t + \phi - \theta(\omega)))}. \end{aligned}$$

The outputs, T_1 and T_2, of the temporal-averaging blocks can be written as

$$\begin{aligned} T_1 &= \int_0^T E_1 dt, \\ T_2 &= \int_0^T E_2 dt, \end{aligned}$$

where T is the period of the sine wave. There is no closed-form solution for T_1 and T_2. In Figure 5.3, T_1 and T_2 are plotted versus ϕ, for a fixed time constant of the lowpass filter, $\tau = 2$s. Here, I assume the input is moving at a constant velocity and the input is composed of different spatial wavelengths. The outputs, T_1 and T_2, is computed for spatial phases between 0 and π. An increasing spatial phase between the receptors is equivalent to a decreasing wavelength of the input. The top curve corresponds to T_2;

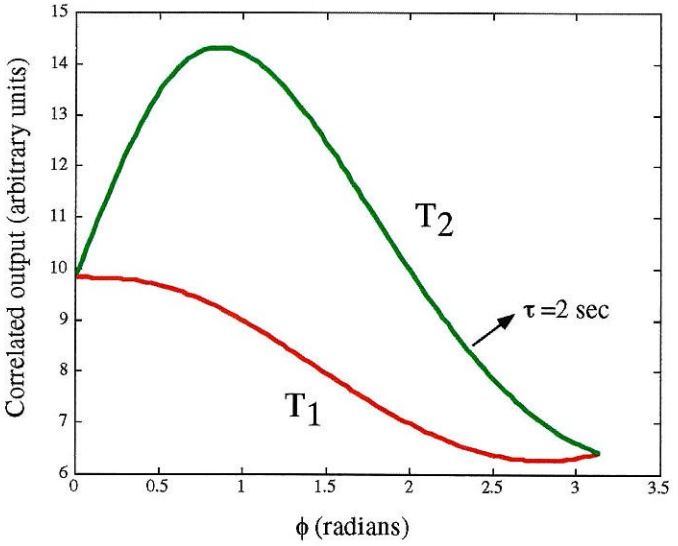

Figure 5.3: Plot of the temporal averaged outputs, T_1 and T_2, versus the spatial phase between the receptors, ϕ. An increasing spatial phase corresponds to a decreasing wavelength. We analyze the case where the velocity of the input is fixed and the input is composed of different spatial wavelengths. The top curve corresponds to T_2; the bottom curve corresponds to T_1. Here, $T_2 > T_1$ for all spatial phases between 0 and π.

the bottom curve corresponds to T_1. The figure shows that $T_2 > T_1$, thus showing that the correct direction is computed for these spatial phases. When $\phi = 0$, as in the case of flicker, the outputs, T_1 and T_2, are equal. Hence, the mutual inhibition block will signal no motion. In Figure 5.4, T_1 and T_2 are plotted versus ϕ, for two different values of $\theta(\omega)$. Here, I assume that different spatial wavelength inputs are moving at different velocities such that the temporal frequency, ω, is constant. When $\phi = 0$, as in the case of flicker, the outputs, T_1 and T_2, are equal as in the previous figure. If the spatial phase, ϕ, is positive, the correct direction is always signaled because T_1 (the solid curve)$> T_2$ (the dashed curve). The preferred direction is indicated by the horizontal arrow at the bottom of the plots. Notice that the maximum difference between T_1 and T_2 is when $\phi = \theta$. The second plot shows the outputs, T_1 and T_2, for

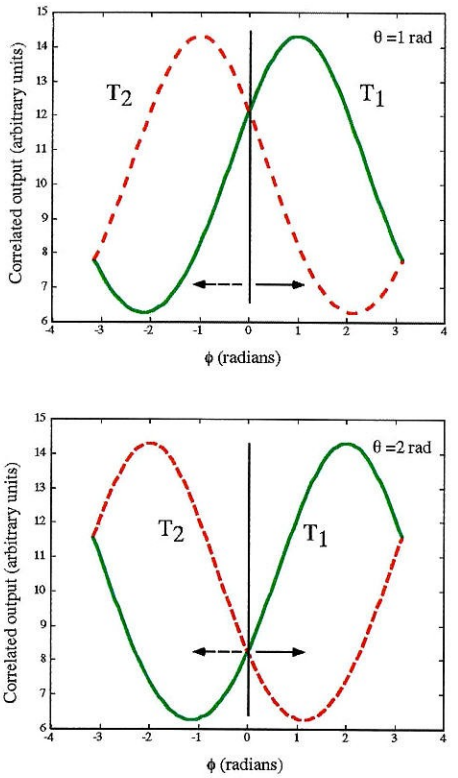

Figure 5.4: Plot of the temporal averaged outputs, T_1 and T_2, versus the phase between the receptors, ϕ, for two different values of delay through the lowpass filter, θ. The top curve corresponds to a value of $\theta = 1$ rad and the bottom curve corresponds to a value of $\theta = 2$ rad. The curves to the right of the vertical line show that if the stimulus is moving in the preferred direction, $T_1 > T_2$ for all values of ϕ. The maximum difference is obtained when the temporal phase between the receptors is equal to the delay through the lowpass filter, that is, $\phi = \theta$. In the case of flicker, that is, when $\phi = 0$, $T_1 = T_2$.

a different θ. Again, the maximum difference between the outputs is when $\phi = \theta$. By passing T_1 and T_2 to a mutual inhibition block, we get the direction of the moving stimulus.

5.3.2 Circuit Implementation

Figure 5.5 shows the circuit for the direction-selective model. The output of the retino-laminar circuit, V_l, is buffered through a source follower. The buffered output, V_b, drives a lowpass filter. Both these outputs, V_b and V_{lp}, are represented as currents,

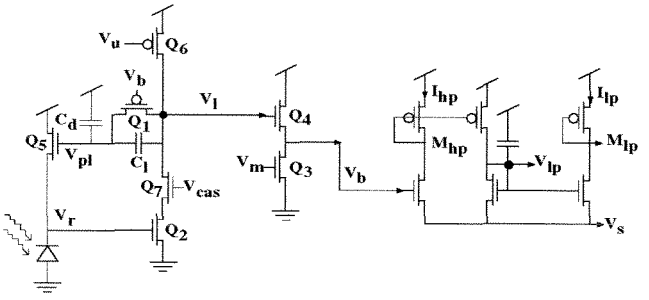

Retino-laminar circuit **Lowpass filter**

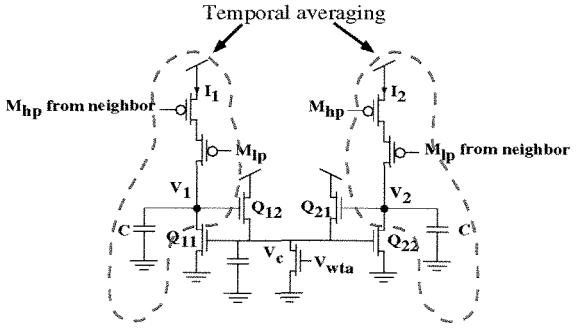

Winner-take-all circuit

Figure 5.5: Motion circuit that implements the direction-selective model shown in Figure 5.2. The output of the retino-laminar circuit, V_1, (described in Chapter 3) is buffered through a source follower consisting of Q_3 and Q_4. The source follower was also used to generate the bias to the feedback element, Q_1, in the retino-laminar circuit. The buffered output, V_b, drives a lowpass filter. The filtered output, V_{lp}, and V_b are brought out as currents, I_{lp} and I_{hp}. Note that the current, I_{hp}, is not a highpass output of V_b. The current outputs are correlated and fed to a WTA circuit. Temporal averaging is implemented as part of the WTA circuit.

I_{hp} and I_{lp}. The currents are correlated and then fed to a winner-take-all (WTA) [26] circuit. The correlated currents represent the output of the exponential stage in Figure 5.2. The temporal averaging at nodes V_1 and V_2, and mutual inhibition are both part of the WTA circuit. The transfer function of the WTA circuit is described in Appendix 7.1.

Time Constant of Lowpass Filter

The lowpass filter in Figure 5.5 does not have a fixed time constant. The current charging up the output capacitor depends on the value of $V_{\rm b}$. The transfer function is derived from the KCL equations at nodes v_x and v_l, in the small-signal model shown in Figure 5.6:

$$g_{m3}v_x + C_l\dot{v}_l + g_{m2}v_l = 0, \tag{5.1}$$

$$g_{m1}v_i + g_{m2}v_x = 0. \tag{5.2}$$

From Equation 5.2, we get $v_x = \frac{g_{m1}}{g_{m2}}v_i$. Taking the Laplace transform of Equation 5.1, we get

$$g_{m3}v_x + v_l(sC_l + g_{m2}) = 0. \tag{5.3}$$

Plugging in $v_x = \frac{g_{m1}}{g_{m2}}v_i$ into Equation 5.3, we solve for v_l:

$$v_x = -\frac{sC_l + g_{m2}}{g_{m3}}v_l = \frac{g_{m1}}{g_{m2}}v_i. \tag{5.4}$$

From Equation 5.4, we solve for v_l:

$$v_l = -\frac{g_{m1}g_{m3}}{g_{m2}(sC_l + g_{m4})} = \frac{1}{1+\tau s}v_i,$$

where $\tau = \frac{C_l}{g_{m4}}$ and all values of g_m are equal. Since g_{m4} is exponentially dependent on the gate voltage, input signals at different background intensities and different contrasts will have different time constants.

5.4 Experimental Results

The experimental results reported here are obtained from a test circuit fabricated in a $2\mu m$ CMOS ORBIT technology. Since the time constant of the lowpass filter changes exponentially with the output of the retino-laminar circuit, results are shown only at one background intensity. Most of the data shown are taken at the inputs to the

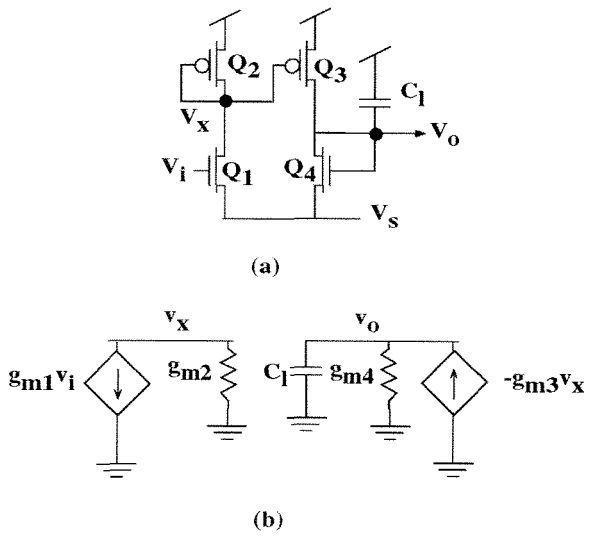

Figure 5.6: Plot of lowpass filter and small-signal model. (a) Circuit diagram of lowpass filter whose time constant depends on the input signal. (b) Small-signal model of the filter.

correlation circuitry and the WTA output. Sine-wave stimuli are used in most of the experiments. The results will show that the circuit integrates information over time before making a decision. The latency between the onset of a direction change in the stimulus and the decision made by the circuit is also obvious.

5.4.1 Output of Lowpass Filter

Depending on the value of $V_{\rm b}$, the time constant of the lowpass filter can be also be adjusted via the external bias, $V_{\rm s}$. Figure 5.7 shows the step response of $I_{\rm lp}$ to a square-wave modulated red LED of contrast 0.4 for three values of $V_{\rm s}$. The current output has been converted to a voltage through a sense-amplifier. The rise times for the three curves are 0.78ms, 1.5ms, and 3.4ms, corresponding to values of $V_{\rm s}$ of 0.215V, 0.236V, and 0.263V. The time constants are then 0.356ms, 0.68ms, and 1.54ms. Since the time constant is inversely dependent on the g_m of the transistors, $\tau = C/g_m$, we can compute κ of Q_4 from the ratios of the time constants. The transconductance,

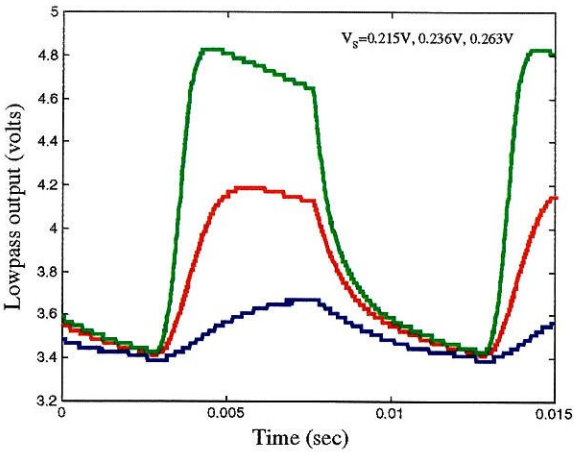

Figure 5.7: Step response of the lowpass filter for three different values of V_s.

g_m, is $\kappa I_0 e^{\kappa V_s/U_T}$. The ratio of two time constants, τ_1 and τ_2, is given by

$$\frac{\tau_1}{\tau_2} = e^{\kappa(V_{s1}-V_{s2})/U_T}.$$

From the first set of time constants, 0.356ms and 0.68ms, we find that $\kappa = 0.8$; from the second set, 0.68ms and 1.54ms, we get $\kappa = 0.78$. We can also see that the fall time of the step response is smaller than the rise time because the value of V_b is higher at the high-to-low going edge.

Figure 5.8 shows the step responses of V_b and I_{hp} to a stimulus of contrast 0.4 at two background intensities. The lighter-colored curves are the responses at the lower background intensity. The current output is smaller and the time constant is larger in the case of the low background intensity. The plot illustrates the large difference in time constants of the outputs with only 70mV difference between the two values of V_b. We can also see that the fall time of I_{hp} is smaller than the rise time. The time constant also changes for different contrast signals at the same background intensity as shown in Figure 5.9. The two different input contrasts are 0.4 and 0.54. The difference in the time constant is again due to the different values of V_b.

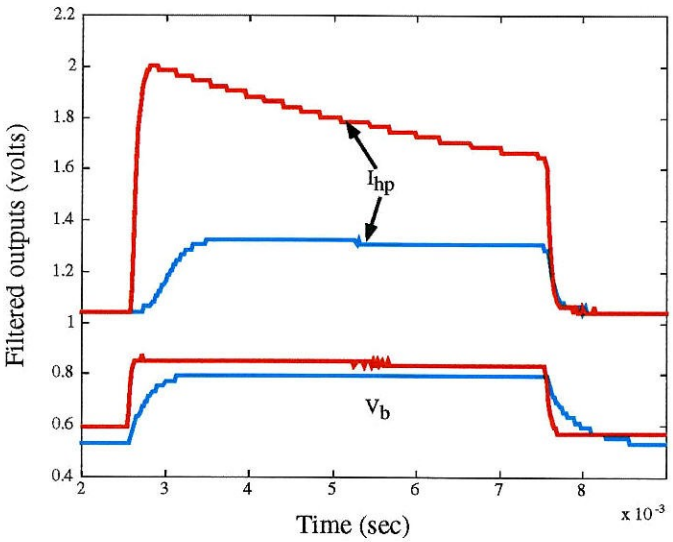

Figure 5.8: Step responses of V_b and I_{hp} to a stimulus of contrast 0.4 at two background intensities. The darker-colored curves are the responses to the stimulus at the higher background intensity. The current output is higher than that at the lower background intensity because of the higher value of V_b.

5.4.2 Response of Direction-Selective Output

I recorded the response of the direction-selective output to motion by displaying a moving sine-wave stimulus (actually a rotating wheel with spokes of alternating gray levels) to the chip. The range of temporal frequencies of the stimulus varies from 1Hz to about 22Hz. In Figure 5.10, I show the responses of V_b and the direction-selective output to a slow moving stimulus at a frequency of 2.3Hz. The stimulus changes direction and its input frequency increases to 2.7Hz in the middle of the plot. This figure shows that the circuit responds to direction changes independent of the speed of the stimulus. Notice the latency between the onset of the direction change in the stimulus and the change in the direction-selective output. This latency indicates that the circuit is averaging the input information over time.

The same data were obtained for a stimulus that initially moved at 9Hz and switched to 10Hz in the middle of Figure 5.11. Thus, the circuit still responds correctly to a faster moving stimulus. The circuit can respond to the moving stimulus up to frequencies of more than 22Hz. Unfortunately, it was difficult to drive the motor

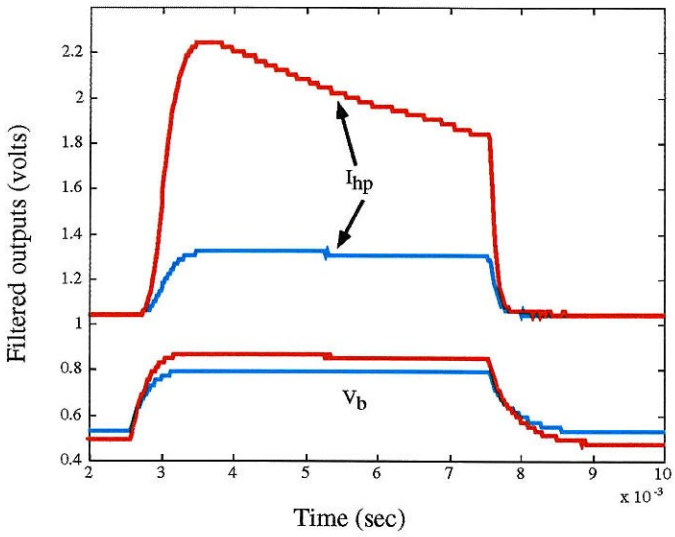

Figure 5.9: Step responses of V_b and I_{hp} to a stimulus of contrast 0.4 and 0.54 at the same background intensity. The time constants of the current output are different in both cases because of the different values of V_b.

holding the stimulus at frequencies greater than 22Hz. The contrast of the stimulus in Figure 5.10 and Figure 5.11 is 0.82. Figure 5.12 shows the data of the same experiment for a stimulus of lower contrast at 0.58.

The direction-selective output is also invariant with the stimulus speed as shown in Figure 5.13 and Figure 5.14. The stimulus was slowed down in Figure 5.13 and speeded up in Figure 5.14. Figure 5.15 shows the responses of V_b and the direction-selective output to my hand moving back and forth over the chip. The sharp peaks in the V_b output corresponds to the edges of my hand. The circuit computes the direction of motion correctly.

5.4.3 Dependence of Direction-Selective Output on Contrast

The data from the experiments described in Section 5.4.1 and Section 5.4.2 are obtained with a fixed set of biases. In this case, the chip stops responding when the contrast of the stimulus on the wheel goes below 0.58. This behavior does not mean that the circuit cannot respond to a lower contrast. By setting V_s to a lower value, the circuit responds down to a contrast of 0.3, but then the high-contrast signals

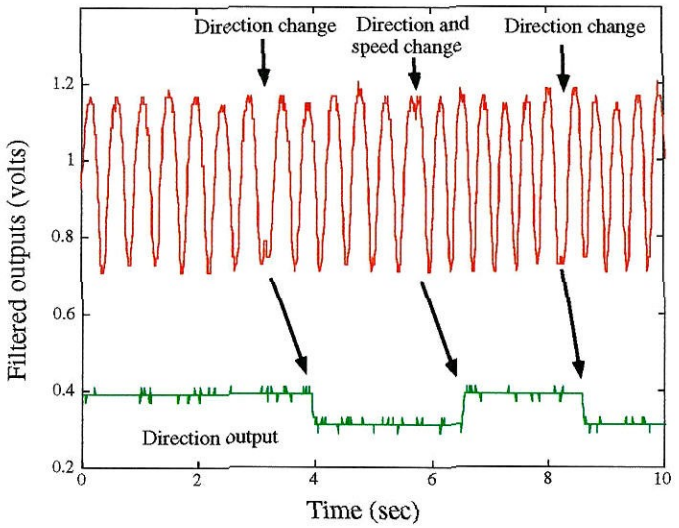

Figure 5.10: Responses of V_b and the direction-selective output to direction changes of the stimulus. The speed of the stimulus increases from 2.3Hz to 2.7Hz in the middle of the figure.

are a problem because the time constant is too fast for a reliable correlated output. To illustrate that the chip works with low-contrast signals, the moving stimulus was shown under fluorescent lighting. The responses are shown in Figure 5.16. The p–p output of V_b is only about 60mV, as compared to the p-p values of V_b in Section 5.4.2 which range from 0.2 to 0.3V. The p–p output of 60mV corresponds to a stimulus of contrast of 0.118.

The latency of the direction-selective output for low-contrast signals is longer than that of high-contrast signals, because the time constant of the filter is shorter for high contrast signals as shown in Figure 5.9. Figure 5.17 shows the latency of the direction-selective responses to two different contrast stimulus. The top set of curves show the responses to the stimulus of contrast 0.82, while the bottom set of curves show the responses to the stimulus of contrast 0.58. The latency of the direction-selective output is shorter for the higher-contrast stimulus.

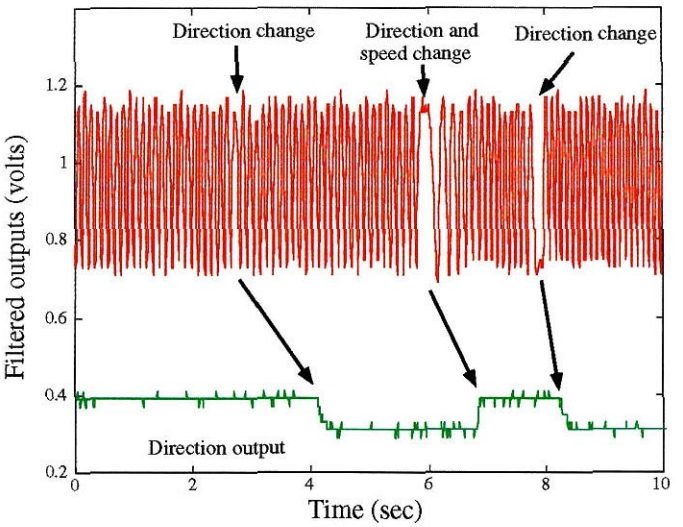

Figure 5.11: Responses of V_b and the direction-selective output to direction changes of the stimulus. The speed of the stimulus increases from 9Hz to 10Hz in the middle of the figure.

5.5 Discussion

The motion circuit described in this chapter shows that direction selectivity can be computed from continuous-time graded signals of low contrast. The robustness of the output signal is increased through the use of temporal averaging and mutual inhibition. Inhibition has been observed in the direction-selective cells in the lobula plate. The time constant of this circuit is exponentially dependent on the background intensity. This property makes it difficult to operate the circuit over decades of background intensity and will be removed in a subsequent implementation.

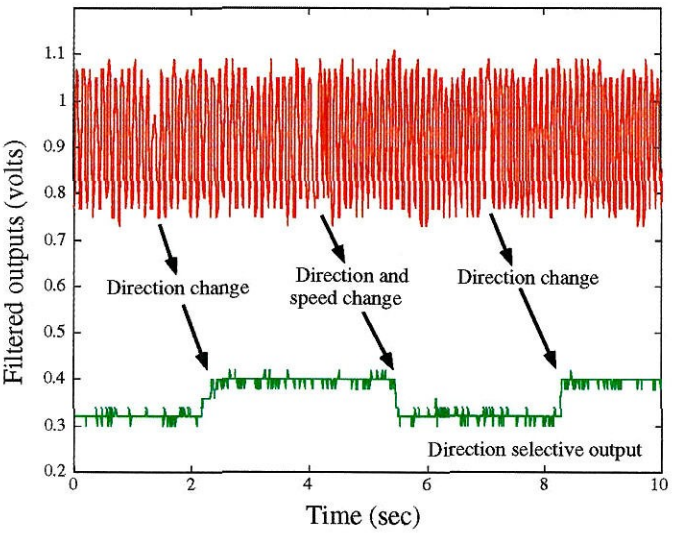

Figure 5.12: Responses of V_b and the direction-selective output to direction changes of the stimulus at a contrast of 0.58. The speed of the stimulus increases from 9Hz to 10Hz in the middle of the figure.

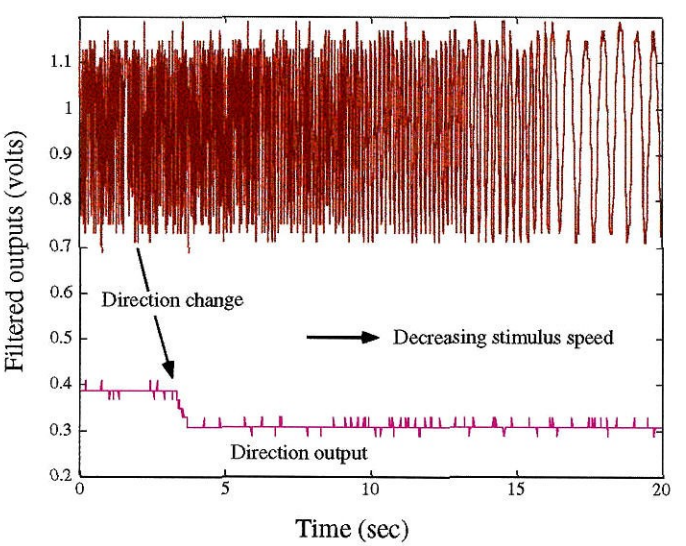

Figure 5.13: Responses of V_b and the direction-selective output to the slowing down of the stimulus. The data show that the direction-selective output depends on only the direction change of the stimulus, and not on the decreasing speed of the stimulus.

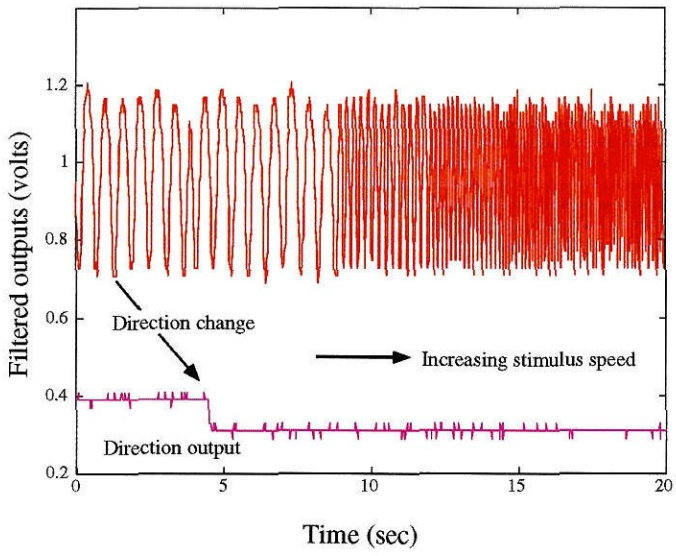

Figure 5.14: Responses of V_b and the direction-selective output to the speeding up of the stimulus. The figure shows that the direction-selective output depends on only the direction change of the stimulus, and not on the increasing speed of the stimulus.

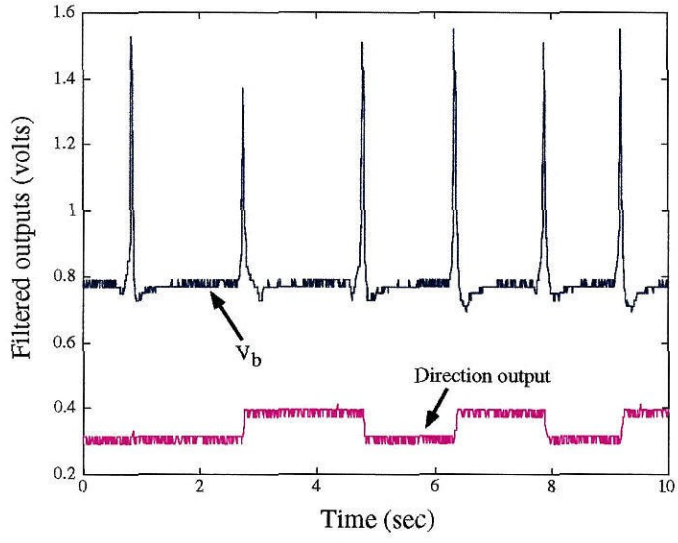

Figure 5.15: Responses of V_b and the direction-selective output to my hand moving back and forth over the chip.

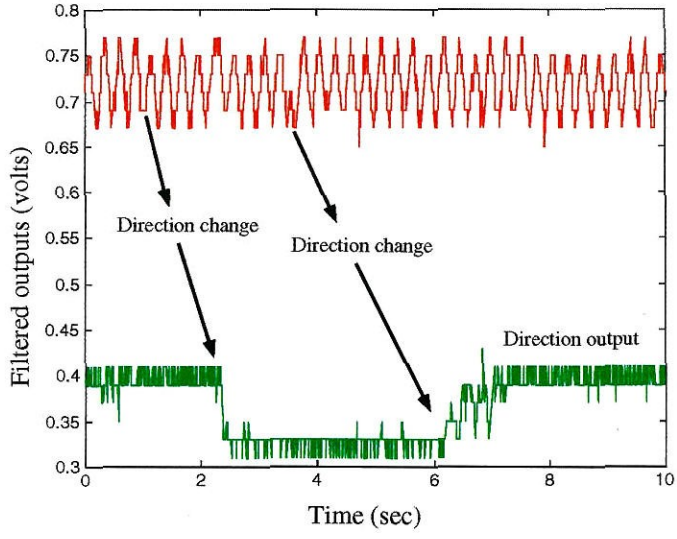

Figure 5.16: Responses of V_b and the direction-selective output to a change in direction of the stimulus under fluorescent lighting.

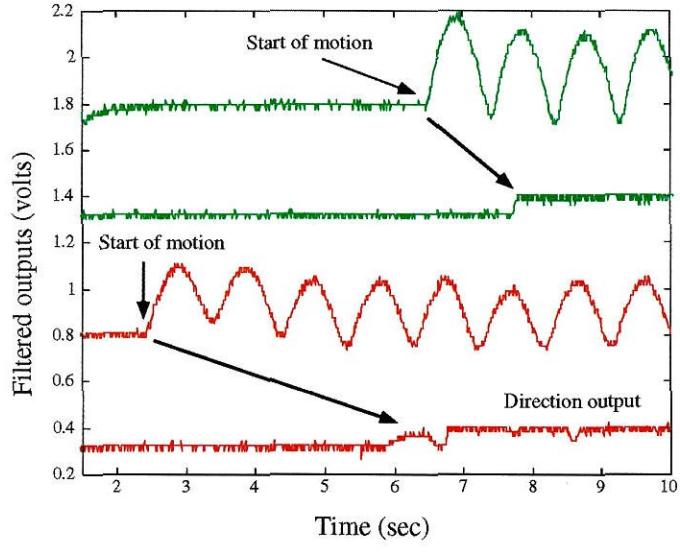

Figure 5.17: Responses of V_b and the direction-selective output for two different contrast signals to a sine-wave stimulus moving at 1Hz. The top set of curves are the responses to a stimulus of 0.82; the bottom set of curves are the responses to a stimulus of 0.58. The latency for the response of the circuit is shorter for the higher-contrast stimulus.

Bibliography

[1] W. Reichardt, "Autocorrelation: A principle for the evaluation sensory information by the central nervous system," in *Sensory Communication*, W. A. Rosenblith, ed, Wiley, New York, pp. 303–317, 1961.

[2] J. P. H. van Santen and G. Sperling, "Temporal covariance model of human motion perception," *J. Opt. Soc. America A*, **1:4**, pp. 451–473, 1984.

[3] J. P. H. van Santen and G. Sperling, "Elaborated Reichardt detectors," *J. Opt. Soc. America A*, **2:2**, pp. 300–320, 1985.

[4] W. A. Beaudot, "Sensory coding in the vertebrate retina – towards an adaptive control of visual sensitivity," *Network Computation in Neural Systems*, **7**, pp. 317–323, 1996.

[5] K. Boahen, "Retinomorphic vision systems: reverse engineering the vertebrate retina," *PhD Thesis*, California Institute of Technology, Pasadena, CA, 1997.

[6] E. Adelson and J. Bergen, "Spatiotemporal energy models for the perception of motion," *J. Opt. Soc. America A*, **2:2**, pp. 284–299, 1985.

[7] A. B. Watson and A. J. Ahumada, Jr, "Model of human visual-motion sensing," *J. Opt. Soc. America A*, **2:2**, pp. 322–341, 1985.

[8] J. Tanner and C. Mead, "An integrated optical motion sensor," in *VLSI Signal Processing II*, S. Y. Kung, R. Owen, and J. Nash, eds, IEEE Press, New York, pp. 59–76, 1986.

[9] A. Andreou and K. Strohbehn, "Analog VLSI implementation of Hassenstein–Reichardt–Poggio models for vision computation," *Proc. IEEE Symp. Syst., Man Cybern*, pp. 707–710, 1990.

[10] K. Strohbehn, R. C. Meitzler, A. G. Andreou, and R. E. Jenkins, "Analog image processing with silicon retinas," *Johns Hopkins APL Technical Digest*, **15:3**, pp. 178–187, 1994.

[11] R. Sarpeshkar, W. Bair, and C. Koch, "An analog VLSI chip for local velocity estimation based on Reichardt's motion algorithm," in *Advances in Neural Information Processing Systems 5*, S. Hanson, J. Cowan, and L. Giles, eds, Morgan Kaufmann, San Mateo, CA, pp. 781–788, 1993.

[12] J. Kramer, R. Sarpeshkar, and C. Koch, "An analog VLSI velocity sensor," *Proc. Int. Symp. Circuits Syst. ISCAS 95*, pp. 413–416, Seattle, WA, 1995.

[13] R. Sarpeshkar, J. Kramer, G. Indiveri, and C. Koch, "Analog VLSI architectures for motion processing - from fundamental limits to system applications," *Proceedings of the IEEE*, **84:7**, pp. 969–987, 1996.

[14] J. Kramer, R. Sarpeshkar, and C. Koch, "Pulse-based analog VLSI velocity sensors," *IEEE Transactions on Circuits and Systems II* , **44:2**, pp. 86–101, 1997.

[15] R. Etienne-Cummings, C. Donham, J. van der Spiegel, and P. Mueller, "Spatiotemporal computation with a general purpose analog neural computer: Real-time visual motion estimation," *Proc. IEEE Int. Conf. on Neural Networks*, pp. 1835–1840, 1994.

[16] R. Etienne-Cummings, J. van der Spiegel, and P. Mueller, "A focal-plane visual-motion measurement sensor," *IEEE Transactions on Circuits and Systems I*, **44:1**, pp. 55–66, 1997.

[17] T. Horiuchi, W. Bair, B. Bishofberger, A. Moore, C. Koch, and J. Lazzaro, "Computing motion using analog VLSI chips: An experimental comparison among different approaches," *Int. Journal on Comp. Vision*, **8**, pp. 203–216, 1992.

[18] T. Delbrück, "Silicon retina with correlation-based velocity-tuned pixels," *IEEE Transactions on Neural Networks*, **4**, pp. 529–541, 1993.

[19] H. B. Barlow and W. R. Levick, "The mechanisms of directionally selective units in rabbit's retina," *Journal of Physiology*, **178**, pp. 477–504, 1965.

[20] R. Benson and T. Delbrück, "Direction selective silicon retina that uses null inhibition," in *Advances in Neural Information Processing Systems 4*, J. Moody, S. Hanson, and R. Lippmann, eds, Morgan Kaufmann, San Mateo, CA, pp. 756–763, 1992.

[21] A. Simoni, G. Torelli, F. Maloberti, A. Sartori, S. Plevridis, and A. Birbas, "A single chip optical sensor with analog memory for motion detection," *IEEE J. Solid-State Circuits*, **30:7**, pp. 890–897, 1995.

[22] M. Mahowald, "VLSI analogs of neuronal visual processing: a synthesis of form and function," *PhD Thesis*, California Institute of Technology, Pasadena, CA, 1994.

[23] J. Lazzaro, J. Wawrzynek, M. Mahowald, M. Sivilotti, and D. Gillespie, "Silicon auditory processors as computer peripherals," *IEEE Transactions on Neural Networks*, **4:3**, pp. 523–528, 1993.

[24] A. Mortara, E. A. Vittoz, and P. Venier, "A communication scheme for analog VLSI perceptive systems," *IEEE J. Solid-State Circuits*, **30:6**, pp. 660–669, 1995.

[25] P. Venier, A. Mortara, X. Arreguit, and E. Vittoz, "An integrated cortical layer for orientation enhancement," *IEEE Journal of Solid State Circuits*, **32:2**, pp. 177–286, 1997.

[26] J. Lazzaro, S. Ryckebusch, M. Mahowald, and C. Mead, "Winner-take-all networks of O(n) complexity," in *Advances in Neural Information Processing Systems 1*, D. Tourestzky, ed, Morgan Kaufmann, San Mateo, CA, pp. 703–711, 1988.

Chapter 6 Conclusions

This dissertation has described the development of a direction-selective system that included the preprocessing properties of the retina and laminar cells, and also the motion adaptation observed in the direction-selective cells of the lobula plate. This system is an improvement over previous motion systems by adding adaptive temporal preprocessing after the receptor circuit and incorporating temporal averaging for robustness and mutual inhibition. The various chapters describe the different subsystems of the direction-selective system.

In Chapter 2, I compared the temporal and spatial bandwidths of a previous silicon receptor model [1] with that of different insect receptors. The results of the comparison show that even though silicon receptors have higher limits on the speed sensitivities at high background intensities, these receptors perform poorly at low background intensities. In contrast, the speed sensitivities of insect receptors are almost invariant to the background intensity. A main reason for this difference is that the temporal bandwidths of our silicon receptors vary linearly with the background intensity, while the bandwidths of the biological receptors depend on a 1/3 to 1/4 root of the intensity. In the interest of keeping the pixel area small, our silicon receptors do not model the sharp cutoff in the frequency gain curves of the biological receptors. This sharp cutoff might be important in the subsequent motion detection process.

This dissertation contains the first characterization of offset distributions in our silicon retinae and that in the fly receptors. Both the neural system and the silicon system have to deal with mismatches between neurons or transistors. If the offset distribution is worse in our silicon retinae, then we should use adaptation or self-calibration methods to reduce the range of offsets. It is difficult to obtain data that describe the offset statistics in a single organism. The data from the fly receptors were obtained from different flies but of the same species. It is interesting to see that the offset distribution is small among different flies. We can do a better comparison of the

offsets in both systems, by characterizing the offsets of different chips with the same design and layout that have been fabricated on the same run. I have characterized the offsets at only one background intensity. It would be interesting to see if the offset statistics vary with the background intensity.

The Delbrück receptor model has been endowed with the adaptive temporal filtering properties of the LMCs by adding two more transistors to the circuit. This new retino-laminar circuit, shown in Chapter 3, has an adaptation time constant that can be controlled by an external bias. The temporal filtering also changes with the background intensity. The change in the temporal filtering with the S/N conditions can be predicted by using information theory [2]. The assumption used is that the visual system tries to maximise the information transfer to subsequent layers. The retino-laminar circuit does not implement the weak spatial center-surround property and the zero DC gain of the LMCs.

The adaptive correlator described in Chapter 4, models the time constant adaptation of the motion system to the temporal frequencies of the input stimuli. This model is a variant of the Hassenstein–Reichardt (HR) model. The filters in the HR model are endowed with adaptive time constants and the circuitry for adapting the time constants are included in the adaptive correlator. The results from this model explain the physiological results from the direction-selective cells. The results from a silicon implementation of this model also show that the time constants of the filters indeed adapt to the motion stimuli.

The final system described in Chapter 5, is a novel implementation of the HR model, where temporal averaging and mutual inhibition are part of the direction selectivity process. The circuit uses the graded output signals of the retino-laminar circuit, and does not use any pulses or edges in the direction selective computation. Previous implementations have ignored the temporal averaging computation in the correlation model, and only one other implementation incorporated mutual inhibition. The mutual inhibition process models the inhibition observed in the H1 cell in the lobula plate when motion in the null direction is presented to the eye. The temporal averaging process induces different latencies for different contrast signals. For low

contrast signals, the circuit exhibits a longer latency in reaching a decision on the direction of motion. The circuit needs to be extended to the 2D domain and the correlated inputs that are fed to the mutual inhibition block need to be brought out. The adaptation circuitry described in Chapter 4 needs to be incorporated into this direction-selective model. The time constant of the lowpass filter in the present model is exponentially dependent on the background intensity. This property makes it difficult to operate the circuit over decades of background intensity and will be removed in a subsequent implementation.

The different subsystems of the direction-selective system show the importance of understanding the filters at each processing stage of the visual layers. Obviously, the spatial and temporal processing in each stage is necessary for obtaining robust outputs at the final motion layer under different background conditions. It is also important that we understand the relevance of the spatiotemporal processing in each layer. The neuromorphic modeling of the fly visual system gives us a medium to develop a working model that captures the spatiotemporal features necessary for robust motion computation. It also allows us to address the issues that neural systems face, for example, offsets and noise.

Bibliography

[1] T. Delbrück, "Analog VLSI phototransduction by continous-time, adaptive, logarithmic photoreceptor circuits," CNS Memo No.30, California Institute of Technology, Pasadena, CA, 1994.

[2] J. H. van Hateren, "Theoretical predictions of spatiotemporal receptive fields of fly LMCS, and experimental validation," *J. Comp. Physiology A*, **171:2**, pp. 157–170, 1992.

Chapter 7 Appendix to Chapter 5

7.1 Transfer Function of WTA

The transfer function of the The equations at nodes V_1 and V_2 are:

$$i_1 = C\dot{v}_1 + g_{d11}v_1 + g_{m11}v_c, \tag{7.1}$$

$$i_2 = C\dot{v}_2 + g_{d22}v_2 + g_{m22}v_c. \tag{7.2}$$

The equation at node V_c is:

$$g_{m12}(v_1 - v_c) + g_{m21}(v_2 - v_c) = C_c\dot{v}_c + (g_{d12} + g_{d21})v_c. \tag{7.3}$$

Rewriting Equation 7.3 in the Laplace domain, we get

$$g_{m12}v_1 + g_{m21}v_2 \approx (sC_c + g_{m12} + g_{m21})v_c.$$

Hence,

$$v_c = \frac{g_{m12} + g_{m21}}{sC_c + g_{m12} + g_{m21}}. \tag{7.4}$$

Taking the Laplace transform of Equations 7.1 and 7.2 and substituting v_c from Equation 7.4, we get

$$\begin{aligned} i_1 &= (sC + g_{d11})v_1 + (g_{m11}g_{m12}/Y)v_1 + (g_{m11}g_{m21}/Y)v_2 \\ &= (sC + g_{d11} + g_{m11}g_{m12}/Y)v_1 + (g_{m11}g_{m21}/Y)v_2, \end{aligned} \tag{7.5}$$

$$\begin{aligned} i_2 &= (sC + g_{d22})v_2 + (g_{m22}g_{m12}/Y)v_1 + (g_{m22}g_{m21}/Y)v_2 \\ &= (sC + g_{d22} + g_{m22}g_{m21}/Y)v_2 + (g_{m22}g_{m12}/Y)v_1, \end{aligned} \tag{7.6}$$

where $Y = sC_c + g_{m12} + g_{m21}$. Substituting in v_2 from Equation 7.5 into Equation 7.6, we get:

$$\begin{aligned} i_1 &= (sC + g_{d11} + \frac{g_{m11}g_{m12}}{Y})v_1 + \frac{g_{m11}g_{m21}}{Y}(i_2 - \frac{g_{m22}g_{m12}}{Y}v_1)\frac{Y}{(sC + g_{d22})Y + g_{m22}g_{m21}} \\ &= \frac{((sC + g_{d11})(sC + g_{d22})Y + (sC + g_{d11})g_{m22}g_{m21} + (sC + g_{d22})g_{m11}g_{m12})v_1 + g_{m11}g_{m21}i_2}{(sC + g_{d22})Y + g_{m22}g_{m21}} \end{aligned}$$

$$\begin{aligned} i_2 &= (sC + g_{d22} + \frac{g_{m22}g_{m21}}{Y})v_2 + \frac{g_{m22}g_{m12}}{Y}(i_1 - \frac{g_{m11}g_{m21}}{Y}v_2)\frac{Y}{(sC + g_{d11})Y + g_{m11}g_{m12}} \\ &= \frac{((sC + g_{d22})(sC + g_{d11})Y + (sC + g_{d22})g_{m11}g_{m12} + (sC + g_{d11})g_{m22}g_{m21})v_2 + g_{m22}g_{m12}i_1}{(sC + g_{d11})Y + g_{m11}g_{m12}} \end{aligned}$$